Robotically Assembled Space Telescopes with Deployable Modules: Concepts and Design Methodologies

Thesis by
Kristina Hogstrom

In Partial Fulfillment of the Requirements for the
degree of
Doctorate of Philosophy in Space Engineering

CALIFORNIA INSTITUTE OF TECHNOLOGY
Pasadena, California

2017
Defended June 27, 2016

ACKNOWLEDGEMENTS

Firstly, I would like to thank my advisor, Professor Sergio Pellegrino. On my second day at Caltech, I was presented with the opportunity to work on cool space stuff in the Astronomy department for my PhD. So after the Masters program, I jumped the Guggenheim ship and ventured over to Cahill, while Professor Pellegrino kept an eye on me as my academic advisor and liaison in GALCIT. A year later, things were not working out as planned; my PhD advisor was leaving Caltech and I wasn't sure what my future would hold. Feeling lost and panicked about changing directions and being a year behind, I turned to Professor Pellegrino for advice. He gave me a chance and welcomed me back to GALCIT as his student. Best of all, I still got to work on cool space stuff!

I would also like to thank all of my mentors and collaborators at JPL and NASA Langley, especially those who worked with me during my NSTRF internships. As my NSTRF mentor, Stuart Shaklan introduced me to the field of coronagraphs for exoplanet research during my internship, and has offered his invaluable support and feedback throughout my NSTRF tenure. Erik Komendera, John Dorsey, and Bill Doggett shared their unique expertise with me on space structures and assembled telescopes, and provided me with generous resources for building my experiment at NASA Langley.

Of course, I would like to thank my committee members, Professors Ravi Ravichandran, Dennis Kochmann, and Joel Burdick, for all of their advice and guidance throughout this experience.

I must also thank my summer intern, Isabelle Phinney, for her help with programming, wiring, soldering, and all of the tedious work that interns are asked to do. I was incredibly lucky to have an intern as bright, knowledgeable, and hard-working as her.

I would like to thank the NASA Space Technology Research Program for their generous support, funding this work under grant number NNX13AL67H. I would especially like to thank the Keck Institute for Space Studies, specifically Michele Judd and Tom Prince, for not only funding my first year at Caltech, but for organizing such incredible and exciting events and opportunities for Keck fellows over the years.

I have to thank the entire GALCIT community and administrative staff for working so hard behind the scenes to make sure the department runs smoothly.

Special thanks to Kate for dealing with my insane fellowship finances and billing, to Christine for all her help keeping my coursework and PhD forms on track, to Dimity for being the glue that keeps the entire department together, and to Petros for all of his help setting up experiments and transporting them to JPL.

Of course, this thesis would not have been possible without my mom and dad, for obvious reasons (bringing me into existence), but also for raising me to be the person I am today, which I will admit was not an easy task. In my earliest childhood, they taught me to be curious and confident, to absorb the world and never stop learning. As a kid, they showed me that they'd love me no matter what and that they'd never be disappointed in me, but that I should strive to never be disappointed in myself. As a rebellious teen, they gave me the freedom to make mistakes and find my own path, trusting that ultimately I would put my future and academic success above all else. As an adult, they continue to support me and tell me how proud they are, but most importantly, they remind me to be proud of myself.

I would also like to thank my LA family, the entire Burgoyne-Stein-Harris-Brandt-Weiss clan. They are the most warm and welcoming group of people I have been lucky enough to meet, and they have helped make this city my home.

Finally, there's no one who deserves my thanks more than Hayden. Starting with first-year problem sets, then the months we spent studying for quals together, then our temporary relocation to Virginia together, and basically going through this whole experience together every step of the way, no one has had to put up with my craziness more than him. For the last five years, he has kept me afloat when I felt like I was sinking and celebrated with me when everything inevitably turned out okay (as he said it would). So obviously, I need to thank him for being by my side. However, most importantly, I need to thank him for just being himself. Anyone will tell you that he is unconditionally kind to everyone, unquestionably dedicated in his career, and unceasingly loyal to those he loves most. Yet, one of his most unique and notable qualities is his quiet confidence, how he stays even-keeled in the face of difficult challenges. He has had so many successes in his life that he worked hard to achieve. Being the logical person that he is, he has learned to trust in himself, to trust that he will continue to succeed, and that no challenge is too difficult for him if he puts in the same hard work. It is with this same logic that he trusts in me. Every day he encourages me to believe in myself and inspires me to better myself. I am so grateful that we are on this journey together and I'm confident that we'll accomplish great things.

ABSTRACT

This thesis first presents a novel architecture for robotically assembled optical telescopes with apertures between 20 m and 100 m, that utilizes only currently available technology. In this architecture, the primary mirror consists of two layers: a reflective layer and a truss backplane layer. The reflective layer is divided into mirror modules, or groups of mirror segments and actuators. The truss backplane layer is divided into truss modules that fold compactly for launch and are deployed in space by the robot. In this thesis, the design methodology of the mirror modules and truss modules is detailed. The ability of the designed truss layer to maintain precision requirements in the presence of typical space environment loads is demonstrated.

This architecture requires the deployment of many truss modules, and thus the deployment must be reliable despite errors introduced during manufacturing. In this thesis, a new simulation-based toolkit for estimating deployment reliability is described, including the experimental validation of the deployment simulation and the Monte Carlo-style method for repeating deployment simulations with different distributions of random fabrication errors to statistically estimate reliability. Using the toolkit, a set of reliability trade studies are then presented, revealing how different types of errors and design parameters affect reliability. Finally, the manufacturing tolerances and design modifications required to ensure high reliability are proposed.

Even if all modules deploy successfully, fabrication errors will still be present and may affect the assembly process. In this thesis, a new simulation method is presented that can model the step-by-step assembly of flexible modules with errors. The method is used to reveal that overall shape errors grow with the number of connections, resulting in significantly decreased surface precision and large-scale deformations from the nominal backplane shape as the size of the backplane increases. The misalignment at each individual connection does not increase as the backplane increases, but can still be much larger than the applied manufacturing tolerances simply due to random combinations. A simple design for the interconnects between modules is then tested, with simulation results demonstrating that it is unlikely to fully engage when the expected errors are present. With this information, a requirement on the complexity of the interconnect design is inferred, and potential modifications that may increase its efficacy are suggested.

PUBLISHED CONTENT AND CONTRIBUTIONS

[1] Nicolas Lee et al. "Architecture for In-space Robotic Assembly of a Modular Space Telescope". In: *Journal of Astronomical Telescopes, Instruments, and Systems* (2016). DOI: 10.1117/1.JATIS.2.4.041207.

[2] Kristina Hogstrom et al. "Methods for Characterizing and Increasing the Reliability of Deployable Modules for Large Optical Reflectors". In: *3rd AIAA Spacecraft Structures Conference, AIAA Science and Technology Forum and Exposition*. San Diego, California, USA, 2016. DOI: 10.2514/6.2016-2164.

[3] Kristina Hogstrom et al. "A Robotically Assembled 100-meter Space Telescope". In: *65th International Astronautical Congress*. Toronto, CA, 2014. URL: https://iafastro.directory/iac/archive/browse/IAC-14/C2/2/26019/.

TABLE OF CONTENTS

LIST OF ILLUSTRATIONS

LIST OF TABLES

Chapter 1

INTRODUCTION

1.1 Motivation, Background, and Research Goals

The future of astronomy may rely on extremely large optical telescopes to study the first stars or image Earth-sized exoplanets. Such small and faint targets, previously invisible, may then be revealed with the light collecting area and resolution enabled by larger aperture sizes. Already, ground-based telescopes are reaching new extremes. Currently in operation are the Hobby-Everly Telescope (HET), Southern African Large Telescope (SALT), and the Keck Telescope, all 10-m class [1][2][3]. The 25-m Giant Magellan Telescope is now under construction, while the Thirty Meter Telescope and the 40-m European Extremely Large Telescope are planned for first light in the early 2020s [4][5][6]. All of these telescopes have in common a segmented aperture design, which divides the primary mirror into many precisely shaped mirror segments. This sharply reduces the cost of mirror fabrication and enables aperture sizes not possible with a single monolithic mirror.

Ground-based telescopes do have limitations. Atmospheric turbulence unavoidably degrades the image at even the clearest locations, unless corrected by an active optics system. Strong structures are required to support the mirror segments and prevent gravity sag from distorting the image. These structures also limit the separation distance between the primary and secondary mirrors, necessitating shorter focal lengths which often translate to tighter positioning tolerances of the downstream optics. In space, these problems are mitigated or non-existent. Of course, space-based telescopes also have limitations, with the largest currently in operation being the 2.4-m Hubble Space Telescope [7]. Even without considering the cost of the launch vehicle, with conventional architectures, a fundamental limit on the aperture is set by the size of the payload fairing. The upcoming James Webb Space Telescope is designed to bypass this limit by folding up for launch and deploying autonomously in space, allowing an aperture 6.5 m across to fit inside a payload fairing with a diameter of only 4.5 m [8]. The upcoming SLS launch vehicle, with an 8-m fairing diameter, is enabling new concepts for deployable telescopes up to 16 meters [9][10]. However, even with these architectures, the fairing constraint is still present, and certainly an aperture size exists at which the required packaging

efficiency, or compactness after folding, is either impractical or impossible. At present, this size limit is believed to be around 20 m. Ground-based telescopes are obviously not constrained to the size of one truck, because they can be brought to the location in pieces on many trucks and constructed by a crew on-site. The same can be true for space telescopes using the concept of on-orbit assembly. By launching the telescope in pieces and assembling it in space, the fairing constraint is removed entirely, and the aperture size can theoretically be as large as the budget allows.

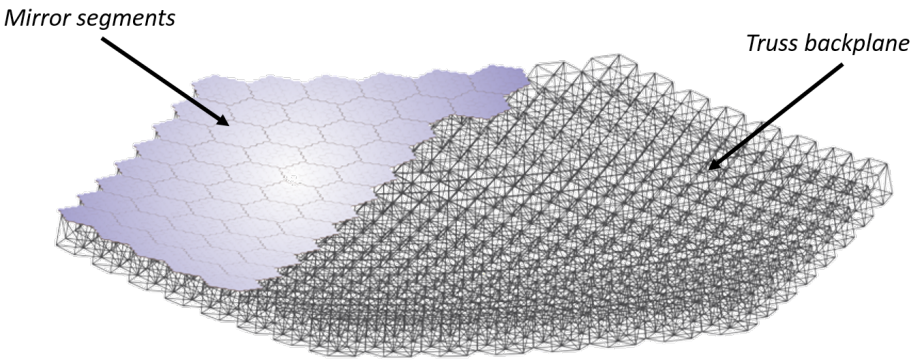

Figure 1.1: Illustration of a typical large optical reflector with mirror segments forming the reflective surface and an underlying truss backplane structure to support those segments.

A significant body of preliminary concept studies for large space-based telescopes assembled on-orbit has been produced over the last four decades, especially in the early 1980s with the beginning of the Space Shuttle program [11][12]. In all of these concepts, attention was almost entirely directed to the primary mirror (PM), the largest component and thus presumably the most difficult to assemble. The primary mirror typically consists of two layers: the reflector surface, composed of mirror segments that may be backed by actuators, and the truss support structure, or backplane, as illustrated in Figure 1.1. In the late 1980s through early 1990s, NASA Langley developed a method for assembling the backplane by connecting each strut or member individually, working outward from a central hub on a rotating platform [13][14][15][16]. Each mirror segment would be then attached after a sufficient portion of the backplane was completed. The assembly process was adapted for both human and robotic construction. This concept was matured to the point of neutral buoyancy testing with a 14-m aperture, proving the feasibility of the assembly method. However, for larger aperture sizes, strut-by-strut assembly may be needlessly time consuming. Other concepts instead used a modular approach, dividing not just the reflector surface but also the backplane into a series

of repeating cells that could be easily packaged for launch and assembled on-orbit [17][18][19][20][21][22][23][24]. A selection of these concepts is shown in Figure 1.2. To increase packaging efficiency, the backplane units were typically deployable and could be folded compactly. On orbit, a central robot or crew would deploy and connect each unit.

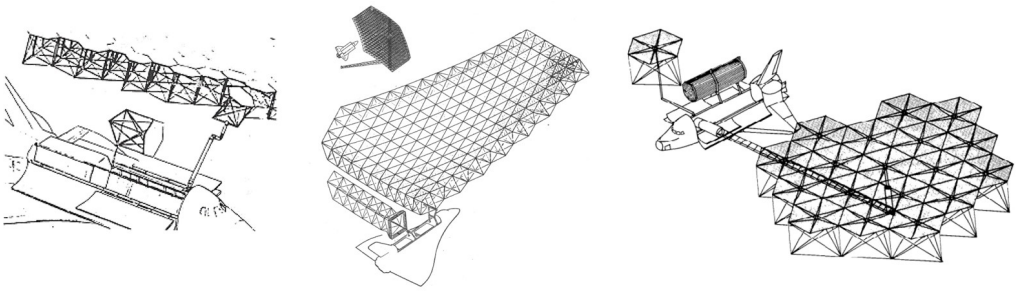

(a) (b) (c)

Figure 1.2: Illustrations of large modular antenna concepts constructed on-orbit. Each of these concepts used the Space Shuttle robotic arm as the construction robot. Sources: (a) from [23], (b) from [20], and (c) from [17].

Until recently, these proposed telescopes were confined to radio and infrared wavelengths, as the precision required for optical observations was not thought to be achievable with such large assembled structures. However, significant technological advancements have been made in active and adaptive optics, which can greatly relax the tolerances on the telescope structure itself [25][26][27][28][29][30]. Previous proposals also typically relied on astronauts or primitive robots with astronaut supervision to assemble the structure. Yet, current robots are now capable of complex autonomous tasks with only ground-based human interaction, eliminating the need for astronauts and thus significantly reducing the cost of the mission [31][32]. With these advancements, large robotically-assembled optical space telescopes are feasible, as suggested by more recent proposals [33][34][35]. In one such proposal, the primary mirror is composed of individual cubesats, each equipped with a deformable mirror segment [36]. The cubesats would be unconnected for launch, then navigate into position and dock together to form the backplane. The mirror segments would then deform to the right shape based on their location, creating the full aperture. A flight demonstration of this concept, including docking of the cubesats and deforming of the mirrors, is scheduled for launch in 2018. The use of autonomous cubesats is a departure from the previous modular concepts, in which relatively passive modules would be assembled by a centralized robot or crew. Equipping each

module with a propulsion and guidance system may severely and unnecessarily increase mass and complexity. Keats Wilkie et. al. proposed a concept for an optical PM composed of passive deployable modules, each with a pre-attached blank mirror facet. On orbit, a crawling robot would connect these modules and machine the facet surface to the correct shape [37]. While this concept belongs to the current state of the art for large optical space telescopes assembled from passive modules, it still has limitations. For instance, rather than employing deformable mirror technology, a complex micromachining process would be required to obtain the correct shape of each mirror segment, with actuators in the truss structure maintaining precision during operation. Furthermore, since the truss module and mirror segment would be attached before launch, the deployment scheme must maintain the face of the segment, eliminating schemes that may have greater packaging efficiency. Thus, an open research area is identified: the development of a novel, feasible architecture for an optical space telescope that is sufficiently too large to be deployed and must be assembled on-orbit. The architecture should draw from the current body of research, yet also incorporate currently existing but recently developed technologies, establishing an innovative framework suitable for future flight missions.

The literature survey of previous assembled space telescope concepts reveals one common, well-established architecture that is easily adapted for current technologies: the use of many deployable modules assembled by a centralized robot or crew. Larger modules divide the structure into fewer assembly steps and thus reduce assembly time, and folding those modules for launch increases packaging efficiency. Within this common theme, the design of the modules varies widely among the proposals. Some modules deploy purely by spring action, while others require complex motor systems that are either self-deployable or are partially actuated by the assembly robot. Entirely passive deployable concepts are ideal, avoiding the power consumption, mass, and complexity of motors. However, there is anecdotal evidence that spring-actuated deployable structures are difficult to control and unreliable, with even small fabrication and assembly errors causing unpredictable hinge latching sequences that hinder deployment. Little work has been done to quantify the reliability of these deployment schemes, defined in this context as the likelihood that a given module with a random set of errors will deploy successfully. In previous literature, reliability is typically a mere qualitative description with no analytical backing. If analysis is presented, it is often limited to the ground-based or in-orbit testing of one module or simple kinematic numerical models [38][39]. Some higher fidelity models have been developed specifically to obtain reliability

estimates, but these models only consider errors in the driving torques of the actuating mechanisms, not in the geometry of the structure [40]. Depending on the size of the primary mirror, hundreds of these modules may be required, all likely manufactured in bulk with standard precision levels to remain within budget. Even if the deployment of each module is then tested before launch, an assuredly expensive endeavor, the entire structure may need to be redesigned if the deployment scheme proves unreliable, resulting in severe setbacks late in the mission development timeline. Thus reliability is an important mission constraint that must be quantified early in the design process, identifying another open research area. First, exactly how the errors affect the deployment must be understood, requiring the development of new high-fidelity simulation modeling techniques. Then these simulations should be used to optimize the module design and set the manufacturing tolerances needed to meet reliability requirements.

After a module is deployed, the next task is connect it to other modules and assemble the backplane. According to Ribble and Woods, the module assembly "will probably provide the largest single challenge to the construction of large space structures" [17]. The challenge is in part due to the same fabrication errors, which will still be present even if the deployment was successful. As the backplane is assembled, these errors may compound and amplify, requiring large forces to complete the structure and potentially yielding a final shape that does not meet precision requirements. In the early 1980s, John Hedgepeth developed a back-of-the-envelope analytical expression for computing the ratio of the final precision of a truss backplane to the precision of its components, a measure of how much errors are magnified after assembly [41]. In this expression, precision is inversely proportional to the backplane diameter, suggesting that errors grow during assembly. While this ratio is certainly an important metric, the simple analytical approach cannot provide other critical information, such as the stresses in the truss members after assembly. This information was obtained with a statistical approach by Hedgepeth later in 1989 [42]. A finite element model of a nearly completed structure with random fabrication errors was created, from which the equilibrium shape was obtained. From the shape, the distance between the final connection points and the force required to bring the points together was calculated. While this approach yields more information about the final structure, it loses any information about the assembly history. Recently, a new algorithm has been developed using robotic mapping principles and techniques to predict errors during assembly [43][44]. This algorithm does predict that errors grow with the number of connections. However, it can only be used to analyze

truss-like rigid elements, and it is possible that the inclusion of realistic material properties and flexibility in the truss members may yield a different result. No matter what error magnitudes are encountered during assembly, the interconnects between modules must form a precise and stiff connection. As with the module designs, the interconnect designs vary widely in style and complexity among previous proposals. One more common design features a relatively simple interlocking cup/cone system [37][36][23]. Yet, limited or no analysis has been performed to demonstrate successful coupling of these interconnects despite fabrication errors. Thus, a third research area is identified. How the errors interact and grow during assembly must be understood, requiring the development of a new technique to simulate the step-by-step connection of truss modules with realistic material behavior. This technique can then be used to determine the maximum expected error at any connection point in the backplane given a general assembly plan. The interconnect design must ensure that a full connection can be made even with this maximum error. The complexity and style of interconnect needed to meet this requirement must be investigated.

In summary, three research goals have been established. First, *a new concept for on-orbit assembled large optical space telescopes* must be proposed that effectively modernizes modular deployable schemes of the past with current robotics and adaptive optics technology. Second, *a method for quantifying deployment reliability* is required to inform the truss module design, propose a set of manufacturing tolerances, and prove that the deployment is unhindered by fabrication errors. Finally, *a technique for simulating the assembly* of flexible truss modules with fabrication errors must be developed to investigate the feasibly of simple interconnect concepts and propose a new set of manufacturing tolerances if the assembly proves more constraining than the deployment. This thesis addresses each of these research goals and therefore delivers a comprehensive and demonstrated feasible architecture for future generations of space telescope missions.

1.2 Thesis Outline

Chapter 2 of this thesis introduces the In-Space Telescope Assembly Robotics (ISTAR) architecture for L2-orbiting optical telescopes with aperture diameters ranging from 20 m to 100 m. In this architecture, the primary mirror is assembled by a six-limbed robot with significant on-board autonomy, modeled after JPL's RoboSimian [31]. Like ground-based telescopes HET and SALT, the primary mirror is spherically curved and composed of identical mirror segments. Each

segment is backed by a rigid body actuator to correct any large, quasistatic errors, while small, dynamic errors are corrected by the deformable mirror segments that comprise the secondary optics. The primary mirror is uniquely divided into two types of modules: mirror modules, or groups of mirror segments, actuators, and electronics; and deployable truss modules. The mirror modules and truss modules are initially unconnected and launched separately, allowing greater freedom in the truss module design. The truss geometry is a modified version of the PACTRUSS, selected for its packaging efficiency, and uses a combination of Rolamite tape spring hinges and control from the assembly robot to actuate a smooth deployment. The specific truss module design is chosen to maintain the precision requirements set by the capabilities of the wavefront control system. The design methodology is similar to those found in previous proposals, employing simple analytical techniques for estimating the magnitudes of relevant space environment loads and their effect on the structure [45][37][46][47]. On orbit, the robot first constructs the backplane by deploying and connecting the truss modules, then mounts the mirror modules onto the supporting backplane to safely and efficiently complete the primary mirror.

Chapter 3 presents the deployment reliability estimation toolkit designed to estimate deployment reliability. While the toolkit was developed in the context of the ISTAR module, it can easily be adapted for any truss geometry or deployment scheme. At the core of the toolkit is the detailed deployment simulation of one specific truss module, performed using the finite element software Abaqus [48]. At the next level is a Python shell that rapidly performs many deployment simulations, each of the same nominal truss module but with a different set of randomly chosen fabrication errors with specified manufacturing tolerances. The number of successful deployments out of the total then provides an estimate for the reliability of that design with those tolerances. At the highest level of the toolkit is another Python shell that allows one module design parameter or manufacturing tolerance to be varied, determining the effect of that parameter on reliability. Thus, the toolkit is capable of producing a thorough set of trade studies, which can be used to optimize the truss module design and determine the required manufacturing tolerances for 100% reliability.

The experimental validation of the deployment simulation is described in Chapter 4. A 1/6th representative section of the ISTAR truss module was physically constructed and its final shape was carefully measured. The module was then deployed several times, while tracking select nodal displacements and hinge rotations.

Using the shape measurements, the module was reconstructed as closely as possible in the simulation model, and the same nodal displacements and hinge rotations were obtained. The results showed satisfactory agreement between the simulated and experimental quantities, suggesting that the simulation accurately models deployment behavior.

As described in Chapter 5, the fully developed toolkit was finally applied to the ISTAR truss module. The individual effects of different types of errors were first investigated and the tolerance required to achieve 100% reliability was determined for each error type. The relative difficulty of achieving each tolerance was compared, giving insight into which error is most detrimental for reliability and what parts of the module need to be manufactured most precisely. Next, using these tolerances, all of these error types were applied simultaneously, which drastically reduced the reliability to far below acceptable limits. From this baseline, selected design parameters, including the truss member outer diameter, member wall thickness, and Rolamite hinge moment, were varied and their effect on reliability was recorded. The results of these trade studies showed that the most effective way to achieve 100% reliability without impacting other structural properties and mass was to simply to increase the hinge moment. With this information, a final set of manufacturing tolerances were proposed, all within the capabilities of standard manufacturing processes.

Chapter 6 focuses on the detailed assembly of the modules given that fabrication errors will still be present after deployment. In the ISTAR architecture, the modules are assembled in concentric rings around a central hub, which is connected to the spacecraft that drives the primary mirror. In each assembly step, the module currently held by the robot may connect to one, two, or three adjacent modules, depending on its location in the backplane. A new simulation technique is presented that sequentially adds modules, each with a unique set of fabrication errors, to the backplane. In each assembly step, the module currently being added is forced into alignment with the adjacent modules. Then physical connections are made, the alignment constraints are relaxed, and the structure is allowed to reach an equilibrium state. The technique was applied to the ISTAR assembly, and three quantities were tracked: the final surface precision of the backplane, the stresses in the members, the initial distance between each interconnect half before alignment. The results clearly showed that surface precision decreased as the backplane size increased. Furthermore, to maintain safe stress levels and precision requirements,

the manufacturing tolerances had to be greatly reduced from the levels suggested based on deployment reliability. This information was then used to investigate the viability of a simple interconnect concept featuring a magnetic interlocking cup and cone system. The assembly of one module with fabrication errors was simulated using detailed models of the interconnects. In this simulation, the cups and cones could not fully engage, with unacceptably large residual distances caused by bending in the structure. To improve the result, a two-stage locking system was proposed. In the first stage, called the "soft capture", the interconnects would be allowed some movement in relation to the module, facilitating contact between the cups and cones. In the second stage, once the cups and cones have fully engaged, all further movement would be restricted and the structure would become rigid. The soft capture was modeled by adding appropriate springs to the simulation. The results showed that, while the residual distances between the cups and cones were greatly reduced, they were still non-zero. The conclusion is that the system is possibly too overconstrained. To ensure full engagement, the interconnect will likely need to be much more complex, relaxing degrees of freedom entirely during assembly and becoming rigid after the connections have been made.

Chapter 2

THE ISTAR ARCHITECTURE

This chapter presents the ISTAR architecture for robotically-assembled optical space telescopes with aperture diameters between 20 m and 100 m, initially proposed by members of the JPL and Caltech community in an effort to explore a possible application for newly developed robotics technology. The architecture is entirely modular, cost effective, easily assembled, and can even be expanded to sequentially increase the aperture size over a series of mission stages as budget and technology readiness allows. In this chapter, the overall optical scheme and components of the telescope are first presented. Focus is then shifted to the concept of the primary mirror, the largest component of the system. The modules that comprise the primary mirror and the plan for robotically assembling those modules is outlined. The module design process is then detailed, using structural and thermal analyses to ensure that precision requirements are met under expected loads given currently existing wavefront sensing and control technology.

Some of the content in this chapter has been adapted from: Kristina Hogstrom et al. "A Robotically Assembled 100-meter Space Telescope." In: *65th International Astronautical Congress*. 2014. The contributions of specific authors are clarified in Section 2.6.

2.1 Optical Scheme

The ISTAR concept is a segmented, steerable, UV to near IR telescope robotically assembled in space. Figure 2.1 shows the basic layout of the telescope and its four main components: the sunshade, primary mirror (PM), spherical aberration corrector (SAC), and metrology system. In the figure, D_{pm} is the effective aperture "diameter," approximately the vertex-to-vertex dimension of the hexagonal PM, and R_{pm} is the radius of curvature of the PM. Given the large size of the telescope, each of these components is structurally separate and formation flown, with its own power, thermal control, and propulsion system that maintains formation.

The optical design borrows from that of the ground-based Hobby-Eberly Telescope (HET) and Southern African Large Telescope (SALT) by utilizing a spherical curvature primary mirror [1][2]. The PM acts as a “precision light bucket,” and

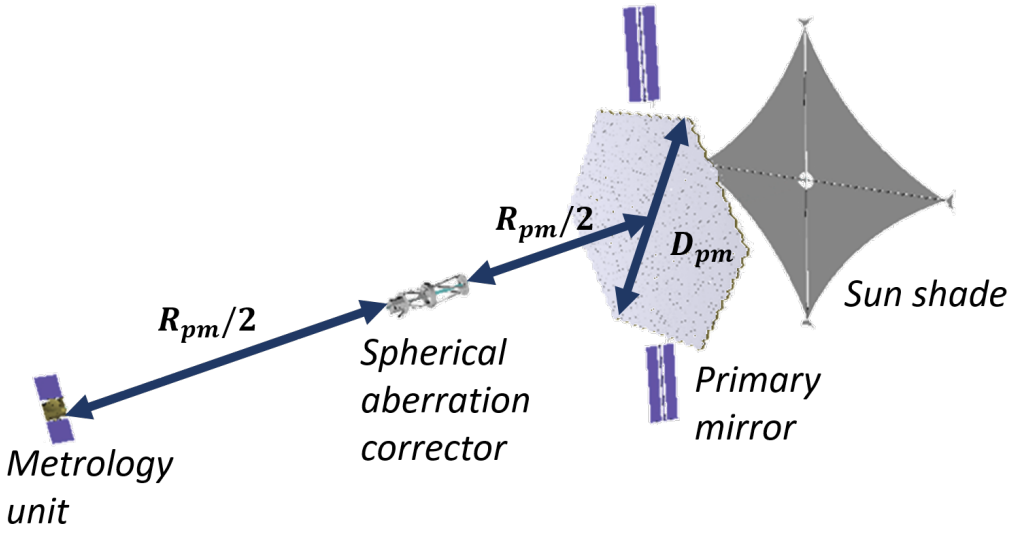

Figure 2.1: Illustration of the ISTAR telescope and its components.

is phased into a diffraction-limited telescope at the exit pupil inside the SAC using a technique described by Meinel et. al [49]. One key advantage of this design is that the majority of the wavefront sensing and control (WFSC) and the only active deformable mirrors are offloaded from the PM to the much smaller optics in the SAC. The PM segments are identical, manufactured in bulk, and only require tip-tilt control, sharply reducing mirror fabrication costs, which is one of the most significant cost drivers in observatories. The SAC mirror segments have the same basic characteristics, but are deformable with μm-level actuation range and can correct down to nm-level. The baseline mirror segments are drawn from currently available technology, and are assumed to have a hexagonal shape with vertex-to-vertex length of 1.35 m.

Since the segments are hexagonal, the PM is also approximately hexagonal, with discrete allowable values of D_{pm} as determined by the number of mirror segments and how they are packed. The exact definition of D_{pm} will be explained in Section 2.4, but the largest value considered in this architecture is 105 m. The radius of curvature R_{pm} is set to $8D_{pm}$. The resulting focal length of $4D_{pm}$ is significantly longer than that of most telescopes, because typically it is limited by the structural connection between the PM and secondary optics. In this architecture, these components are formation flown, and so the structural limit is not applicable. Longer focal lengths are more desirable, since they afford better optical tolerances and smaller secondary optics.

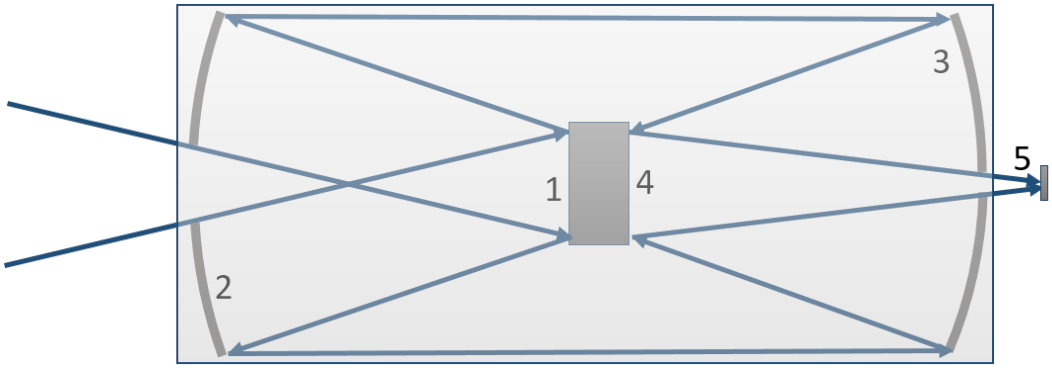

Figure 2.2: Ray trace diagram of the SAC. Light from the primary mirror enters through the opening on the left and is reflected by flat surface 1 onto clamshell mirror 2. The ray then reaches clamshell mirror 3 and is reflected to flat surface 4 and finally to the detector at location 5.

The SAC is located at the focal point of the PM, for a separation distance of $4D_{pm}$. It includes two clamshell aspheric mirrors, with diameter and separation distance dependent on the size of the PM. For the largest design, these values are 8.6 m and 24.4 m respectively. This size is assumed to be within the range of deployable methods and so the SAC is not robotically assembled in this architecture. A ray trace diagram is shown in Figure 2.2. Another major advantage of the spherical aperture is that the SAC can be moved relative to the PM to observe a new target within a certain field of regard, without having to slew the whole telescope. This enables rapid transition to a new observation, saving time and fuel. For the largest design, the field of regard ϕ_{field} is 7.16°. The locus of motion of the SAC with respect to the PM is a spherical surface with half the radius of curvature and half the span as the PM, as shown in Figure 2.3. In the nominal position, the SAC is centered and the entire PM is visible. However, when the SAC is positioned at the limit of its range of motion, only about 40% of the PM can be seen, as shown in Figure 2.4.

The metrology system is located at the center of curvature of the mirror. It contains a Zernike wavefront sensor and an Array Hetroydyne Interferometer to precisely measure the shape and phase of the primary mirror segments.

The sun shade design borrows from deployable solar sails like Sunjammer [50]. Four deployable masts extend from a central hub radially outward, carrying the corners of a lightweight membrane until it is taut. In order to fully shield the primary mirror, each of the masts must extend to at least $\sqrt{2}D_{pm}/2$, or 75 m for D_{pm} = 105 m. The Shuttle Radar Topology Mission, launched in 2000, used a 60-m mast built by ATK [51]. Thus, a 75-m mast is conceivable with currently existing

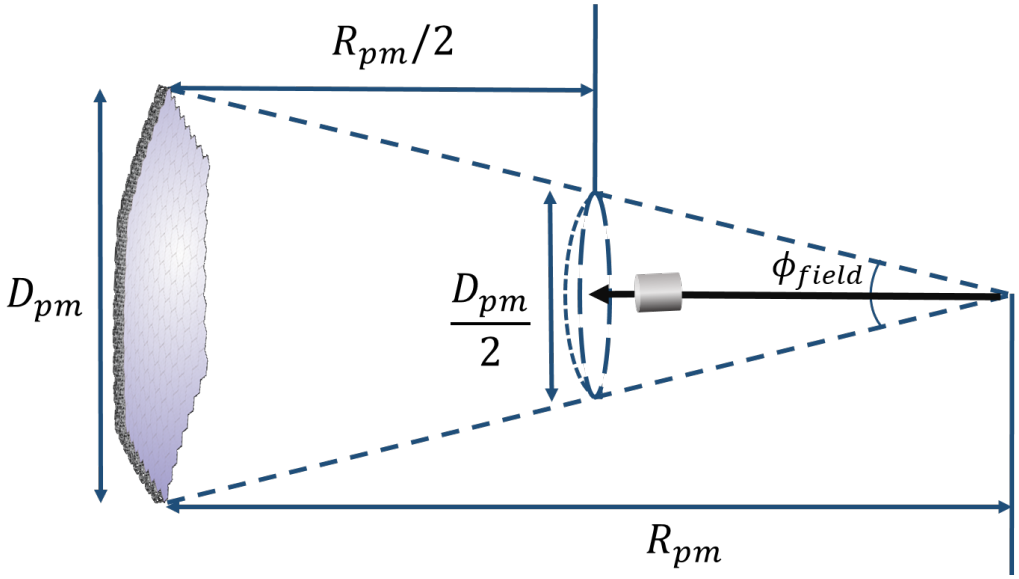

Figure 2.3: Sketch highlighting the SAC motion required to point to a new target without slewing the primary mirror.

technology. The membrane material and surface properties must be chosen based on thermal constraints that will be described in Section 2.5.

2.2 Primary Mirror Assembly

The primary mirror is the largest component of the telescope and thus the focus of robotic assembly. A representation of the ISTAR robot needed to assemble the mirror is shown in Figure 2.5. The robot will be commanded from Earth, but with significant on-board autonomy to minimize the bandwidth of communications to a human operator. The resulting supervised autonomy system will enable the Earth-based operator to specify high-level commands, while the robot performs all sensor-based motion and complex tasks autonomously.

Drawing upon the development of the Lemur and RoboSimian robots at JPL, the ISTAR robot is anticipated to have six appendages [31][32]. During assembly, two of these appendages can be used for dexterous manipulation while the other appendages remain attached to the structure. All six appendages can be used to walk on the structure. Perception and dexterous manipulation technologies that will be needed have been demonstrated in a laboratory environment at JPL [52]. The robot is battery powered and can be charged from the PM power grid.

The PM consists of two layers: the mirror layer, which includes rigid body actuators and electronics, and a truss backplane structure that supports the mirrors.

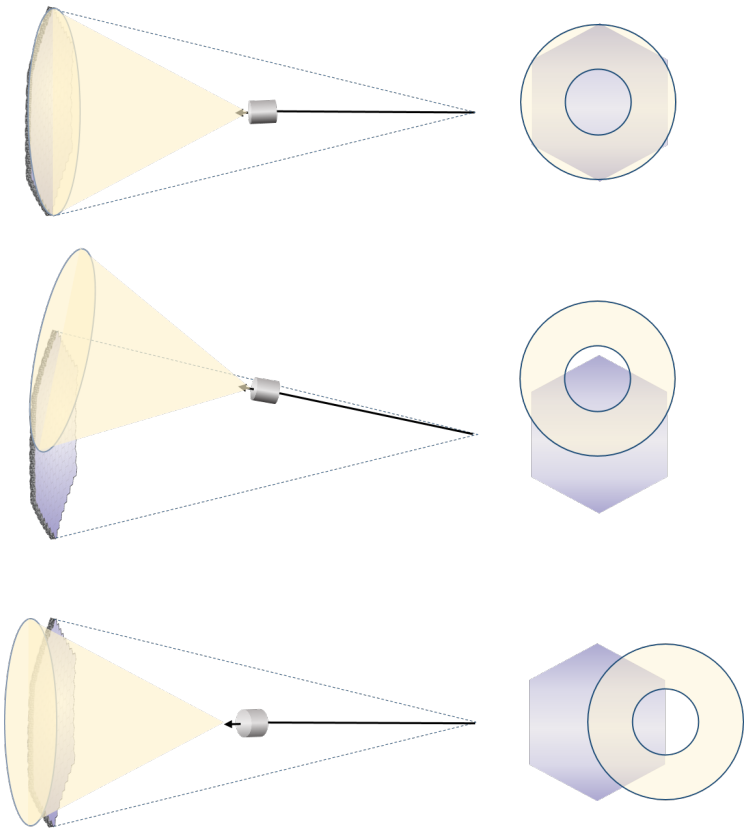

Figure 2.4: Diagram of what portion of the primary mirror is visible to the SAC when it is centered (top) and $\phi_{field}/2$ from center in two different directions (middle and bottom, respectively). A side view of the telescope is shown left and a top view is shown right.

Because the PM is spherical, all mirror segments can be identical, enabling a highly modular structure. Groups of segments and their actuators are hexagonally packed into a cluster called a *mirror module*. Each mirror module is backed by a rigid plate which features structural and power connectors. Given the complexity and fragility of the segments and associated electronics, mirror modules are assembled on the ground by humans and launched as a package.

The truss backplane layer is divided into hexagonal *truss modules*, which are deployable structures sized to match one mirror module when fully deployed but can stow compactly for launch using internal hinges. An assembled mirror module and truss module are shown in Figure 2.6. Each truss module is equipped with structural and power connectors located at the ends of each vertical member, with internal wiring throughout the members to transmit power. These connectors are structurally adjustable by the robot to ensure proper alignment between modules.

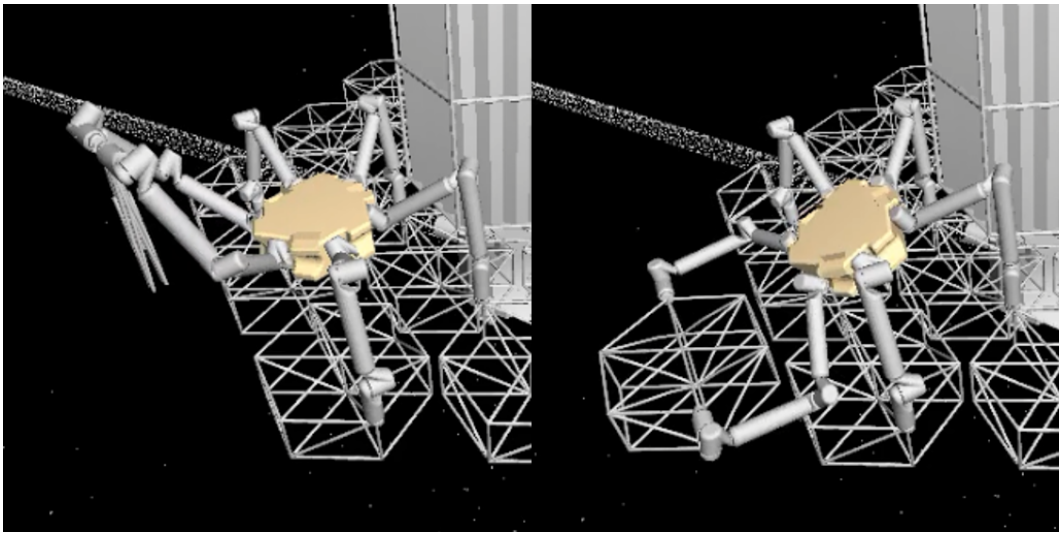

Figure 2.5: Depiction of a ISTAR robot with six appendages. In this image, the robot uses two appendages to deploy a truss module, while the remaining four are fixed to the structure.

The vertices on the top surface of each module are equipped with ball-like features which the robot can grasp while walking.

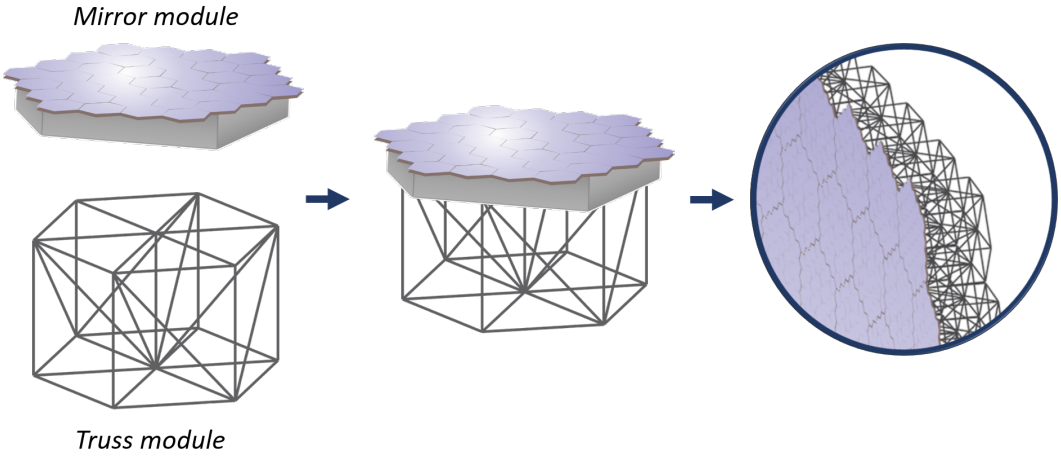

Figure 2.6: Depiction of a mirror module and truss module as one unit of the primary mirror.

In space, the robot retrieves the first folded truss module from a central canister and deploys it so that the internal hinges lock. The robot then attaches the truss module at the connection points to a central hub that is rigidly mounted and wired to the spacecraft that drives the PM. The robot then continues to assemble truss modules in concentric rings around the central hub. Once the backplane is complete, the robot begins assembling mirror modules, interfacing only with the rigid plate to

avoid the sensitive mirror segments. In the same concentric ring pattern, the mirror modules are attached to the backplane, not to other mirror modules, to avoid stress build-up. The module assembly process is summarized in Figure 2.7.

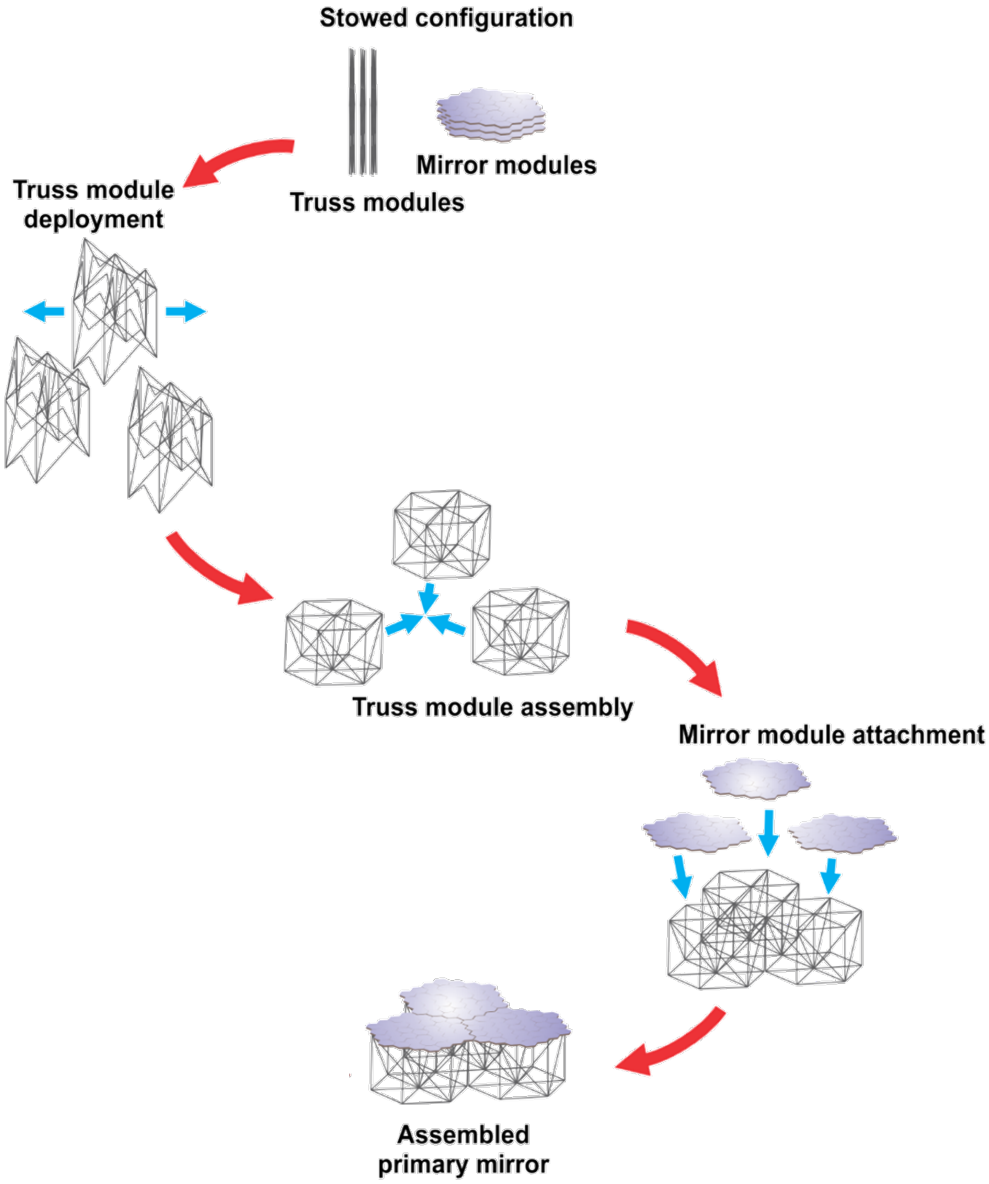

Figure 2.7: Illustration of the ISTAR assembly process.

It is unlikely that the truss modules will need to be serviced. However, mirror segments are sensitive and may encounter issues (e.g. meteoroid hits). Servicing of individual segments may be too complex for the robot, so instead the entire mirror module can be replaced. The connectors that attach the mirror module to the backplane will also be able to detach as needed.

2.3 Mission Requirements

The wavefront sensing and control system has two levels of correction, with ranges consistent with the current state-of-the-art. First, the primary mirror segments are backed by rigid body actuators for removing quasistatic errors due to inertial loads, such as thermal gradients. These actuators can correct errors up to 10 mm and bring the system to μm-level precision. Then the active mirrors in the SAC can remove any dynamic errors up to μm -level, correcting down to nm-level. The telescope design must ensure that errors remain within these ranges of correction.

Along with the precision requirements, the following other functional requirements must be met:

- The telescope shall be operable no more than three minutes after a slew maneuver.
- The telescope shall operate at temperatures between 240 K and 300 K.
- The primary mirror shall have an areal density less than 30 kg/m^2. The areal density of the mirror segments and actuators is estimated to be 25 kg/m^2; thus, 5 kg/m^2 is allotted to the truss structure.
- Mirror segments shall have a gap of 100±10 mm to facilitate the ball-like features that the robot uses to walk on the mirror surface.
- The telescope shall nominally operate in an orbit around the second Lagrange point (L2).

The most customized parts of the architecture are the truss and mirror modules. Their design, described in the remainder of the chapter, is based on these requirements.

2.4 Mirror Module Design

The mirror modules are all identical. Their geometry is based on the following key considerations:

- The module contains $n_{s,m}$ identical, spherical mirror segments arranged according to a hexagonal tessellation.
- The value of $n_{s,m}$ is chosen to be as large as possible to maximize launch capacity, so that the modules can be stacked inside a payload fairing.

- The gaps between the mirror segments are 100±10 mm to facilitate robotic mobility, as stated in Section 2.3.
- The gap size between segments must vary to allow the hexagonal segments to lie on a spherical surface.

Figure 2.8 shows three choices for $n_{s,m}$: 7, 19, and 37 segments. With the nominal 100-mm gap between segments, these designs yield maximum mirror module dimensions of 3.77 m, 6.28 m, and 8.81 m respectively. Since the proposed SLS launch vehicle will have a payload fairing with an outer diameter of 8.4 m, the $n_{s,m} = 19$ design was chosen [9].

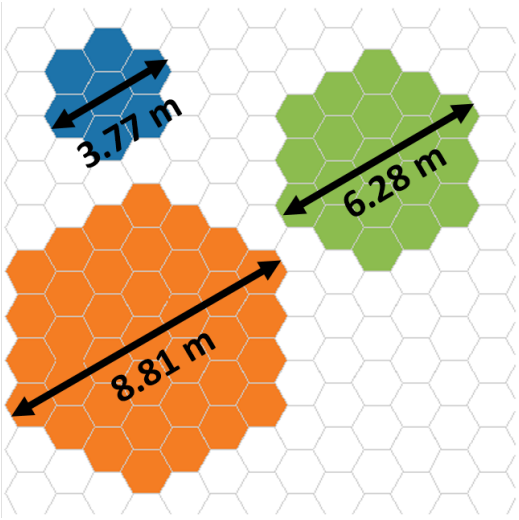

Figure 2.8: Choices of number of mirror segments per mirror module.

The mirror module size dictates the possible values of the approximate aperture diameter D_{pm}. Given n_m, the number of modules on a side of the full hexagon, D_{pm} is defined as the distance between the vertices of the two outermost segments, as shown in Figure 2.9. With a nominal 100-mm gap, Table 2.1 gives the value of D_{pm} as a function of n_m.

n_m	3	4	5	6	7	8	9	10
D_{pm} [m]	27.9	38.9	50.0	61.0	72.1	83.2	94.3	105.3

Table 2.1: Values of D_{pm} possible with the mirror module design.

Generally, close-packed hexagons cannot be tiled onto a spherical surface. Thus, the curvature of the mirror requires variable gap sizes between the mirror segments.

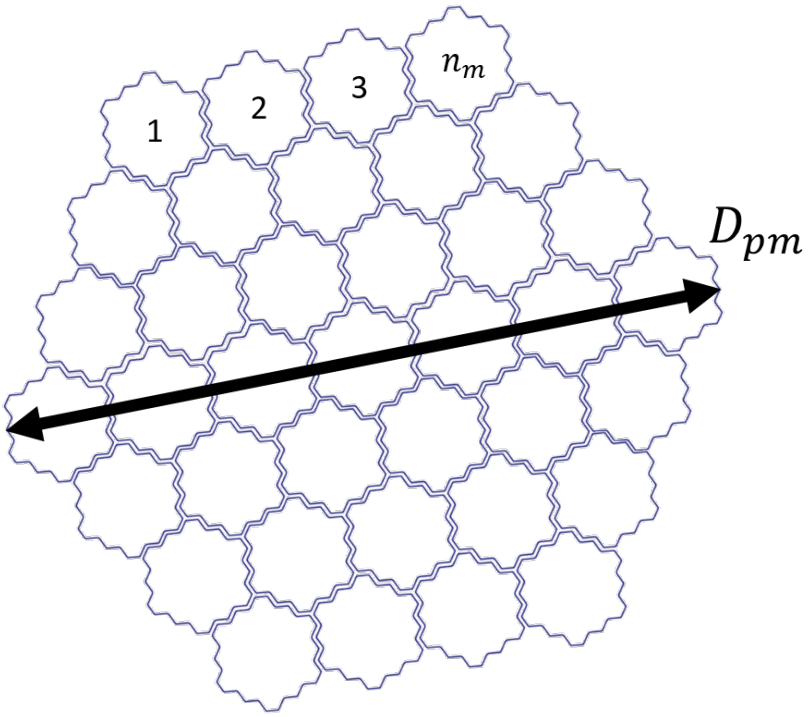

Figure 2.9: Definition of the aperture diameter based on the number of mirror modules on a side of the hexagon. A design with four modules on a side (n_m = 4) is shown.

The distribution of the gap size is a design parameter that has been studied in detail. An algorithm to place the segments on a spherical surface while imposing different constraints on the gap variations was developed by Lee et. al [53]. A solution was obtained in which the gap sizes between mirror segments within a mirror module vary by no more than 1.7 μm, with the distribution being identical for all mirror modules. The gaps between one mirror module and another mirror module were also minimized with this solution, with values ranging from 98 mm to 101.3 mm. This result is well within the required tolerance of ± 10 mm.

The mirror modules will be assembled on the ground, incorporating the variable gap distribution that has been calculated. The variation in the larger gaps between modules must be created during assembly. To accomplish this, the interconnects between modules will be adjustable by the robot, with a range up to 1 cm. Note that the gaps between the modules increase linearly with depth through the truss thickness, and hence will be larger on the back side of the truss than on the front. However, because the radius of curvature is much larger than the depth of the truss, the difference is still well within the range of the adjustable connectors. These gaps will necessarily lead to eccentricities in the structure, such that member center lines

between neighboring modules will not intersect at the joint. The effect of these gaps on the structural integrity will be addressed in Section 2.5.

2.5 Truss Module Design

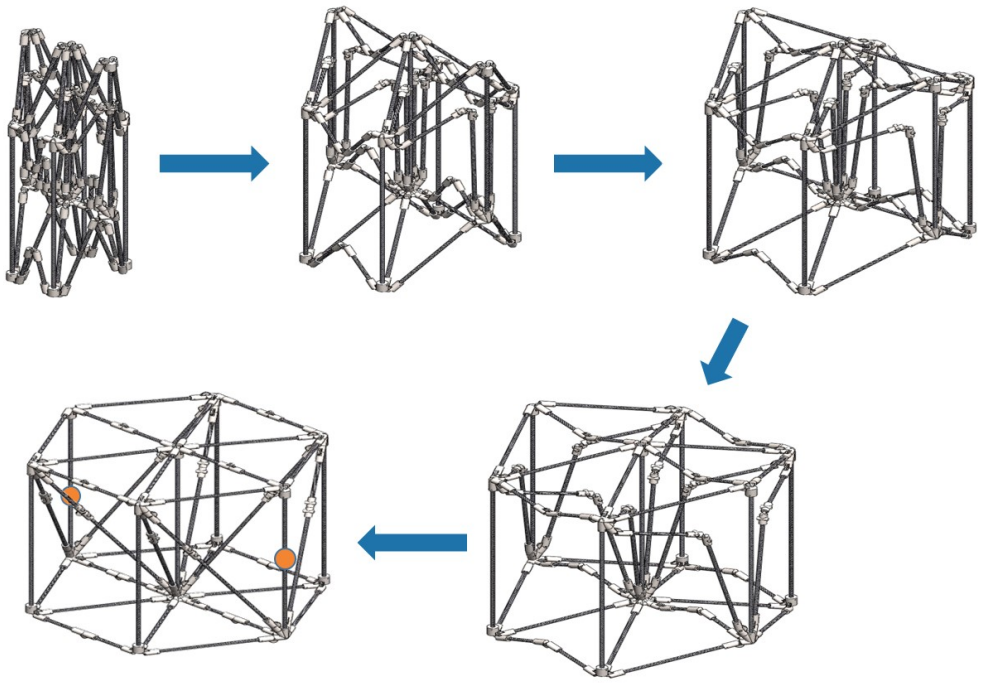

Figure 2.10: Truss module deployment. The points at which the robot holds the module are marked with the orange circles in the final deployment stage.

The truss geometry must facilitate a compact storage profile and a smooth deployment. The overall shape must also be hexagonal to match the shape of the mirror module. A modified version of the PACTRUSS deployment scheme was selected over the more traditional tetrahedral geometry, because of its improved packaging efficiency. PACTRUSS was developed by Aerospace Corporation specifically for large precision telescope structures [54]. It was originally intended to provide an entirely deployable telescope backplane, consisting of many hexagonal unit cells simultaneously unfolding. This design was analyzed to show that it could maintain sub-micron precision under operational loads when fully deployed. However, deployment simulations revealed difficulties in controlling the order in which the many hinges latched [54]. The ISTAR concept removes this uncertainty, because only one hexagonal unit cell is required for the truss module, greatly reducing the number of hinges that must act simultaneously. The module and deployment scheme are shown in Figure 2.10. The unit cell consists of 39 members: the 12 longerons that

make the hexagonal face on each side (24 total), seven verticals, four face diagonals, and four internal diagonals. The diagonals and eight longerons are hinged in the center. In the compact state, the truss module folds like a bundle of rods, and thus the stowage footprint is determined by the hinge offsets and the outer diameter of the members.

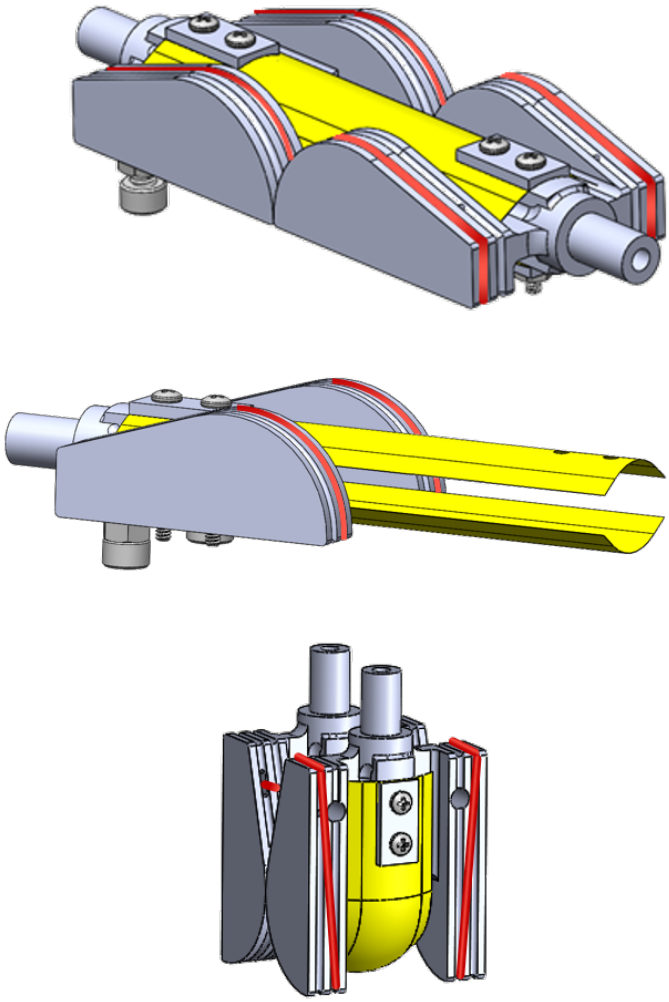

Figure 2.11: Rolamite hinge shown deployed (top), deployed with one cam set cut away to see the detail of the tape pair (middle), and folded (bottom). The tensioning wire is sketched in red.

Each of the eight mid-member folds are equipped with Rolamite tape spring hinges. These hinges are composed of two ordinary measuring tape sections and two sets of two cams constrained to roll on each other about one axis, as shown in

Figure 2.11. A pretensioned wire wraps around the two separate cam sets, holding them together and further constraining the degrees of freedom for smooth unfolding. The wire wrapping and tensioning mechanism are diagrammed in Figure 2.12. The hinges can fold such that the attached members are parallel, self-deploy, and firmly latch in the fully open position with high bending stiffness. The behavior of these hinges has been studied extensively and is discussed in Section 3.1 [55]. The hinges are sized so that the truss module can deploy purely by spring force. However, during deployment, the robot holds the centers of opposing vertical members, controlling their displacements and working against the hinges for a slow, quasistatic deployment. This is to mitigate the uncertainty and fluctuations in reaction forces and internal stresses that may be associated with dynamic effects and vibrations. The centers of the vertical members are controlled to minimize the reaction forces caused by the Rolamite hinges and avoid eccentricities that may result in stress concentrations. These control points are marked in Figure 2.10.

The truss module dimensions are defined in Figure 2.13. In order to reduce the number of redundant members, the truss modules are rotated with respect to the mirror modules, rather than hexagonally packed, as shown in Figure 2.14. The value of the side length L must match this tessellation pattern, governed by the mirror module size. For $n_{s,m} = 19$ as chosen, $L = 2.76$ m.

M55J carbon fiber composite (CFC) has been selected for the truss material, because of its high stiffness and low density [56]. It has an elastic modulus E_m of 340 GPa, a density ρ_m of 1620 kg/m^2, a coefficient of thermal expansion α_m of $1.1 \times 10^{-6}/°$C, and a thermal conductivity k_m of 156 W/m. The remaining design variables are the truss depth H, the member outer diameter d_o, and the member wall thickness t. These variables control the structural response to external loads, and must be chosen to ensure that all of the precision requirements for the PM are met. The loads at L2 are benign compared to low Earth orbits; there is no gravity gradient or air drag, and the thermal environment is relatively stable. Furthermore, since the telescope is expected to always point away from the Sun, solar pressure will be approximately uniform across the back of the PM, and so any resulting torques or elastic deformations are negligible. The two major external loads are thus time-invariant temperature gradients and dynamic disturbances due to reaction wheels, slewing, and other random vibrations.

The magnitudes of these loads and their effect on the PM generally vary with the aperture diameter. In order to simplify the architecture and allow for an expandable

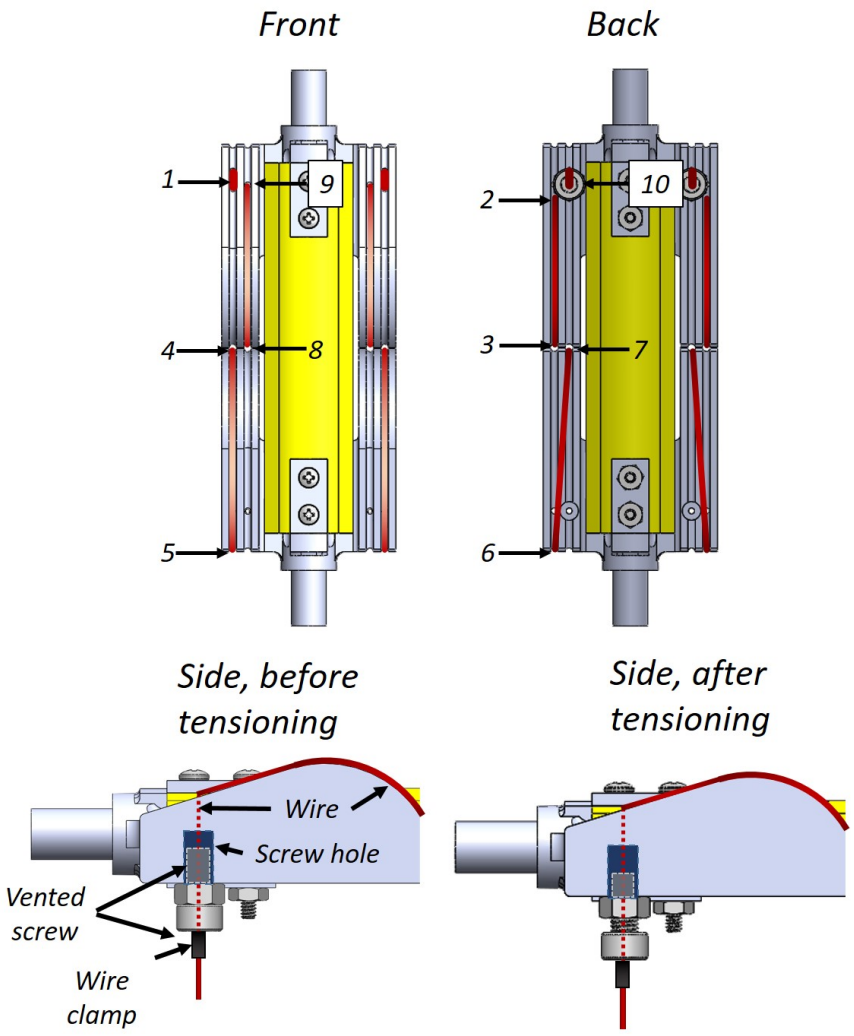

Figure 2.12: Diagram of the Rolamite wire wrapping. The start of the wire is clamped at location 1 on the front surface and is immediately threaded through a hole to the back surface, emerging at location 2. It runs along the back of the hinge in the outer channel until location 3, where it is pulled through to the front surface between the cam sets at location 4. It then runs along the circular surface of the cam to location 5, where it wraps around to the back side at location 6. The wire then crosses over to the inner channel and is once again pulled through to the front at location 7, emerging at location 8. Finally, at location 9, it is threaded through a hole in the cam section and then through a vented screw. As shown in the side view, the screw is initially threaded through a nut, such that the nut is flush against the cam surface and the screw is flush against the nut. The end of the wire is clamped firmly in this position at location 10. The nut is then turned to extend the screw away from the cam surface, thereby applying tension to the wire.

mission as previously described, only one module design is proposed that meets the precision requirements for any aperture diameter within the range. The selected

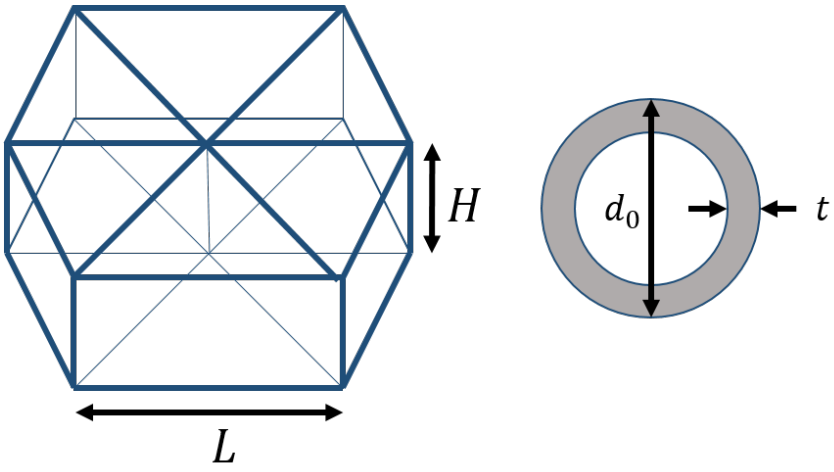

Figure 2.13: Geometric variables of the truss module, with the member cross-section shown right.

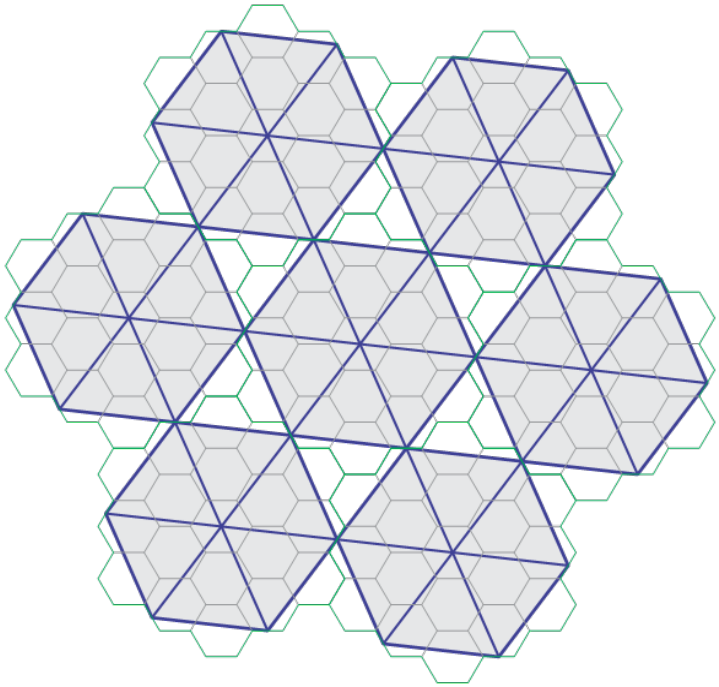

Figure 2.14: Depiction of mirror module tiling (green outline) vs. truss module tiling (purple outline).

design has a depth H of 2.76 m, a member outer diameter d_o of 35 mm, and a member wall thickness t of 3 mm. The areal density of the truss alone is approximately 3 kg/m^2, leaving 2 kg/m^2 for connectors and hinges. Setting the depth equal to the side length L not only satisfies the precision requirements, but also avoids complications in deployment and manufacturing caused by significantly varying

member lengths. The following subsections describe the analyses performed to estimate the magnitudes of the loads and the response of the backplane. The results were compared to the capabilities of the control system, and the process iterated to select the truss module design.

2.5.1 Thermal Effects

For the thermal analysis, the design variables include not only the truss module geometry, but also the coating on the underside of the mirror surface and the amount of solar radiation blocked by the sun shade, all of which may vary to ensure that requirements are met. The bulk thermal requirement is that the primary mirror must operate at 270±30 K. However, one of the most detrimental thermal effects is a change in curvature of the primary mirror, which arises from a temperature difference through the PM thickness, or from the mirror surface to the bottom of the truss backplane. The rigid body actuators, with a range of 10 mm, can correct for this type of error.

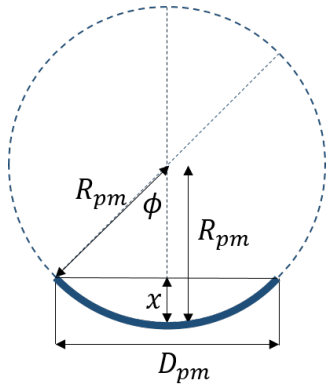

Figure 2.15: Definition of the sag value x. D_{pm} is the arclength defined by twice the angle ϕ on the circle of radius R_{pm}.

When the curvature changes, the sag of the mirror changes. The sag x is the height difference between the mirror edge and mirror center, as shown in Figure 2.15. In this case, the aperture diameter D_{pm} is defined as an arc length on the circle of radius R_{pm} that subtends angle ϕ. This is to ensure that, as R_{pm} changes, the length of the mirror neutral axis stays constant. Since ϕ is small (approximately 3.5°), the sag x is approximately $(D_{pm}/2)^2/(2R_{pm})$. The rigid body actuators can account for a change in sag Δx_{max} of 10 mm. The corresponding maximum change in curvature ΔK_{max} is given by

$$\Delta K_{max} = \Delta\left(\frac{1}{R_{pm}}\right) = \frac{2\Delta x_{max}}{(D_{pm}/2)^2}\,. \tag{2.1}$$

The curvature is then related to the temperature differential by the truss depth H and material expansion coefficient α_m:

$$\Delta T_{max} = \frac{\Delta K_{max} H}{\alpha_m} . \tag{2.2}$$

Substituting Equation 2.1 into Equation 2.2 yields the maximum allowable temperature difference in terms of the truss depth H, given that dx_{max}, α_m, and D_{pm} are known:

$$\Delta T_{max} = \frac{8 \Delta x_{max}}{D_{pm}^2 \alpha_m} H . \tag{2.3}$$

Clearly, ΔT_{max} decreases and the requirement becomes more stringent as D_{pm} increases. For the largest design ($n_m = 10$) with $H = 2.76$ m, $\alpha_m = 1.1 \times 10^{-6}/°\text{C}$ and $dx_{max} = 10$ mm, $\Delta T_{max} = 15$ K.

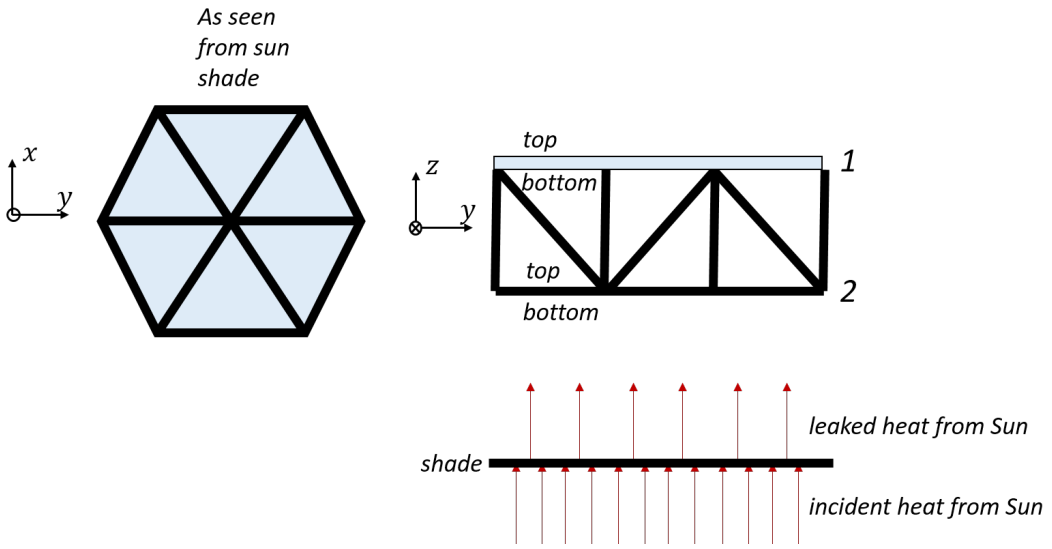

Figure 2.16: Thermal model of one module of the primary mirror. Surface 1 is the mirror surface and surface 2 is the bottom of the truss backplane.

The temperature gradient was estimated using an energy balance approach on a simple thermal model. Figure 2.16 shows one module of the model, where surface 1 is the mirror surface and surface 2 is the bottom surface of the truss backplane, consisting of a triangular tessellation of members with large gaps in between them. At L2, surface 1 is assumed to always face empty space, while surface 2 faces the sun shade. Surface 2 receives heat from the Sun that leaks through the shade, while surface 1 receives heat from the Sun that both leaks through the sun shade and through the gaps in surface 2. Both surfaces are assumed to exchange heat through

radiation and conduction. The energy balance equations for surface 1 and surface 2 are as follows:

$$\dot{Q}_{1,ss} - \dot{Q}_{cond,1\to2} - \dot{Q}_{rad,1\to2} - \dot{Q}_{1,out} = 0\,, \tag{2.4}$$

$$\dot{Q}_{2,ss} + \dot{Q}_{cond,1\to2} + \dot{Q}_{rad,1\to2} - \dot{Q}_{2,out} = 0\,. \tag{2.5}$$

Table 2.2 defines each of the parameters in Equations 2.4 and 2.5.

$\dot{Q}_{1,ss}$	Solar heat leaking through the shade and incident upon surface 1
$\dot{Q}_{2,ss}$	Solar heat leaking through the shade and incident upon surface 2
$\dot{Q}_{cond,1\to2}$	Heat conducted from surface 1 to surface 2
$\dot{Q}_{rad,1\to2}$	Heat radiated from surface 1 to surface 2
$\dot{Q}_{1,out}$	Heat radiating from surface 1 to space
$\dot{Q}_{2,out}$	Heat radiating from surface 2 to space

Table 2.2: Explanation of terms in Equations 2.4 and 2.5.

Each surface i has area A_i, with top and bottom emissivity and absorptivity of $\varepsilon_{i,top}$, $\varepsilon_{i,bottom}$, $a_{i,top}$, and $a_{i,bottom}$ respectively. The total area of the mirror surface A_1 is equal to the total number of modules $n_{m,tot}$ multiplied by the number of mirror segments per module $n_{s,m}$ and the area of one hexagonal mirror segment with side length l_S. Note that $n_{m,tot} = 3n_m^2 - 3n_m + 1$, where n_m is the number of modules along one side of the PM. The area of surface 2 is only the projected area of the truss members arranged in the triangular pattern shown left in Figure 2.16. Each module has 12 surface members with outer diameter d_o and length L. A_1 and A_2 are given by

$$A_1 = n_{m,tot} n_{s,m} \frac{3\sqrt{3}}{2} l_s^2\,, \tag{2.6}$$

$$A_2 = n_{m,tot}(12 d_o L)\,. \tag{2.7}$$

Given this geometry, the external heat fluxes are

$$\dot{Q}_{1,ss} = (1-\gamma)\dot{q}_{solar}(A_1 - A_2)a_{1,bottom}\,, \tag{2.8}$$

$$\dot{Q}_{2,ss} = (1-\gamma)\dot{q}_{solar} A_2 a_{2,bottom}\,, \tag{2.9}$$

$$\dot{Q}_{1,out} = \sigma A_1(\varepsilon_{1,top} + \varepsilon_{1,bottom})T_1^4\,, \tag{2.10}$$

$$\dot{Q}_{2,out} = \sigma A_2(\varepsilon_{2,top} + \varepsilon_{2,bottom})T_2^4\,, \tag{2.11}$$

where $\dot{q}_{solar}$ is the heat flux from the Sun, γ is the fraction of solar heat not blocked by the shade, σ is the Stefan-Boltzmann constant, and T_1 and T_2 are the temperatures of surface 1 and surface 2 respectively.

Conduction between the surfaces is carried through the seven verticals of length H and eight diagonals of length $\sqrt{L^2 + H^2}$ in each module. Given the truss material conductivity k_m, member outer diameter d_o, and inner diameter $d_i = d_o - 2t$, the total conduction term is given by

$$\dot{Q}_{cond,1\to2} = n_{m,tot} k_m \frac{\pi}{4}(d_o^2 - d_i^2)(T_1 - T_2)\left(\frac{7}{H} + \frac{8}{\sqrt{L^2 + H^2}}\right). \tag{2.12}$$

The last term to define is the radiation between the two surfaces. Surface 2 can be treated as three arrays of parallel cylinders separated by $s = \sqrt{3}/2L$. The arrays are oriented at 30° angles to each other to comprise the full triangular grid. It is assumed that the surfaces are large enough with respect to the individual cylinders to be treated as infinite. From Reference [57], the view factor from an infinite plate to an infinite array of parallel cylinders is given by

$$F_{1\to2} = 1 - \left(1 - \left(\frac{d_o}{s}\right)^2\right)^{1/2} + \frac{d_o}{s}\tan^{-1}\sqrt{\frac{s^2 - d_o^2}{d_o^2}}. \tag{2.13}$$

The total projected area of each array is $4n_{m,tot}d_oL$, because each module has four members of length L in each direction. The total radiation heat transfer from surface 1 to the three arrays in surface 2 is then given by:

$$\dot{Q}_{rad,1\to2} = \frac{3\sigma(T_1^4 - T_2^4)}{\frac{1-\varepsilon_{2,top}}{4n_{m,tot}d_oL\varepsilon_{2,top}} + \frac{1}{A_1F_{1\to2}} + \frac{1-\varepsilon_{1,bottom}}{A_1\varepsilon_{1,bottom}}}. \tag{2.14}$$

Substituting Equations 2.6 through 2.14 into Equations 2.4 and 2.5 yields the full energy balance for the system, which can be solved to obtain T_1 and T_2. The temperature difference $T_1 - T_2$ can then be compared to that in Equation 2.3 to ensure requirements are met. A quick inspection (particularly noting that $A_1 \propto n_{m,tot}$ in the radiation term) will prove that $n_{m,tot}$ appears in every term in the energy balance and thus can be canceled, meaning that the temperature difference between the surfaces is independent of aperture diameter. This is expected, because boundary effects are assumed to be negligible. Given the point design described in this section and the thermal properties in Table 2.3, $T_1 = 273$ K and $T_2 = 267$ K, satisfying both the bulk temperature requirement of 270 ± 15 K and the temperature gradient requirement of 15 K derived from Equation 2.3. The table shows that the underside of the mirror surface should be coated with colored paint (e.g. red or green), and that the sun shade should only block 36% of solar radiation. The material and thickness of the sun shade should be chosen accordingly.

Property	Value	Description
$\varepsilon_{1,top}$	0.3	polished aluminum
$\varepsilon_{1,bottom}$	0.87	colored paint
$\varepsilon_{2,top}$	0.88	matte black CFC
$\varepsilon_{2,bottom}$	0.88	matte black CFC
$a_{1,top}$	0.02	polished aluminum
$a_{1,bottom}$	0.6	colored paint
$a_{2,top}$	0.96	matte black CFC
$a_{2,bottom}$	0.96	matte black CFC
γ	0.36	

Table 2.3: Thermal surface properties of primary mirror and sun shade.

2.5.2 Dynamic Disturbances

The fundamental frequency is perhaps the most important factor controlling the response of the PM backplane structure to external loads. There is a sizable body of literature delineating methods for estimating the minimum fundamental frequency required to reject disturbances given a maximum allowable deformation. With these methods, the precision requirement of 1 μm under dynamic loads can be translated into a fundamental frequency requirement on the truss backplane structure, a parameter that is generally simple to compute.

One of the major sources of vibrations are reaction wheels. From Reference [47], the requirement on the fundamental frequency to reject reaction wheel disturbances is given by

$$f_0 = \begin{cases} f_c\sqrt{v_c - 1} & : v_c \geq 1 \\ f_c & : v_c < 1 \end{cases} \qquad (2.15)$$
$$v_c = \frac{n_{RWA}U_s}{2\zeta M_{total}\delta_{max}},$$

where f_0 is the backplane fundamental frequency, f_c is the cut-off frequency of the isolation system, n_{RWA} is the number of reaction wheels, U_s is the static reaction wheel imbalance, ζ is the damping coefficient, M_{total} is the total mass of the telescope and spacecraft, and δ_{max} is the maximum allowable deformation. In the present case, $\delta_{max} = 1\mu$m, and the damping coefficient is conservatively estimated as 0.005. Reference [47] states that a typical value for U_s is 5×10^{-6} kg·m. Thus, $v_c = 500 n_{RWA}/M_{total}$, which is less than 2 given the large mass of the PM. The fundamental frequency of the structure then only needs to exceed the isolation cut-off frequency in order to maintain precision under reaction wheel imbalance loads. Isolation systems can achieve cut-off frequencies on the order of 0.1 Hz [37].

There are many other possible sources of vibrations on the spacecraft, such as the

mirror actuators and joint settling. Control moment gyros may also be used instead of reaction wheels, which will have different vibration characteristics. Rather than addressing each source individually, it is practical to assume a spectrum of random vibrations. The minimum fundamental frequency to reject random disturbances is given by

$$f_0 > \frac{1}{2\pi}\left(\frac{G_0}{8\zeta\delta_{max}^2}\right)^{1/3}, \tag{2.16}$$

where G_0 is the RMS amplitude of the disturbance power spectral density over the bandwidth of their frequencies [37]. Assuming a 1μg amplitude and a 0-100 Hz bandwidth, $G_0 = (9.8 \times 10^{-6}\ \text{m/s}^2)^2)/(100\ \text{Hz}) = 9.6 \times 10^{-13}\ \text{m}^2/\text{s}^3$, which yields a minimum fundamental frequency of the telescope of 0.459 Hz.

Finally, one functional requirement is that the telescope shall be usable no more than three minutes after a slew maneuver. The exact response of the structure to a slew maneuver depends on the torque profile, the propulsion system, and other parameters not specified at this design stage. However, the settling time T_s required for structural distortions to fall below 2% of the initial distortion amplitude can be estimated by considering a single-degree-of-freedom system: $T_s = 3.9/\zeta\omega_0$, where $\omega_0 = 2\pi f_0$. Again assuming $\zeta = 0.005$ and requiring that $T_s < 3$ minutes implies that the fundamental frequency must be larger than 0.69 Hz, which is the most stringent dynamic requirement.

To estimate the vibration response of large truss structures, it is often assumed that the members are pin-jointed at both ends and can only carry axial loads, and the member center lines coming into a joint all meet at a single point. With these assumptions, obtaining the stiffness matrix $\mathbf{K}$ and mass matrix $\mathbf{M}$ is relatively straightforward using the direct stiffness method for truss analysis. The fundamental frequency is then the inverse of the smallest eigenvalue of $\mathbf{M}^{-1}\mathbf{K}$. Furthermore, if the depth of the truss is less than 20% of the span, the structure can be treated as a flat plate with equivalent areal density, and thus the fundamental frequency can be easily obtained from plate theory [58].

In the ISTAR architecture, the variable gaps between the modules necessarily create eccentricities, violating the first assumption that center lines meet at a point. One might immediately conclude that such a design would result in a significant loss in structural integrity. However, the actual members are not simple truss elements, but beams capable of carrying bending loads and rigidly fixed to each other at the joints. Thus, the actual affect of the gaps was investigated before conclusions were

drawn. Three finite element models were constructed, as sketched in Figure 2.17. In the first model, the members were pin-jointed truss elements. A module with side length equivalent to the design side length plus half the nominal gap size (2.81 m) was tessellated to form an initially flat backplane. The nodes at the connection points were merged, yielding two coincident vertical members from the two adjacent modules. The curvature was approximated by projecting the top surface nodes onto a sphere of radius R_{pm} and the bottom surface nodes onto a sphere of radius $R_{pm}+H$. A lumped mass was applied to each of the nodes on the top surface, to represent the mirror module areal density of 25 kg/m^2. The second model was the same as the first model, except each member was a beam (capable of carrying bending loads) with 10 elements along the length. Only the nodes at the endpoints of the members were projected to create the curvature, so that the members remained straight. The third model was the same as the second model, except the modules had the design side length, so that the nominal gaps were present. The connections between modules were created with rigid beam elements.

The design member cross-section and module depth were applied to the three models. For the first model, the frequencies of the first ten modes were computed as a function of D_{pm} using the direct stiffness method. For the second and third models, the frequencies were computed using the finite element software package Abaqus [48]. The variation of the fundamental frequency f_0 with D_{pm} is given in Table 2.4 for the three models. Figure 2.18 plots the frequencies of the first ten modes for the three models with D_{pm} = 105.3 m. As expected, the first and second models yielded extremely close results, indicating that the simple truss structure was a good approximation of the equivalent beam structure. The presence of gaps did result in about a 20% decrease in fundamental frequency. However, even for D_{pm} = 105.3 m, the f_0 value of 0.81 Hz still meets the minimum requirement of 0.69 Hz with a 17% margin of error. Even if the connections are not rigid, but instead aluminum rectangular beams with 2 cm by 2 cm cross-section, the fundamental frequency is only reduced to 0.76 Hz for the largest value of D_{pm} and the requirement is still met.

Finally, one general design rule is that the member slenderness ratio, or the ratio of the length to the radius of gyration, should be above 200 so that the elastic modulus, rather than the compression strength, dominates behavior. However, the fundamental frequency of each individual member should be at least three times that of the full structure, effectively placing an upper bound on the slenderness

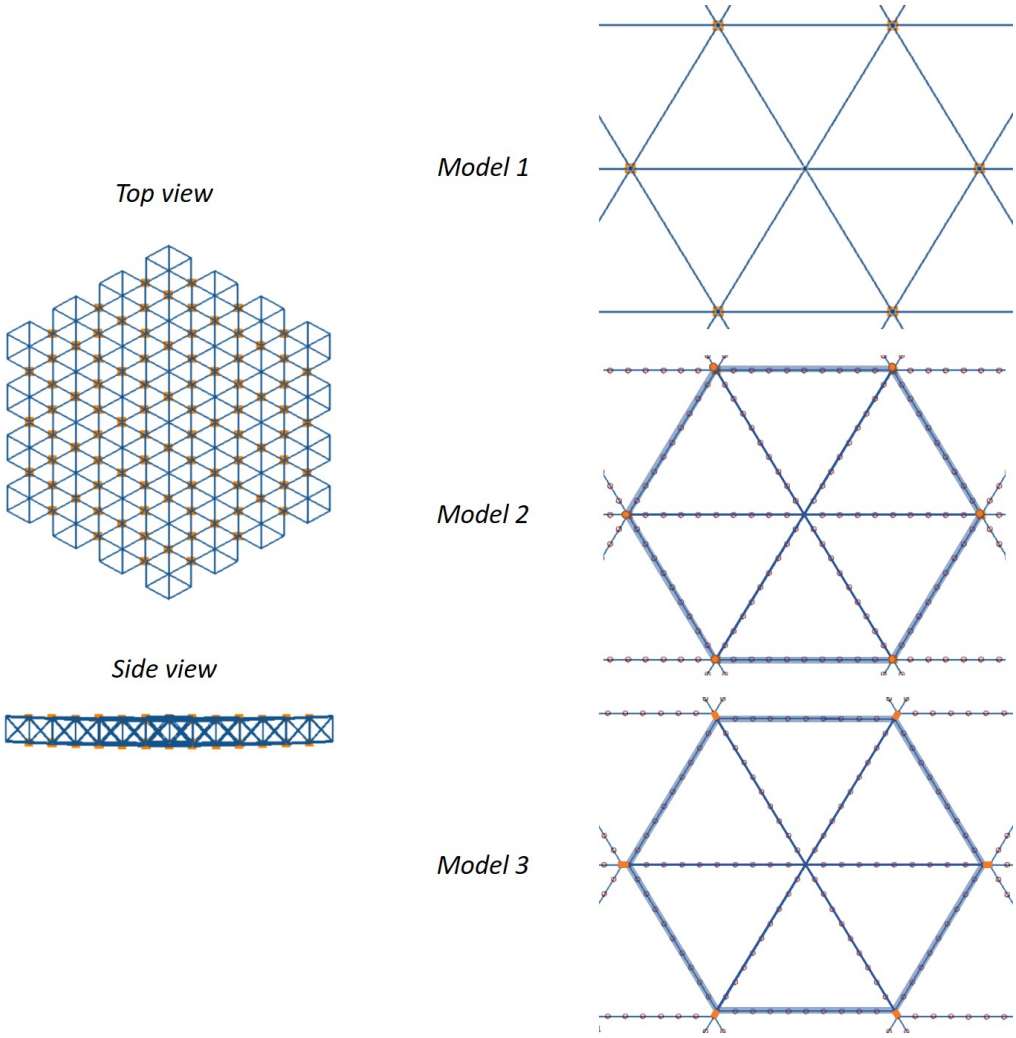

Figure 2.17: Three different models with varying levels of fidelity used to estimate the fundamental frequency of the PM backplane. On the left, a global top view and side view of the backplane (for $n_m = 4$) is shown. The spherical curvature is evident in the side view. The differences between the three models are not visible at this scale. On the right, the backplane is enlarged to show the detail of one module for each of the models. In the first model, each module has a side length of 2.81 m. The members are 2-node truss elements. There are no gaps between the modules, and thus the connecting nodes are coincident. The connections are created by merging these nodes. In the second model, the module side length is again 2.81 m. The members are divided into many beam elements, with nodes as shown. As in the first model, there are no gaps between the modules, and the connections are created by merging the coincident nodes. In the third model, the module side length is the design value of 2.76 m, yielding approximately 10 mm gaps between the modules. The connections between modules are made with rigid beams.

[45]. The resulting constraints on the member outer diameter d_o and inner diameter

n_m	$D_{pm}[m]$	Model 1 f_0 [Hz]	Model 2 f_0 [Hz]	Model 3 f_0 [Hz]
3	27.9	10.59	10.60	8.81
4	38.9	6.15	6.16	5.10
5	50.0	3.97	3.97	3.29
6	61.0	2.76	2.76	2.28
7	72.1	2.02	2.02	1.67
8	83.2	1.54	1.54	1.27
9	94.3	1.21	1.21	1.00
10	105.3	0.98	0.98	0.81

Table 2.4: Variation of fundamental frequency with aperture diameter for the three models.

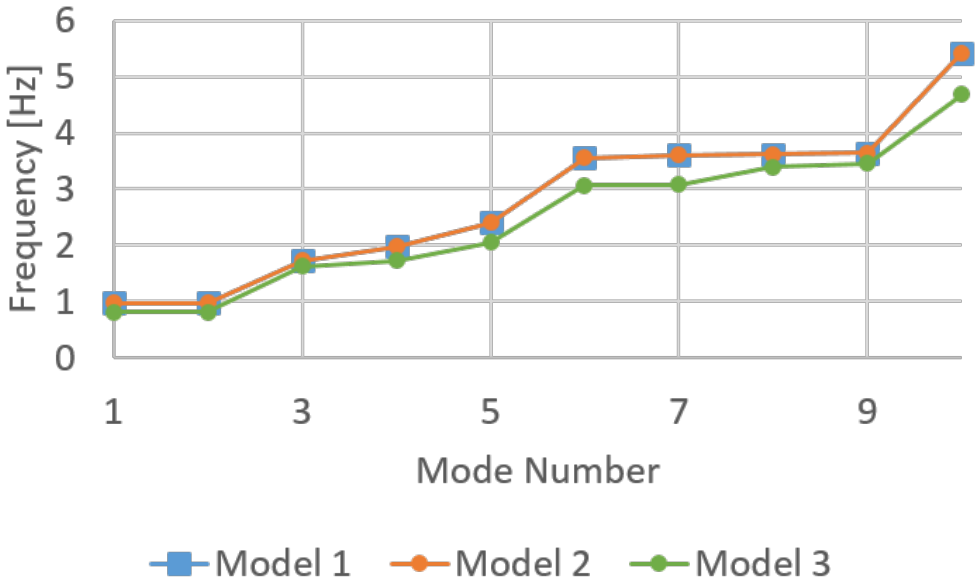

Figure 2.18: Frequencies of modes 1-10 for the three models with $n_m = 10$. Mode 1 is the fundamental mode with frequency f_0.

$d_i = d_o - 2t$ are

$$r_{slender} = \frac{4L}{\sqrt{d_o^2 + d_i^2}} > 200,$$

$$f_{0,member} = \frac{1}{2\pi}\frac{22.373}{L_{member}^2}\sqrt{\frac{E\pi(d_o^4 - d_i^4)/64}{\rho}} > 3f_{0,structure}\,.$$

For the properties of M55J CFC (E = 340 GPa and ρ = 1620 kg/m^3), the design dimensions of d_o = 35 mm and t = 3 mm yield a slenderness ratio of 343 and a member fundamental frequency of 38 Hz, which satisfies the requirements for all D_{pm}.

2.6 Chapter Conclusions

This chapter outlined an architecture for a robotically-assembled telescope with an aperture diameter between approximately 20 m and 100 m. The concept breaks the cost curve by utilizing an optical design with a spherical primary mirror, allowing each of the segments to be identical for a high degree of modularity. The assembly process of the primary mirror efficiently balances deployable structures with robotic operations. The primary mirror is broken down into groups of mirror segments called mirror modules, backed by separate deployable truss modules. The truss modules provide stiffness and support to the mirror surface. Structural and thermal analyses have been performed to design the basic dimensions of the truss module and demonstrate that it can provide precision levels within the range of the wavefront correction system to yield diffraction-limited images. Some important parameters of the telescope are summarized by Table 2.5.

For any D_{pm}	
Mirror segment vertex-to-vertex length	1.35 m
Number of segments in mirror module ($n_{s,m}$)	19
Mirror module vertex-to-vertex length	6.28 m
Truss module vertex-to-vertex length ($2L$)	5.52 m
Truss module depth (H)	2.76 m
Truss module member outer diameter (d_o)	35 mm
Truss module member wall thickness (t)	3 mm
Truss material	M55J CFC
Truss areal density	3 kg/m^2
Total PM areal density (without connectors and hinges)	28 kg/m^2
Sun shade blockage factor (γ)	0.36
Operating temperature	240-300 K
Mirror module underside coating	Colored paint
Focal ratio	4
For D_{pm} = 105 m	
Radius of curvature (R_{pm})	840 m
Secondary clamshell mirror diameter	8.6 m
Secondary clamshell mirror separation	24.4 m
Sun shade mast length	75 m
Total mass of PM backing structure	19,000 kg (21 tons)
Total mass of PM	183,000 kg (202 tons)

Table 2.5: Key design parameters of the ISTAR telescope concept.

As previously mentioned, some of the work in this chapter has been adapted from a paper with many co-authors. Backes, Burdick, and Pellegrino proposed the

study. The optical scheme was designed by Wu. The mirror module design and gap analysis were performed by Lee. Backes, Mukherjee, and Kim were responsible for the robotic operations and design. The truss module design and analysis were performed by Hogstrom. Hogstrom was also the primary author of the paper.

Chapter 3

THE RELIABILITY ESTIMATION TOOLKIT

As described in the introduction, the deployment reliability in the presence of fabrication errors is an important parameter that must be quantified to establish the feasibility of the ISTAR mission. In this context, the reliability is defined as the percentage of modules, each with a unique set of errors, that deploy completely without any kind of failure. Failure criteria may include any hinges not latching, any nodes largely out of place, or any reaction forces higher than a tolerable level. A comprehensive deployment reliability estimation toolkit has been developed using a combination of Abaqus Standard and Abaqus's native Python build [48]. The toolkit performs the following levels of analysis:

1. Create a detailed simulation model of a module and accurately reproduce the deployment behavior.
2. For a model with a certain nominal geometry, repeatedly apply a unique set of random errors, chosen from a distribution with given bounds, and repeat step 1. Categorize each deployment as a success or failure and return the estimated reliability for that model.
3. Repeatedly alter the model and repeat step 2, establishing the effect of the model change on reliability.

Thus, the toolkit is capable of rapidly producing reliability trade studies to aid in optimizing the module design. While it was developed in the context of the ISTAR truss module, the toolkit is general to any geometry and deployment scheme. This chapter discusses the models and methods of the toolkit in detail. In the first section, the simulation model is defined, using a simplified version of the PACTRUSS as an example. The second section outlines the method for simulating the deployment of a general model. Finally, the third section outlines the method for performing many simulations to obtain reliability estimates and trade studies.

Some of the content in this chapter has been adapted from: Kristina Hogstrom et al. "Methods for Characterizing and Increasing the Reliability of Deployable Mod-

ules for Large Optical Reflectors." In: 3rd AIAA Spacecraft Structures Conference, AIAA Science and Technology Forum and Exposition. 2016.

3.1 Simulation Model

The full hexagonal PACTRUSS module can be divided into six identical triangular prisms, or wedges, tessellated as shown in Figure 3.1. The figure explains that wedges with dashed outlines are mirrored with respect to the horizontal plane, with the diagonal members adjusted so that the unfolding behavior is consistent. The wedge provides a representative but simpler example for the development and description of the toolkit compared to the full module. The wedge can also be easily deployed by simply moving the two verticals attached to the unbraced face apart, an important feature for the experimental validation discussed in Chapter 4. In this section, the components of the simulation model are presented using the wedge as an example. However, a model of any geometry can be constructed from the same components.

3.1.1 Overall Geometry and Truss Members

A sketch of the wedge in both the unfolded and folded positions is given in Figure 3.2. The key overall dimensions are L, the side length of the module when deployed, q, the side length of the module when stowed, and H, the depth. Figure 3.3 is a more detailed depiction of the two unique faces in the wedge. Offsets in the joints are necessary to allow each of the members to be vertical in the stowed position. Choosing the offset variable l_j shown in the figure is sufficient to uniquely determine the offsets at every location in the structure. The magnitude of l_j must be at least equal to the outer diameter of the members, in order to ensure that they do not interfere when folded. The design of the Rolamite hinge determines the distance μ between the centerlines of the attached members when folded. Like l_j, the magnitude of μ must be at least equal to the outer diameter of the members.

Figure 3.4 shows a more detailed simulation model of the wedge, with node markers and element labels. Each member is composed of beam elements (B31) with pipe cross-section defined by the outer diameter d_o, and the wall thickness t. The member material is treated as isotropic and linearly elastic, with elastic modulus E_m, Poisson's ratio ν_m, and density ρ_m. Beam elements were chosen over truss elements to increase fidelity substantially by including bending stiffness. The model with the highest fidelity would exactly replicate the member geometry with shell or solid elements. However, beam elements can accurately approximate

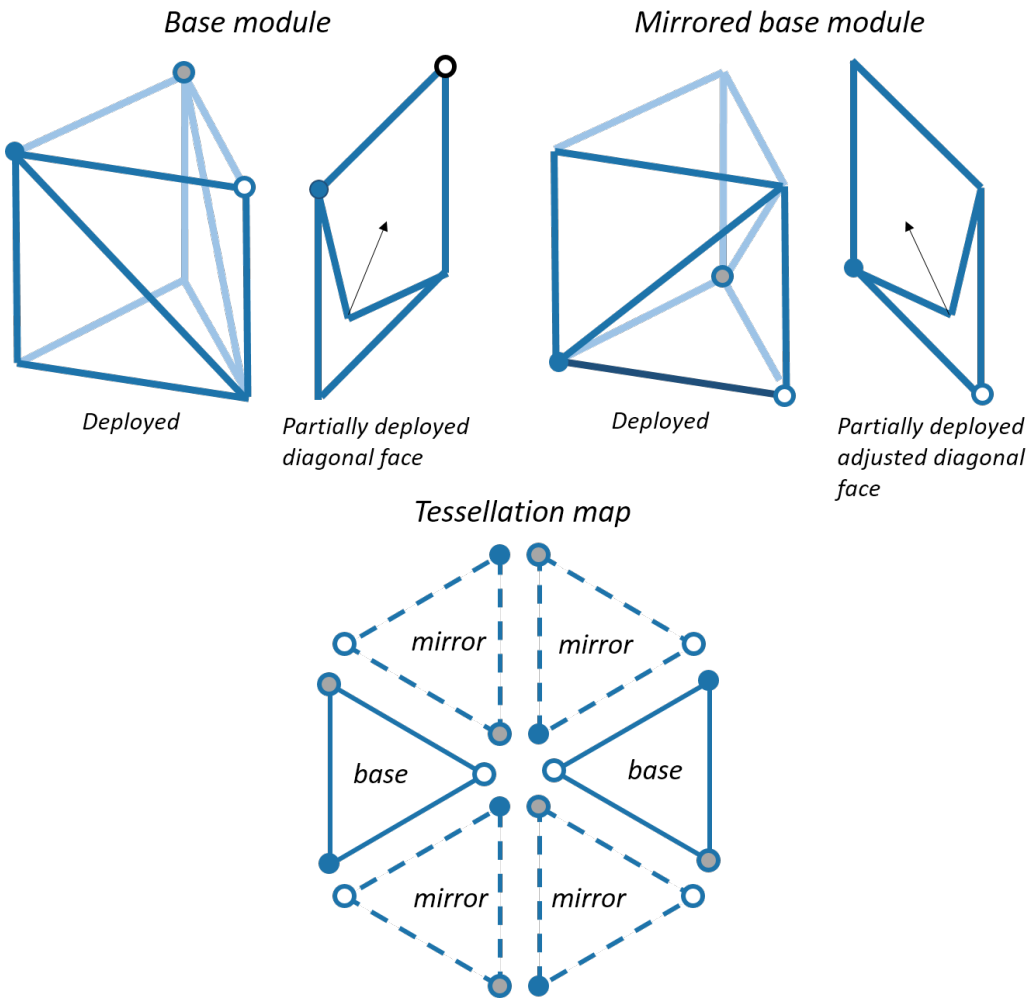

Figure 3.1: (Upper left) The base wedge that comprises the full hexagonal module is shown in the deployed configuration. One diagonal face of the wedge is shown partially deployed to illustrate how the diagonals unfold upward. (Upper right) This sketch shows the base module mirrored about the horizontal plane. If the diagonals were also mirrored, their fold direction would be downward. To be consistent with the base module, the diagonals have been adjusted to also fold upward. (Bottom) This image shows how the base module and the mirrored base module are tessellated to recreate the full hexagonal module. The colored circles indicate how the modules are rotated.

this geometry while reducing the total number of required elements by orders of magnitude. This in turn drastically reduces simulation complexity and run-time without significant losses in accuracy, making beam elements the most practical choice.

All connections between members are modeled with connector elements (CONN3D2). The basic function of these elements is to impose kinematic constraints between

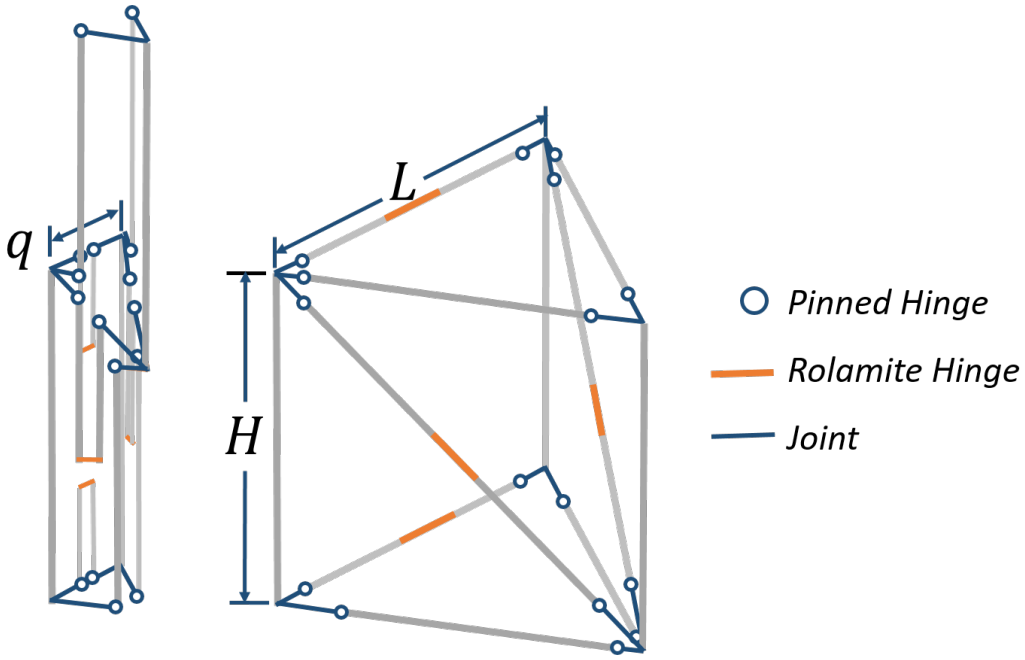

Figure 3.2: Sketch of the wedge model in the stowed (left) and deployed (right) positions.

two nodes, coupling displacement, velocity, or acceleration in any degree of freedom. However, these elements can also include complex behavior, such as elasticity, damping, and friction. The connectors in this model typically behave as nonlinear elastic hinges. To define this type of connector, the following information must be provided:

- the indices of the two nodes to be connected,
- the local coordinate system of the connector with respect to the global coordinate system,
- and the moment-rotation profile or the stiffness of the connector.

Generally, bulk rotation occurs about the x axis of the local coordinate system. The specific behavior of each connector is described more thoroughly in the following sections.

3.1.2 Joints and Pinned Hinges

In general, joints connect the vertical members to longerons and diagonals. Each joint is modeled as a single 2-node beam element. As shown in Figure 3.5, node 1 of the joint is shared with the appropriate end of the vertical member, providing a

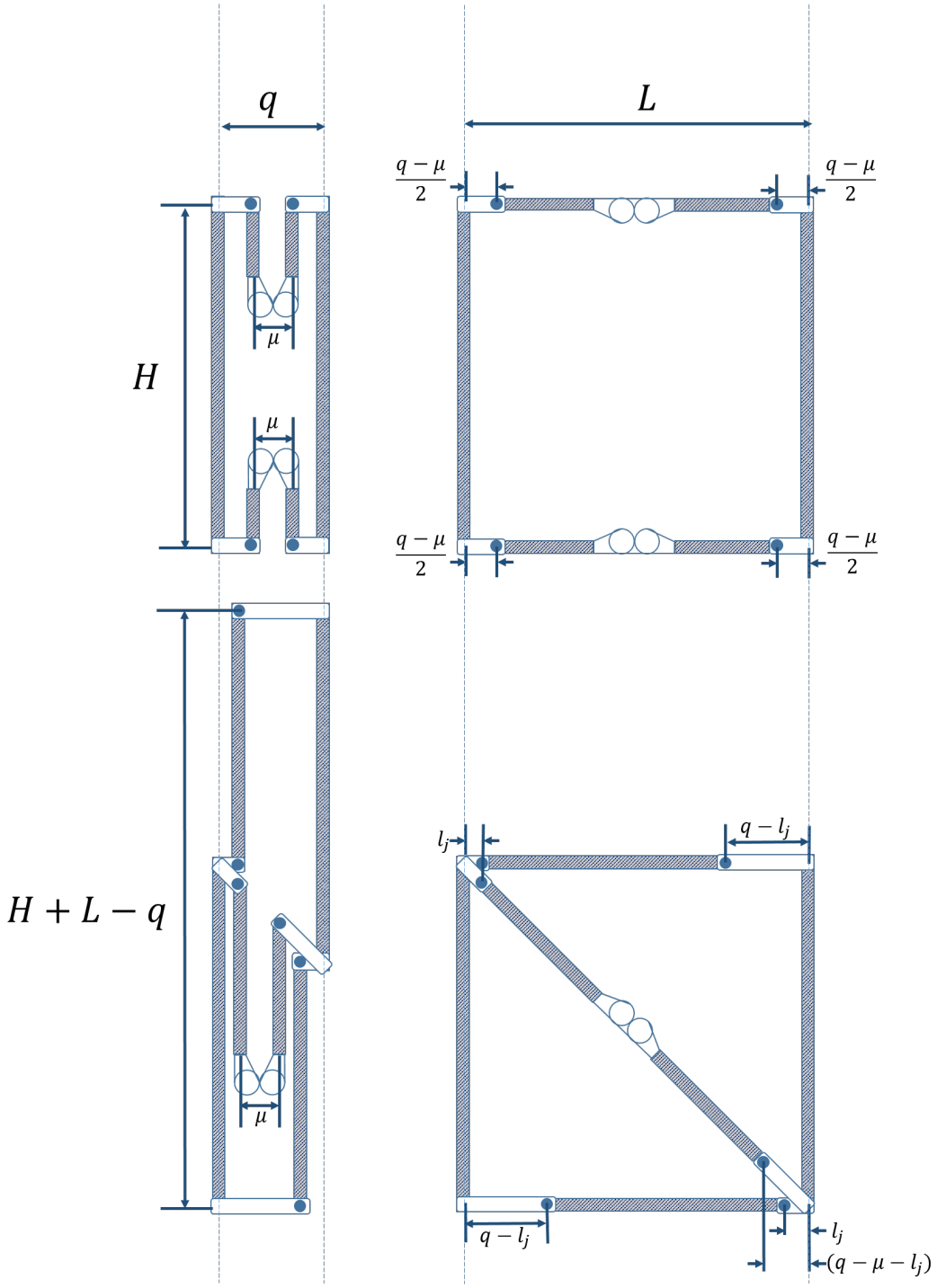

Figure 3.3: Detailed drawing of the two unique faces in the wedge model: the folding longeron face (top) and the diagonal face (bottom). The wedge has two diagonal faces and one folding longeron face. All dimensions required to uniquely define the model are shown.

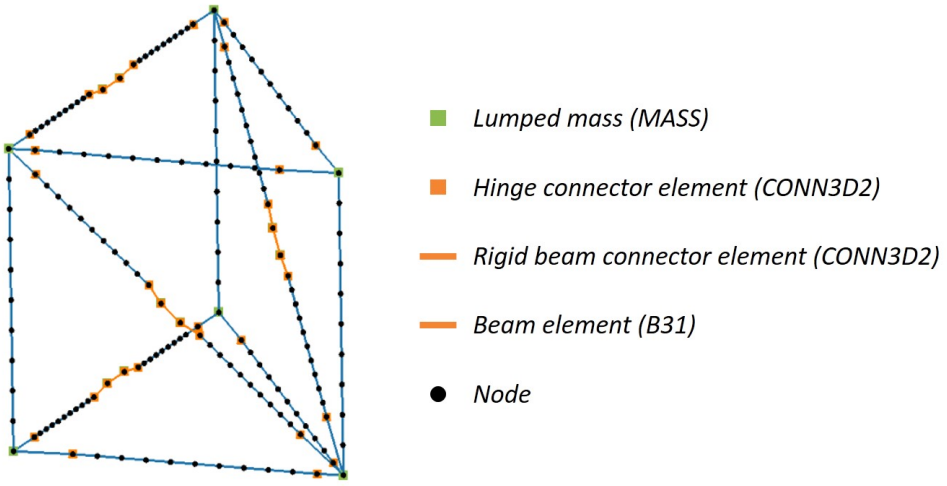

Figure 3.4: Simulation model of the wedge with node markers and element labels.

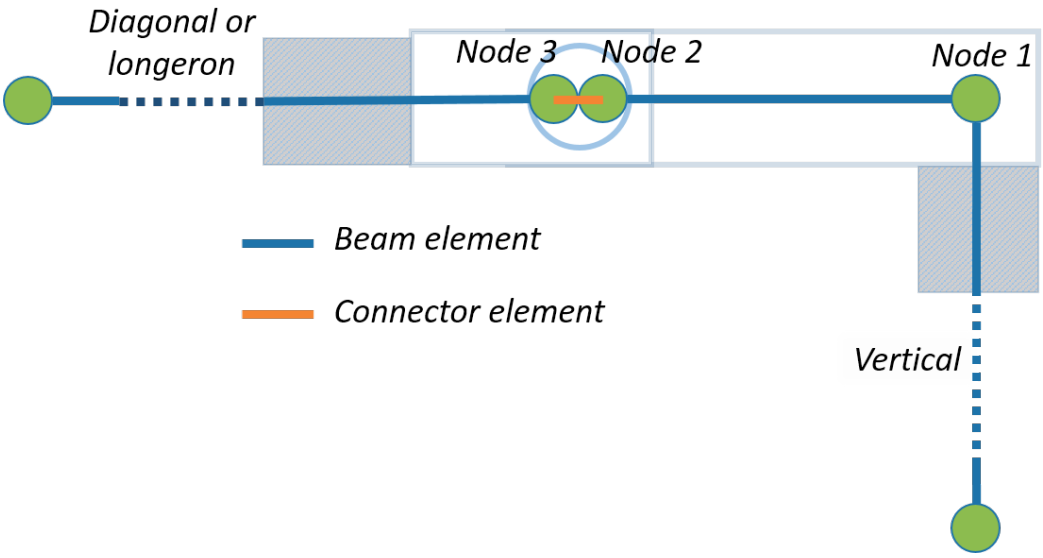

Figure 3.5: Model of a joint connecting a vertical member to a diagonal or longeron member. Node 1 is located at the end of the vertical member and node 3 is located at the end of the other member. Though shown with an offset for graphical purposes, node 2 is coincident with node 3. A beam element connects nodes 1 and 2, and a connector element with hinge-like properties connects nodes 2 and 3.

fixed connection. Node 2 is coincident with but unique to the node at the end of the other member, node 3. A connector element links nodes 2 and 3. The connector is effectively a pinned hinge, providing free rotation about the local x axis in the deployment direction. However, the pinned hinges in this model have a "soft stop" that mitigates rotation in the opposite direction by applying a high moment when the rotation angle has reached a certain critical overextension θ_{stop}. The behavior

is illustrated in Figure 3.6*b* and *f*. The pinned hinges can also have translational compliance and slack, the combined effect of which is modeled by applying non-linear elastic behavior in each of the translational directions. When the displacement of node 3 with respect to node 2 is small, the connector behaves like a spring with low stiffness, allowing node 3 to move somewhat freely. When the displacement reaches a certain threshold δ_{stop}, the stiffness becomes high, providing a restoring force that pushes node 3 back toward node 2. The behavior is illustrated in Figure 3.6b-e.

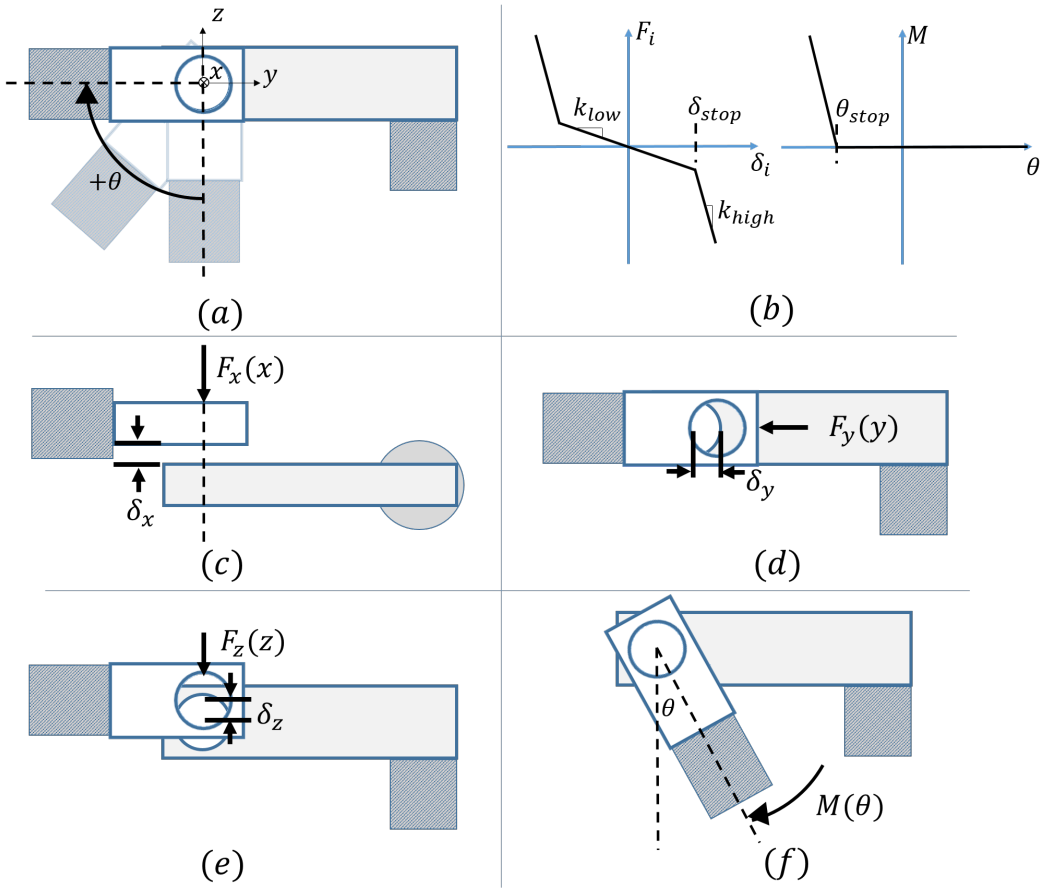

Figure 3.6: Illustration of the behavior of a pinned hinge that connects a joint to a diagonal or longeron member. In (*a*), the coordinate system of the pinned hinge is defined, showing how rotation occurs about the x axis. In this case, the nominal direction of rotation for the hinge is clockwise. In (*c*)-(*e*), the connection points of the hinge undergo some relative displacement δ_i in the direction i. The restoring force $F_i(\delta_i)$ is shown, where $F_i(\delta_i)$ is defined in (*b*). In (*f*), the hinge rotates counter-clockwise, opposite of its nominal rotation direction. The restoring moment $M(\theta)$ is shown, where $M(\theta)$ is defined in (*b*).

The joint beam element has a rectangular cross-section, with width and height

a_j and b_j respectively. The joint material is treated as isotropic and linearly elastic, with elastic modulus E_j and Poisson's ratio ν_j. The density ρ_j of the joint can also be applied to the beam element. However, since realistic joints may have substantial parasitic mass beyond the beams that connect the members, ρ_j can be set to 0 and the exact mass of the joint modeled as a lumped mass located at node 1.

3.1.3 Rolamite Hinges

As previously discussed in Section 2.5, a Rolamite tape spring hinge consists of a pair of steel measuring tape sections and two sets of circular cams that are constrained to roll on each other, allowing only one rotational degree of freedom. The cam sets are held together with a pretensioned wire. The tape sections have a circular arc cross-section and are attached to the cam sets by end clamps. These clamps are designed to match the curvatures of the upper and lower tape surfaces. The hinges can fold compactly and then snap into a stiff configuration upon unfolding. Figure 3.7 shows the key dimensions of the tape sections and Rolamite hinge design. A verbal description of each variable in Figure 3.7 and other key variables not shown are given in Table 3.1.

t_t	Thickness of tape spring
α	Opening angle of the tape spring arc
r_t	Radius of curvature of the tape spring
e_t	Distance between the centroid of the tape spring arc and the centroid of the upper clamp arc
L_{rol}	Distance between member attachment points, or total length of Rolamite hinge
L_t	Unclamped length of tape spring
h_t	Maximum distance between the two tape springs
d_t	Distance between the centerline of the cams and the centerline between the tape springs
p	Distance between the cam centers, or twice the cam radius of curvature
E_t	Elastic modulus of the tape spring material
I_t	Area moment of inertia of the tape spring cross-section
A_t	Cross-sectional area of the tape spring

Table 3.1: Explanation of tape spring and Rolamite variables.

The approximate moment-rotation profile of a Rolamite hinge is shown in Figure 3.8. It is divided into two regions: deployment and latching. The rotation angle θ is defined to be 0 when the hinge is completely folded and π when it is completely unfolded. As the hinge unfolds and θ increases, the moment follows the curve defined by the deployment region. When the critical angle θ_c is reached, where θ_c is

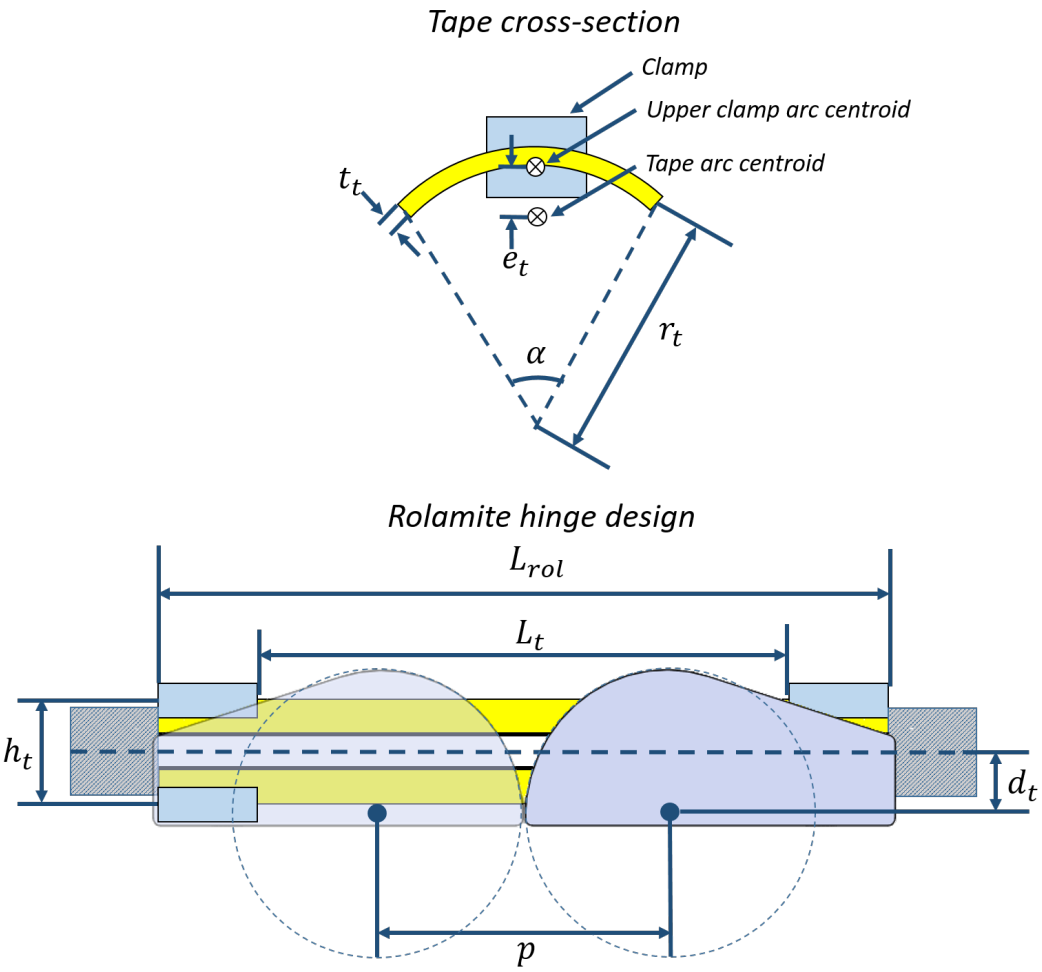

Figure 3.7: Dimensions of tape spring cross-section and Rolamite hinge.

a close to π, the moment jumps to a much higher value (~1-2 orders of magnitude) then decreases along a line to zero when $\theta = \pi$ radians. Kinetic energy may rotate the hinge beyond $\theta = \pi$, at which point the moment becomes increasingly negative, driving the hinge back to the unfolded state. The hinge may continue to oscillate around $\theta = \pi$, but the moment will still follow the linear profile that defines the latching region until any remaining kinetic energy is damped [55].

The maximum latching moment and the minimum deployment moment of the Rolamite hinge can be estimated analytically using techniques developed by Watt [55]. He gives the maximum moment as

$$M_{max} = P_{cr}\left(h_t/2 + d_t + \frac{(h_t/2 - d_t)^2}{(h_t/2 + d_t)}\right),$$

where P_{cr} is the compression load in one tape section, solved iteratively from the

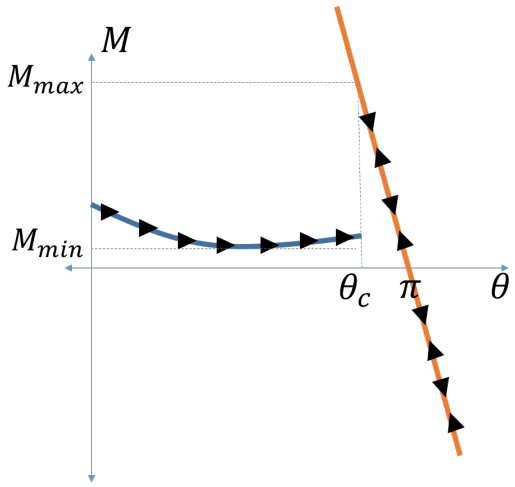

Figure 3.8: Sketch of the general moment-rotation profile of Rolamite hinges. The blue line defines the deployment curve and the orange line defines the latching curve. The hinge follows the deployment curve until the critical angle θ_c is reached. It then permanently switches to the latching curve for any rotation thereafter.

following equation:

$$\frac{0.6 t_t E_t}{r_t} = P_{cr}\left(\frac{1}{A_t} + \frac{e_t^2}{I_t cos\sqrt{\frac{P_c r L_t^2}{4 E_t I_t}}}\right).$$

Watt gives the minimum deployment moment for two tape sections as

$$M_{min} = \frac{\alpha E_t t_t^3}{6(1-\nu_t)^2}.$$

Figure 3.9 shows the kinematic model of the Rolamite hinge. Nodes a_1 and b_1 are located where the member centerlines attach to the Rolamite cam sets. Coincident nodes a_2 and a_2' are located at the center of one cam set and b_2 and b_2' are at the center of the other cam set. Two hinge connectors with the Rolamite moment-rotation profile link a_2 to a_2' and b_2 to b_2' respectively, constraining all degrees of freedom except rotation about the defined local x axis. The rotations of the connectors are defined to be equal in magnitude and opposite in sign. Rigid beams connect a_1 to a_2, a_2' to b_2', and b_2' to b_2.

The moment-rotation behavior of the hinge connectors can be described as a piecewise function based on a switch variable s_{latch}, such that the deployment portion of the profile is followed when s_{latch} is equal to 0 and the latching portion is followed when s_{latch} is equal to 1. The switch in s_{latch} occurs the first time

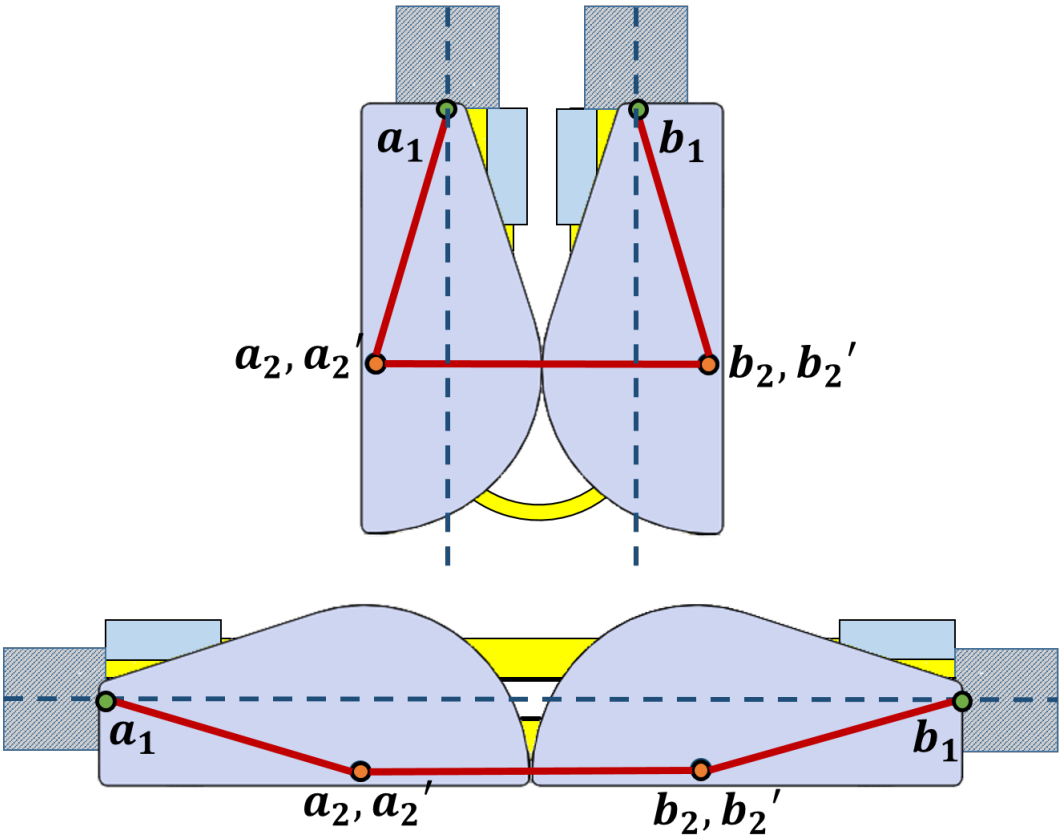

Figure 3.9: Kinematic model of Rolamite hinge. Nodes a_1 and b_1 are located at the attachment points between the members and the hinge. Nodes a_2 and a_2' are coincident and located at the circular center of one cam set. Similarly, nodes b_2 and b_2' are coincident and located at the circular center of the other cam set. Rigid beams connect a_1 to a_2, a_2' to b_2', and b_2' to b_2. Connectors with hinge-like behavior link a_2 to a_2' and b_2 to b_2'.

the rotation in the connector exceeds the critical angle θ_c and remains unchanged thereafter. This behavior is simulated in Abaqus by creating a table that defines the moment as a function of the field variable s_{latch} and the rotation angle $\theta/2$, accounting for the fact that each of the two connectors rotates half the full rotation of the Rolamite hinge. Two customized user subroutines that run in parallel to Abaqus are required to set the value of s_{latch}: URDFIL and UFIELD. At the beginning of the simulation, s_{latch} is initialized to 0. After every time increment, URDFIL extracts the rotation of each connector and feeds it to UFIELD, which determines whether $\theta > \theta_c$. Once this criterion is true, UFIELD sets s_{latch} to 1, and Abaqus is signaled to follow that section of the moment table for the remainder of the simulation.

3.1.4 Types of Errors

Three types of errors can be applied to the simulation model:

- member length errors, which can be introduced by imprecisely cutting the members,
- member alignment errors, which can be introduced by imprecisely attaching or gluing the members to the joints or if the members are not straight after manufacturing,
- and hinge axis errors, which can be introduced by misaligning the holes for the pins that create the pinned hinges or by creating some relative twist between the Rolamite cam sets with the tensioning wire.

Figure 3.10 illustrates each error type. More detail describing how these errors are applied will be given in Section 3.2.

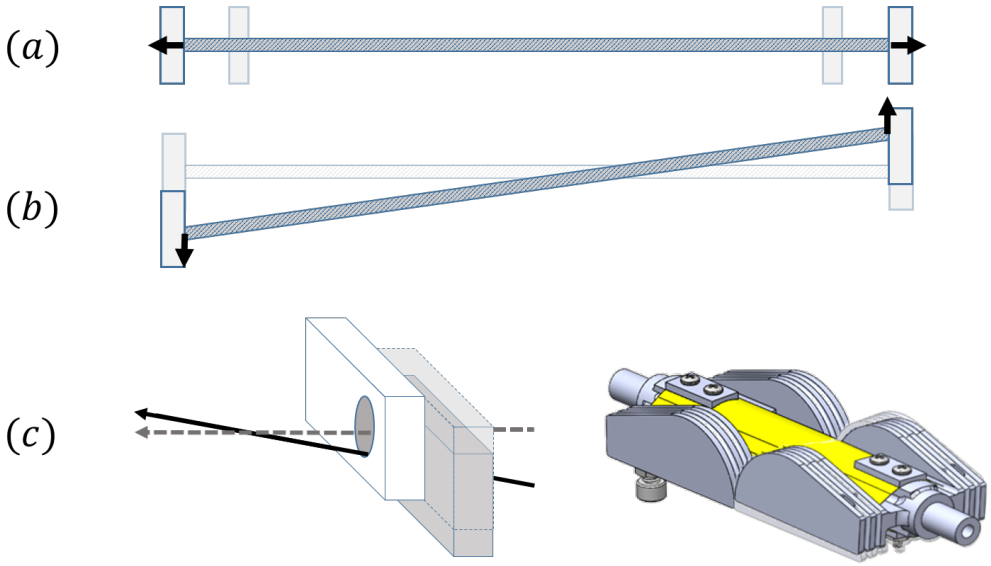

Figure 3.10: Illustration of the three different types of errors that can be introduced into the simulation model: *(a)* member length errors, *(b)* member alignment errors, and *(c)* hinge axis errors in pinned hinges (left) and Rolamite hinges (right).

3.2 Single Deployment Simulation Method

This section describes the computational methods used to simulate the deployment of a general module. The PACTRUSS module is presented as an example when necessary.

3.2.1 Constructing the Model and Applying Errors

To construct any geometric model, the toolkit requires only two sets of information. The first is a matrix providing the coordinates of the endpoints of each member *in the stowed position*. Specifically, the i^{th} row of this matrix contains the (x, y, z) coordinates of the first endpoint and the (x, y, z) of the second endpoint of member i. The second set of information needed is a matrix describing the connectivity between the members. For connection k between members i and j, the k^{th} row of the matrix has the following information:

i, endpoint 1 or 2 of i, j, endpoint 1 or 2 of j, type, orientation, direction.

The "type" flag indicates the type of connection to be made. In the PACTRUSS model, the two types are pinned hinges and Rolamite hinges. However, other types are available, such as a pinned hinge that captures the Rolamite moment-rotation profile but not the kinematics. The orientation is defined by two vectors: the first sets the x axis and the second sets the x-y plane. The direction is a flag indicating whether the hinge nominally rotates clockwise or counterclockwise about the x axis.

The connectivity matrix, endpoint matrix, and all other required input are passed to the toolkit using the model variables file. This file must contain the following information:

- Member material information (E_m, ν_m, ρ_m).
- Member cross-section dimensions (d_o, t).
- Rolamite hinge dimensions not inherently defined in the endpoints matrix (p, L_{rol}).
- Number of beam elements to create along each member.
- Joint material and properties (E_j, ν_j, ρ_j, a_j, b_j).
- Flags to include or neglect gravity or joint masses.
- Path to a file containing a table of θ and M, defining the Rolamite moment-rotation curve. The last entry in this file should define M_{max} and θ_c.
- Path to connectivity matrix.

- *(Optional)* Path to endpoints matrix. If this option is not included, then a PACTRUSS geometry is assumed and the following dimensions must be provided: L, H, q, l_j, and μ. The endpoints matrix is then generated automatically.

Errors in the model can be introduced in two ways. A known set of errors can be included directly in the endpoint and connectivity matrices. Otherwise, a maximum value for each error type can be included in the model variables file as follows:

- dL_{max}: maximum member length error
- dP_{max}: maximum member alignment error
- $d\theta_{max}$: maximum hinge axis error

In this case, the toolkit automatically applies random errors within those bounds to the appropriate locations in the geometry using the following methodology. For each member in the model, a length error dL between $-dL_{max}$ and $+dL_{max}$ is randomly selected. For member endpoints e_1 and e_2, the unit vector axis along the member is $\hat{u} = \frac{e_2 - e_1}{||e_2 - e_1||}$. To include the error, e_1 becomes $e_1 - (dL/2)\hat{u}$ and e_2 becomes $e_2 + (dL/2)\hat{u}$. This is illustrated in Figure 3.11a. Once any length error is applied, then a unit vector perpendicular to $\hat{u}$, $\hat{u_{p1}}$, and another unit vector perpendicular to both $\hat{u}$ and $\hat{u_{p1}}$, $\hat{u_{p2}}$, are computed. Each member endpoint is then translated by a random amount $dP_1 i$ within the bounds of $\pm dP_{max}$ along $\hat{u_{p1}}$ and by dP_2 along $\hat{u_{p2}}$, as shown in Figure 3.11b. Finally, for each hinge axis $\vec{h}$, a unit vector perpendicular to $\vec{h}$, $\hat{h_p}$ is computed. The vector $\vec{h'}$ is obtained, such that $\vec{h'} = \vec{h} + tan(d\theta)\hat{h_p}$, where $d\theta$ is a random angle within the bounds of $\pm d\theta_{max}$. The final misaligned hinge axis is then the vector $\vec{h'}$ rotated by ϕ about $\vec{h}$, where ϕ is a random angle between 0 and 2π. The process is illustrated in Figure 3.11c. Whether the errors are directly specified in the endpoint and connectivity matrices or applied randomly using the above process, the simulation retains no knowledge of a "nominal" configuration. The errors are simply part of the geometry definition.

From this information, the toolkit automatically creates joint beam elements, pinned hinges, and Rolamite hinges where they are located in the structure. One key result of this is that the joints are automatically sized to fit between the member endpoints that they connect, regardless of whether errors are included. In other words, there is no reference to a "nominal" joint length. This means that there are

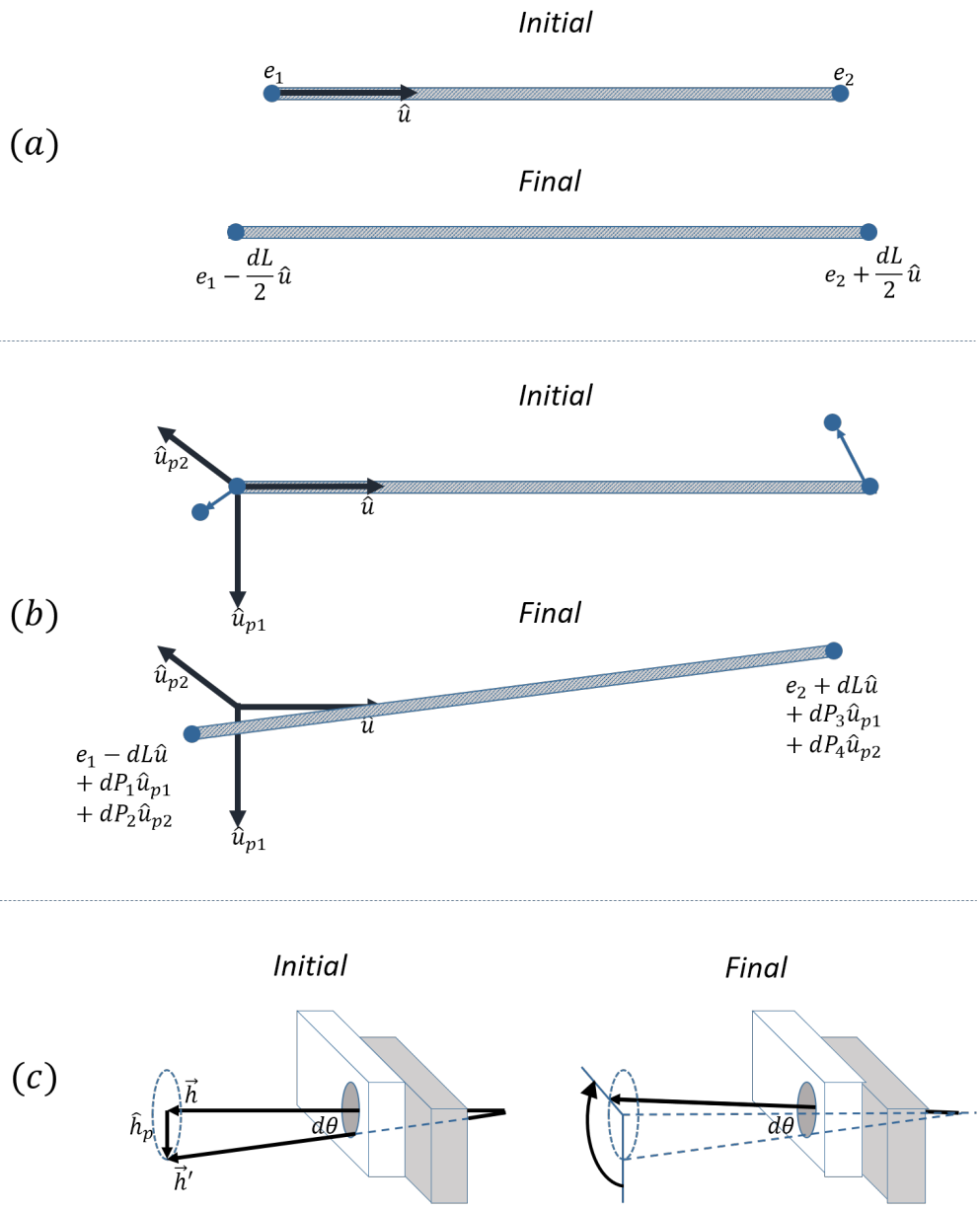

Figure 3.11: Method for applying *(a)* member length errors, *(b)* member alignment errors, and *(c)* hinge axis errors.

no conflicting dimensions to cause pre-stress. It was found that minimal force was required to construct the experimental module (discussed in Chapter 4), suggesting that stresses due to errors were negligible and can thus be reasonably ignored in the simulation model. Since the basis for this assumption is experimental observation, it may not be valid for other geometries besides the PACTRUSS.

3.2.2 Running Abaqus

At the core of the toolkit is the simulation of one deployment. This is performed using the *stabilized static* analysis procedure in Abaqus. To illustrate the effect of stabilization, consider the case of an uncontrolled deployment, or one that actuates purely by spring force. In a general static procedure, an equilibrium solution is sought after each time increment, subject to the equation

$$F_{external} - F_{internal} = 0,$$

where $F_{external}$ is the vector of external loads on the nodes and $F_{internal}$ is the vector of internal loads on the nodes. For the spring-actuated case, the only equilibrium solution is the fully deployed configuration. The nodes must undergo large displacements to reach this solution from the initial configuration, and so the solution is almost certainly outside the radius of convergence for the solver. Thus, this type of analysis is not possible with a static procedure. Now consider a controlled deployment, in which the bulk displacements in each time increment are kept small by applying a displacement boundary condition, such that the analysis steps slowly toward the solution. Ordinarily, this would be possible with a static procedure. However, large displacements may still occur, particularly due to the discontinuity in the Rolamite hinge moment-rotation profile. Thus, a purely static analysis is not recommended for simulating deployments of this nature.

To allow for large displacements, stabilization in Abaqus introduces artificial viscous damping forces, such that the fundamental equation becomes

$$F_{external} - F_{internal} - c\Delta u/\Delta t = 0,$$

where c is the damping factor, Δu is the vector of nodal displacements, and Δt is the time increment. Unlike a static analysis, a stabilized static analysis does have time dependence, even if time has no meaning in the simulation. The damping factor c must be chosen so that Δu is kept sufficiently small in each time increment. By default, Abaqus automatically sets the value of c to be some small fraction of the extrapolated strain energy. The effect of this fraction is discussed in Section 4.6.

A stabilized static analysis is thus similar to a dynamic analysis, in that it allows for large displacements and has some time dependence. Indeed, it will be shown in Section 4.6 that bulk displacements computed dynamically or statically with stabilization are identical. The key difference is that the dynamic analysis will capture vibrations, whereas the stabilized static analysis is effectively infinitely

damped. Thus, the stabilized static analysis may run significantly faster than the equivalent dynamic analysis, and is a good option when vibrations can be reasonably ignored and time has no bearing on the result.

To deploy the module, zero-displacement or zero-velocity boundary conditions are applied to prevent any rigid body motion. Then, one or several nodes are chosen to be controlled. A fixed velocity is applied to these nodes. This velocity is sufficiently small, such that the control is working against the spring forces and restraining the module. The user subroutine UAMP tracks the reaction forces at the bounded nodes after each time increment, particularly in the direction of control. UAMP sets the velocity to 0 once the controlled node(s) has either reached a set displacement or the reaction forces in the bounded nodes indicate that the control has started pulling on the module. At this point, it is possible that some hinges still have not latched and are continuing to apply forces on the module, meaning that an equilibrium state has not yet been reached. The simulation continues for some time after control ceases to allow the structure to equilibrate. Again, purely spring-actuated displacements with no external control are possible because of the stabilization effect.

A suite of Python code is used to rapidly generate models and simulate their deployment in Abaqus. The model variables file is written and passed to the set of functions defined in `create_model.py`. If the endpoints matrix is provided as a file, then that file is read and stored. If only the PACTRUSS dimensions are provided, then the PACTRUSS endpoints matrix is generated using those dimensions and stored. A number of equally spaced 2-node beam elements are created to model each member, with the number defined in the model variables file. The coordinates of the nodes and the node indices that connect each element are stored. The connectivity matrix is also read and stored. The model variables file, beam nodes, beam elements, and connectivity matrix are then passed to the function `write_input_file.py`. This purpose of this function is to generate an Abaqus input file, written in the Abaqus keywords language. It first writes the beam nodes and elements. Then it steps through each entry in the connectivity matrix, calling subfunctions to write the nodes and elements required to create the type of connection, as well as the behavior of that connection. The Abaqus model is completed by defining materials and lumped masses where necessary. `write_input_file.py` then calls another function, `write_fortran.py`, to write the Fortran-based user subroutines that are necessary to define the Rolamite behavior.

The next action for `write_input_file.py` is to write the Abaqus simulation procedure, including the boundary conditions and the control method. The function `write_fortran.py` also writes the user subroutine UAMP to track reaction forces and set the controlled node velocity. Once the input file and Fortran code are written, another function is called to pass these files to Abaqus. The key Python functions required to run one deployment simulation are graphically depicted in Figure 3.12.

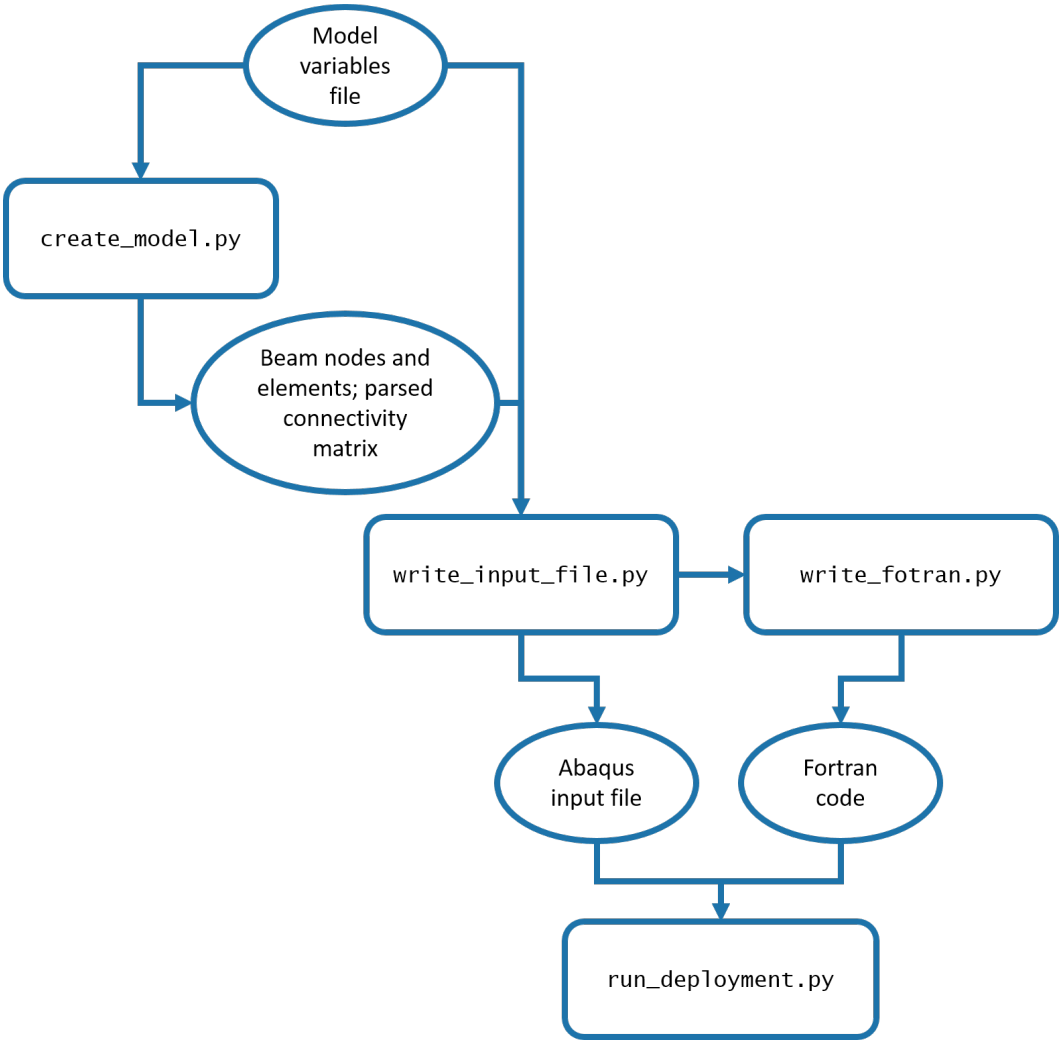

Figure 3.12: Flow chart of the high-level process for running a single deployment simulation. The box components are Python functions and the circle components are inputs and outputs to those functions.

3.3 Monte Carlo Simulation Method to Estimate Reliability

This section describes the Monte Carlo analysis used to simulate the deployment of many models with unique error distributions and compute an estimate for

reliability. Two basic assumptions are made about the deployment behavior:

- For a model of nominal geometry, the simulated deployment will meet the imposed success criteria.
- If the model has errors that sufficiently alter it from the nominal geometry, the simulated deployment may not meet the imposed success criteria.

The success criteria can be any deployment characteristics; in the case of the PACTRUSS model, the criterion is that all of the Rolamite hinges latch. The reliability of the deployment is the likelihood of success for a model with errors below some maximum level. Estimating the reliability requires rapidly simulating the deployment of many models, each with a unique error distribution, and concurrently determining whether each deployment was successful. A suite of Python functions was developed to perform this task.

At the lowest level of the Monte Carlo analysis is the method for simulating a single deployment, described in Section 3.2. Again, this method can automatically generate a unique and random set of errors given the maximum error levels. The next level is the `get_odb_data.py` function. For one deployment simulation, Abaqus writes 10 job files, each with the same file name but a different extension. Each of these files contains a different set of information, but the one containing all of the simulation results is the output database (ODB) file. When passed an ODB file, `get_odb_data.py` uses Abaqus's native Python environment to open the file and extract the data necessary to determine if the deployment was a success or failure. In the case of the PACTRUSS model, this includes the rotations of the Rolamite hinges for each time increment. The data set is then stored and returned for later use. A result flag reading either SUCCESS or FAIL is also returned.

The next level of code is the `main.py` function, which calls the deployment method and `get_odb_data.py` n times, where n is the number of trials. For each trial, the model variables file is unchanged; the nominal model remains the same, but the error distribution changes based on the random sampling. The process is as follows:

1. `main.py` is provided the number of trials and the path to the data storage folder.

2. The data storage folder is checked for any existing ODB files. If the option to append existing data is set, then each existing ODB file is passed to `get_odb_data.py`. The outputted data and the result flag are stored.

3. For i in n trials:

   a) The deployment method is called, which generates an input file and passes this to Abaqus. Abaqus outputs 10 job files, each starting with the file name *file*. Any existing job files with that file name are overwritten.

   b) The ODB file is passed to `get_odb_data.py`. The outputted data set and result flag are stored.

   c) The ODB is copied, renamed as *file_i.odb*, and moved to the data storage folder. This is the only job file that is kept and not overwritten by the next simulation.

4. After n trials, the stored data for each trial is compiled and pickled for later use[1]. The pickled file is moved to the data storage folder. A log file containing all information from the model variables file and the result flags from each trial is written. The result flags labeled SUCCESS are counted and the percentage of successful trials is outputted.

The result is an estimate of the deployment reliability for the given model with the given maximum error levels. At the highest level of the Python suite is the ability to estimate how reliability is affected by changing the model. This is performed by the function `wrapper.py`, which overwrites the model variables file with new parameters. For instance, to study how the member outer diameter d_o affects reliability, a vector of d_o values to be tested is generated. For each d_o value, `wrapper.py` changes the model variables file to reflect the new value and calls `main.py` to obtain a reliability estimate for the current model. The entire Monte Carlo analysis process is illustrated in Figure 3.13.

3.4 Chapter Conclusions

In this chapter, the reliability estimation toolkit was described in detail. While the wedge and PACTRUSS modules were used as examples, the generality of the toolkit to any deployable structure was emphasized. Intended to be used in the

[1] Pickling is a Python function that can compile data structures and save them to a file. That file can later be "unpickled" to retrieve the data.

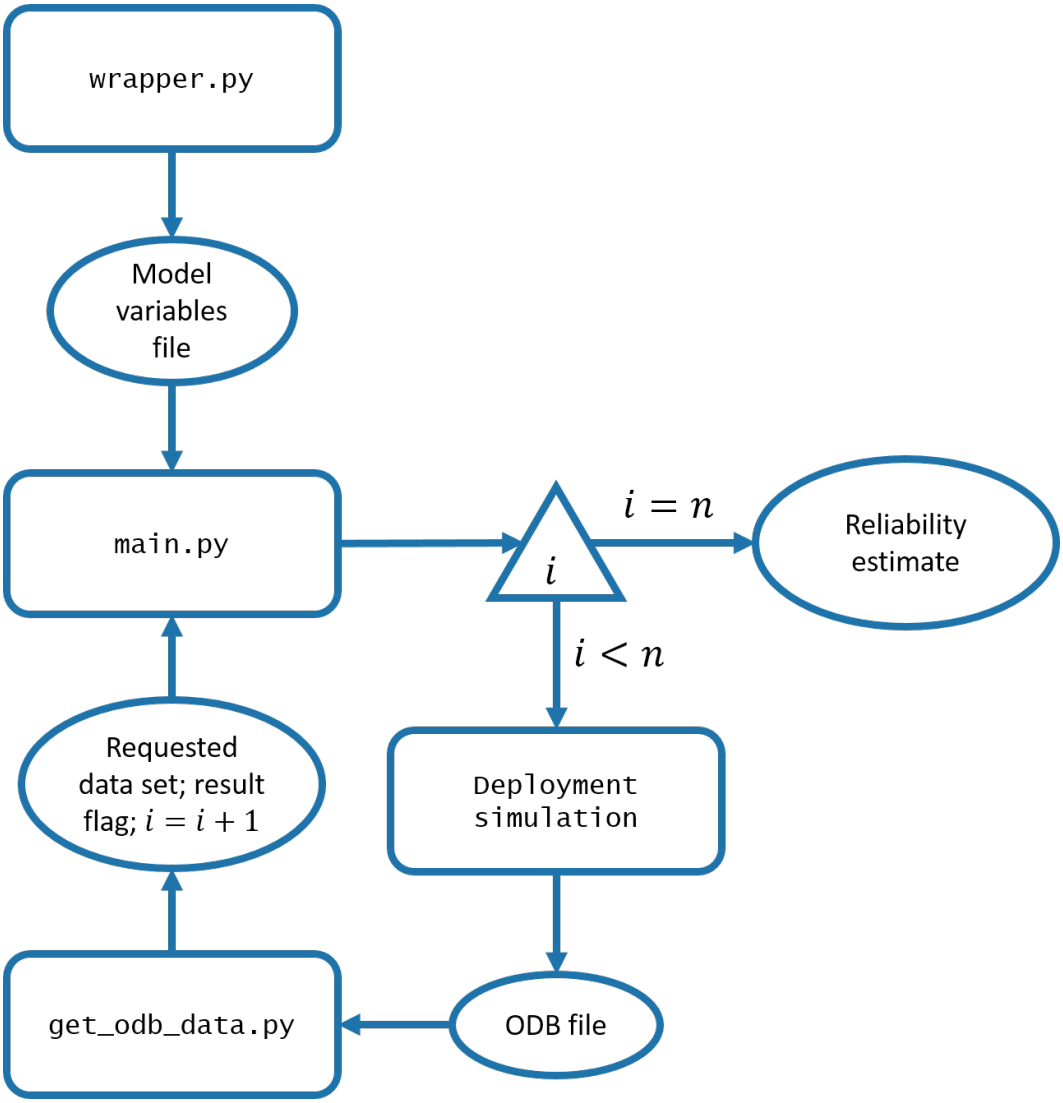

Figure 3.13: Flow chart of the high-level process for running a Monte Carlo analysis to estimate reliability. The box components are Python functions and the oval components are inputs and outputs to those functions. The triangle component is a switch based on the number of iterations i, where n is the maximum number of iterations.

early stages of mission formulation and design, this toolkit can rapidly estimate deployment reliability and produce trade studies for the module design. It is thus a powerful resource for design optimization and the establishment of a key criterion for the feasibility of any mission that requires the deployment of many modules.

Chapter 4

EXPERIMENTAL VALIDATION OF DEPLOYMENT SIMULATION

Critical to the development of the toolkit is experimental validation, necessary to ensure that the deployment simulation results are realistic. Specifically, the toolkit should accurately predict whether a deployment has failed, which would largely be due to any Rolamite hinge not latching. To perform this validation, a physical wedge module was constructed and recreated in the simulation model. Figure 4.1 shows an image of the wedge and experimental setup. The wedge was chosen over the full PACTRUSS module because it could be easily manufactured and deployed simply by moving two vertical members apart in one direction. Two key quantities were used as comparison measures between simulations and experiments: nodal displacements and Rolamite hinge rotations. In this chapter, the first two sections describe the experimental module and equivalent simulation model. Then the experimental equipment and measurement systems and the corresponding simulation boundary conditions and analysis properties are outlined. Finally, the results from the experiment and simulation are presented and compared.

Some of the content in this chapter has been adapted from: Kristina Hogstrom et al. "Methods for Characterizing and Increasing the Reliability of Deployable Modules for Large Optical Reflectors." In: 3rd AIAA Spacecraft Structures Conference, AIAA Science and Technology Forum and Exposition. 2016.

4.1 Experimental Module Geometry

This section describes the overall design and construction of the experimental module. Specific attention will be given to the Rolamite hinges in Section 4.2. The nominal design dimensions of the module are given in Table 4.1. Refer to Section 3.1 for a description of the variables. A CAD image of the module is shown in Figure 4.2. The members were fabric weave carbon fiber composite tubing obtained from RockWest Composites. The joints were 3D-printed with ABS plastic on a Stratasys printer. The vertical members were attached to the joints by gluing them to a joint shaft that seated into the member internally, as shown in Figure 4.2. Similarly, each longeron and diagonal member was glued to 3D-printed member attachments on both ends. Custom jigs were used to mitigate length errors and misalignments while

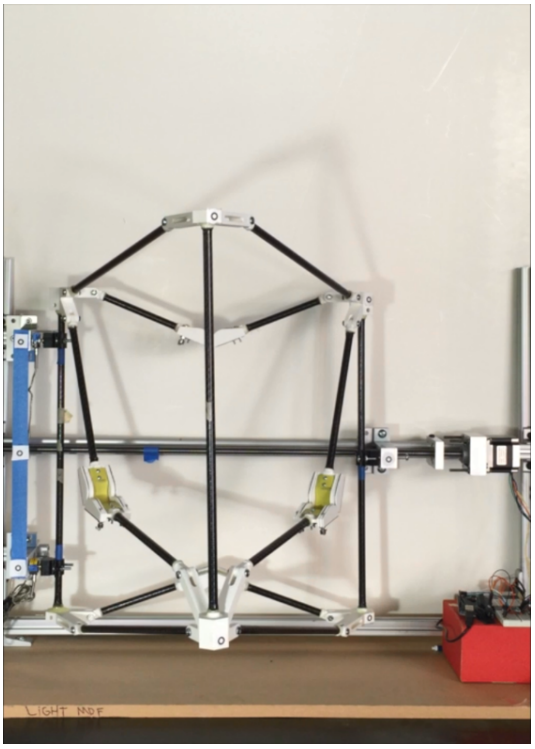

Figure 4.1: Photograph taken of the experimental wedge and setup.

Property	Value	Source
L	50 cm	
H	50 cm	
q	13 cm	
l_j	4 cm	
d_o	1.1303 cm	
t	0.0889 cm	
E_m	142 GPa	[59]
ρ_m	1820 kg/m^3	[59]
ν_m	0.1	[60]

Table 4.1: Experimental geometry and member properties. Sources cited where applicable.

gluing. The member attachments were hinged to the joints with a single machine screw; the screw holes were slightly oversized to allow free rotation over the threads.

In the simulation model, the member material is assumed to be isotropic. Hence the material properties given in Table 4.1 are approximated global properties of the CFC material. Also in the model, the joints are treated as single beam elements with uniform rectangular cross-section. These joint beams share a node with each

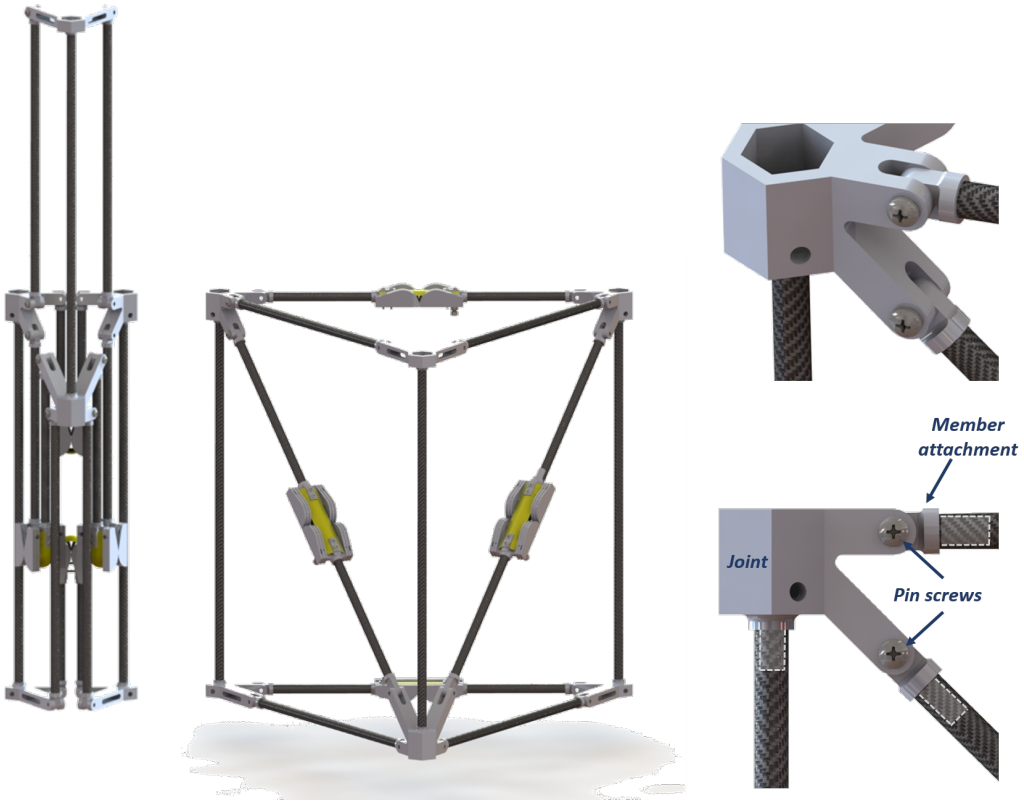

Figure 4.2: (Left) Rendering of the experimental module. (Right) Detail of a joint. The dashed outlines show the inner shafts that are glued to the members.

other and with the end of the vertical member, but otherwise do not interact. The joint model is shown superimposed on the actual experimental joint in Figure 4.3. Clearly, the experimental joints do not have uniform cross-section, and so the model cannot exactly replicate the joint behavior. The cross-section is approximated in the model by setting b_j equal to the average height of the protruding part of the joints and a_j equal to twice the width of the tabs that surround the member attachment. Rather than provide a joint density and allow the model to automatically compute the mass, the actual mass of each joint was measured and applied to the model as a lumped mass, located at the shared node shown in Figure 4.3. Reasonable estimates of the joint compliance properties were obtained by simply pushing and pulling on the module after construction in various locations and observing how much it moved. The value of k_{low} was obtained by estimating that the force exerted by the finger to push the joint to the end of the slack region was 25 N. The joint properties are given in Table 4.2.

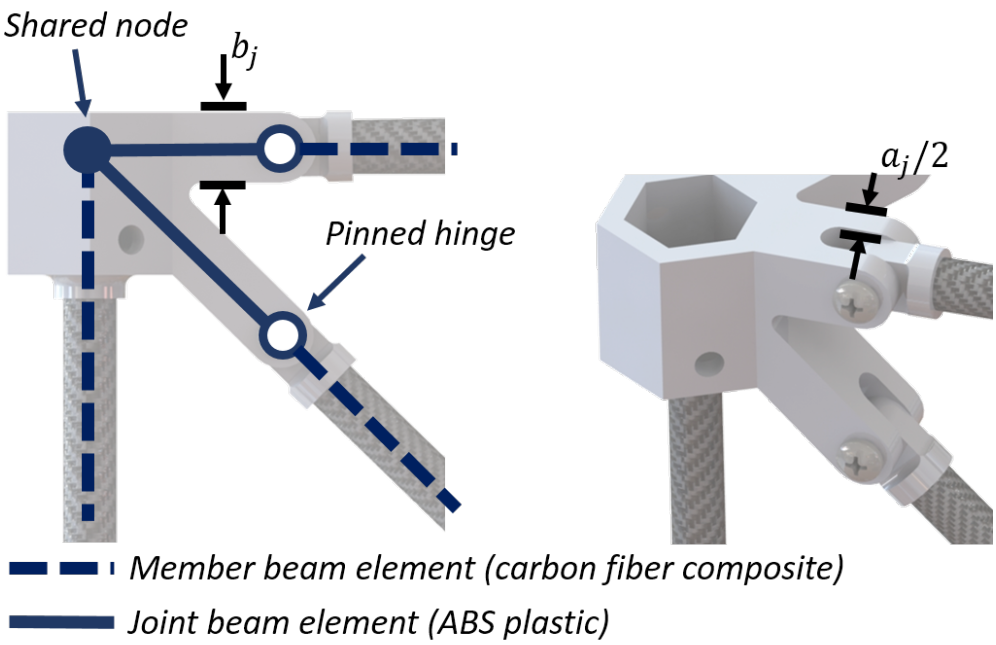

Figure 4.3: Model of a joint superimposed on the actual joint to illustrate the approximations made.

Property	Value	Source
E_j	2.2 GPa	[61]
ν_j	0.35	[62]
a_j	1.25 cm	
b_j	1.45 cm	
δ_{stop}	750 μm	
k_{low}	10^4 N/m	
k_{high}	10^6 N/m	
θ_{stop}	2°	

Table 4.2: Experimental joint properties. Sources cited where applicable.

4.2 Experimental Rolamite Hinges

Each of the four Rolamite hinges were constructed with the same nominal dimensions, given in Table 4.3. The tape sections were cut from standard tape measure obtained at a hardware store. The cam sets were 3D-printed with ABS plastic.

Given these dimensions, the analytical equations given in Section 3.1 predict that the maximum latching moment and minimum deployment moment for this hinge design are 12.96 Nm and 0.065 Nm respectively. In order to obtain a more detailed moment-rotation profile, an experiment was performed using a test hinge

Property	Value	Source
p	42 mm	
μ	26 mm	
L_{rol}	110 mm	
t_t	0.1 mm	[55]
α	1.7 radians	[55]
r_t	15 mm	[55]
e_t	1.35 mm	[55]
L_t	70 mm	
h_t	16.7 mm	
d_t	8 mm	
E_t	210 GPa	[55]
I_t	4.67 mm^4	[55]
A_t	2.55 mm^2	[55]

Table 4.3: Experimental Rolamite hinge dimensions. Since the same tape was used by Watt, many of the values are taken from that source.

with the same nominal dimensions. The experimental setup is shown in Figure 4.4. The cams on the test hinge were printed with large attachments that each screwed onto a gear. The gears were equipped with strain gauges to measure the torques M_1 and M_2 imparted by the hinge. Starting from the fully folded position, each gear was rotated independently by turning the knobs until the total rotation in the hinge was approximately $\Delta\theta$, such that $\theta_1 = \theta_2$ and $\Delta\theta = \Delta\theta_1 + \Delta\theta_2$. At this point, θ_2 was adjusted so that the readings of M_1 and M_2 were approximately equal. The final values of θ_1, θ_2, M_1, and M_2 were recorded. The process was repeated with small rotation increments until the hinge was fully open. The entire test was then repeated three times.

The results of the experiment are shown in Figure 4.5. The markers represent the measured values of $\theta = \theta_1 + \theta_2$ vs. $M = (M_1 + M_2)/2$. Because the torques were matched, rather than the angles, the value of $\Delta\theta$ was not exactly equal for each increment. The blue line was obtained by averaging both θ and M over the three tests. The average standard deviation of the three rotation measurements across all increments was 0.45°, which gives a sense of the resolution of the measurement. Similarly, the average standard deviation in the moment was 0.03 Nm. The figure shows that the predicted value of the minimum deployment moment is well matched with the experiments. However, this experimental method did not have the resolution required to capture the peak of the latching region. In the simulation model, θ_c is set to the rotation corresponding to the peak of the blue curve, 176.5°. The Rolamite

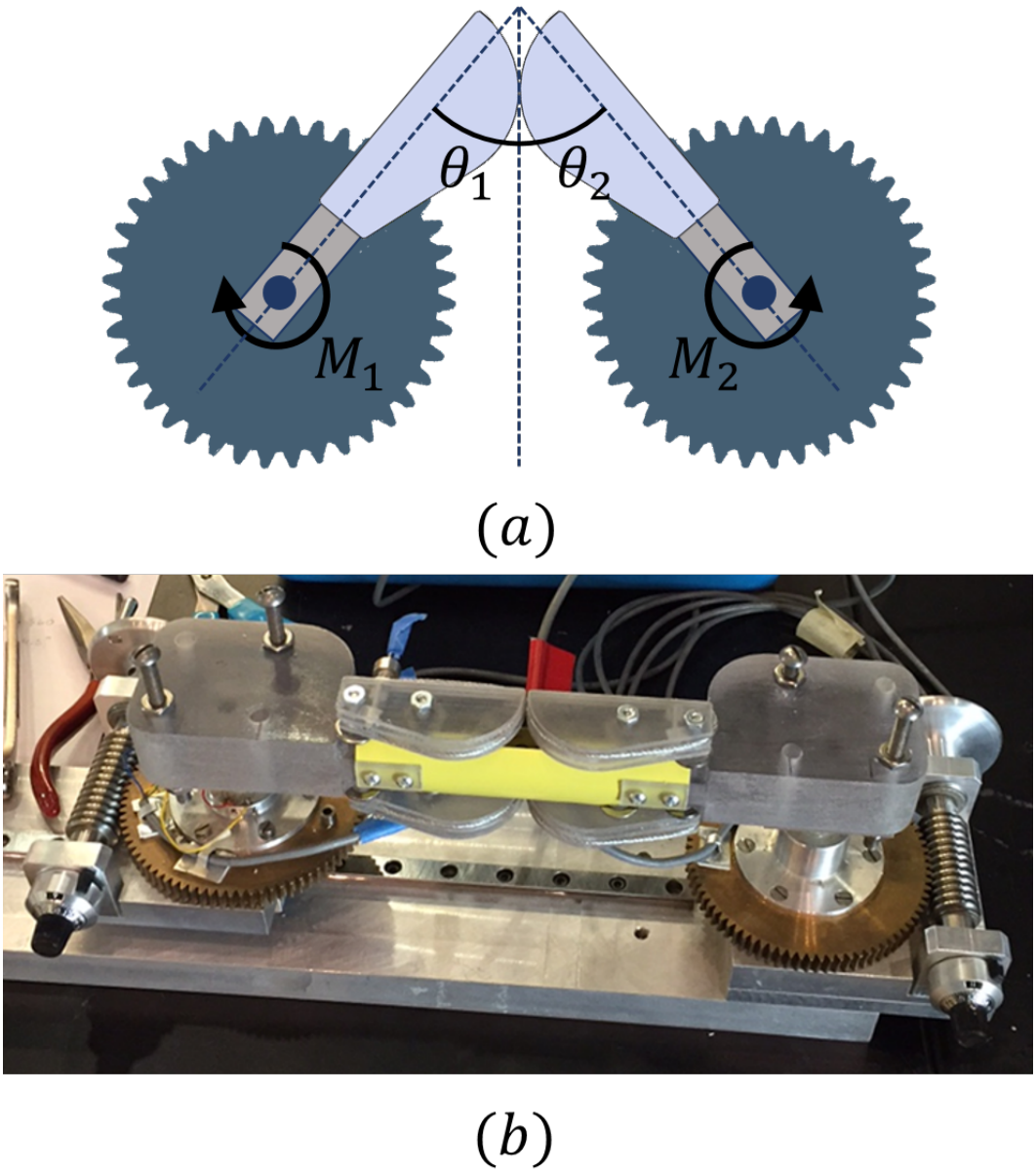

Figure 4.4: Sketch (upper) and photograph (lower) of the Rolamite hinge experiment.

hinges follow the experimentally determined moment-rotation curve until $\theta = \theta_c$. At this point, the analytically determined latching curve is followed.

4.3 Experiment Design and Measurements

4.3.1 Actuating Deployment

As previously mentioned, the wedge can be deployed simply by displacing one of the verticals attached to the folding longeron face along a line perpendicular to its axis. The frame and motor system used to actuate the deployment is shown in

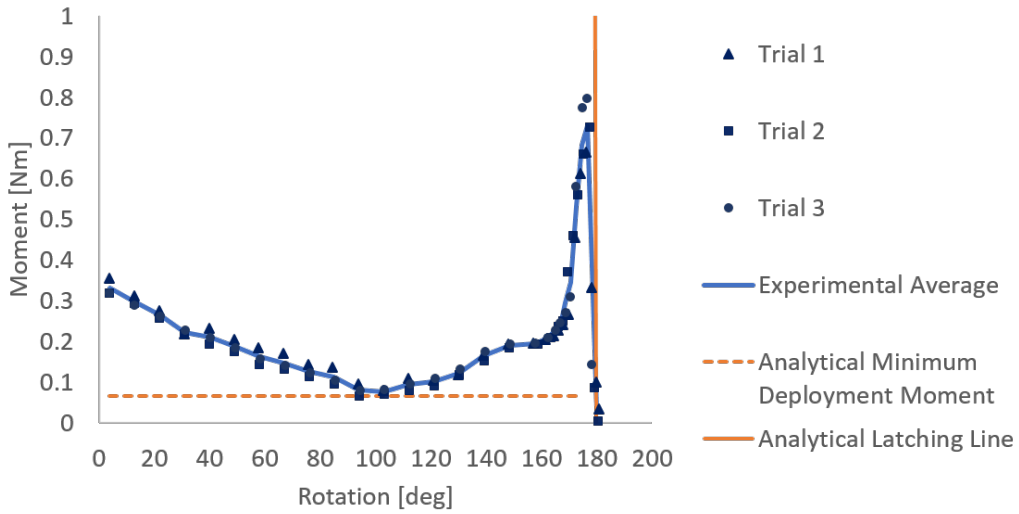

Figure 4.5: Moment vs. rotation curve as measured by the experiment and computed with analytical techniques.

Figure 4.6. The back left vertical was rigidly attached to the frame, with load cells located at the attachment points to measure reaction forces in the y direction. The back right vertical was attached to a carriage with threaded hole. A lead screw was placed through the carriage hole and attached to a motor. When the motor was powered, the lead screw turned and the carriage moved linearly along the frame in the y direction, thereby opening the module.

The motor system was designed to stop automatically when the net reaction force registered by the load cells was in tension. Figure 4.7 illustrates the components of the motor system. The main driving function was written in MATLAB. An Arduino was programmed to send and receive signals from MATLAB. To start the deployment, MATLAB instructed the Arduino to drive the motor. The forces in the load cells were computed using a Vishay P3 strain indicator, which streamed the data to MATLAB. During the deployment, MATLAB monitored the load cell readings. Once the sum of the forces reached some tolerance in tension, MATLAB signaled the Arduino to stop the motor. The tolerance was not set to be the exact switch between net compression and net tension (0 N), but rather a small force of 10 N to account for any minor errors and instabilities.

4.3.2 Measuring Displacements

Markers were placed on the structure and their displacements tracked with a stereo camera pair, as shown in Figure 4.8. Marker 1 was attached to the point on

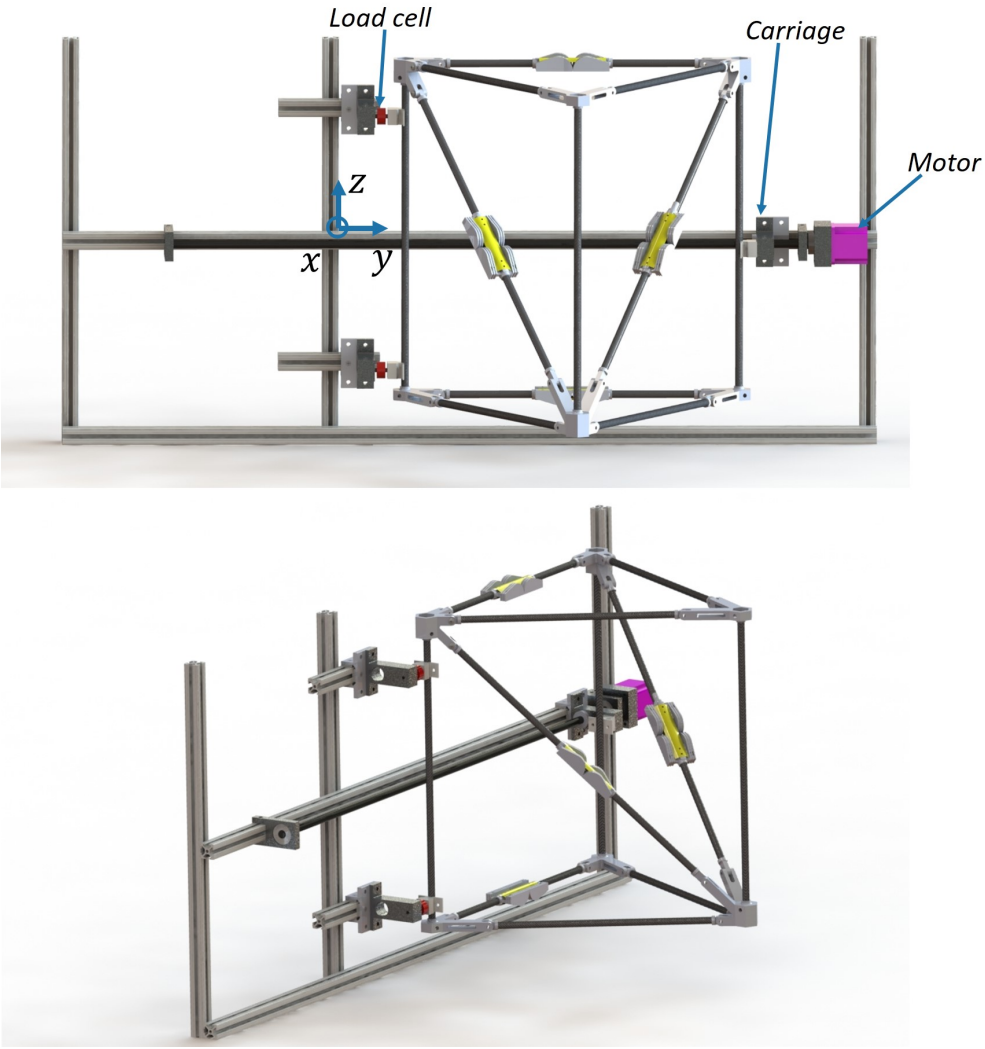

Figure 4.6: Image of the experiment frame. One vertical member of the module is attached to load cells that are rigidly attached to the frame. Another vertical member is connected to a carriage that is threaded onto a lead screw. The motor turns the lead screw, which then moves the carriage linearly along the frame.

the structure used for comparison to simulations; the selection is discussed in more detail in Section 4.5. Marker 2 was attached to the carriage, and was therefore used to track the controlled displacement. Markers 3 and 4 remained stationary during deployment and were used to establish the coordinate system, with marker 4 as the origin, the vector from 4 to 2 as y axis, and markers 2-4 establishing the $y-z$ plane.

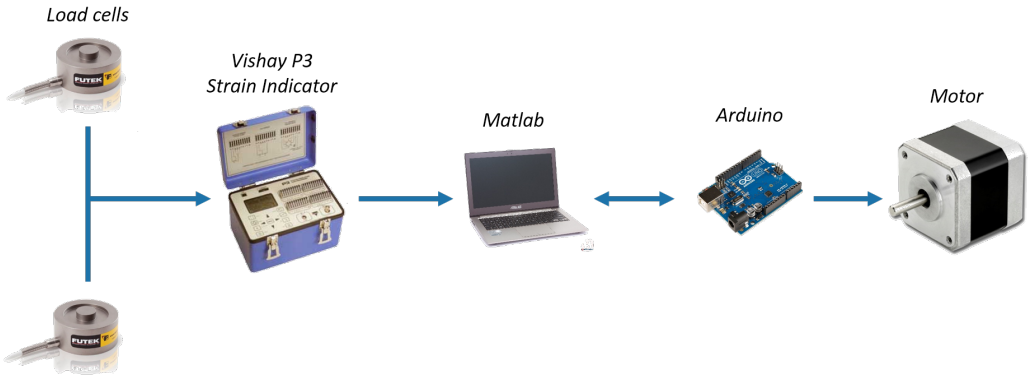

Figure 4.7: Equipment used to actuate deployment.

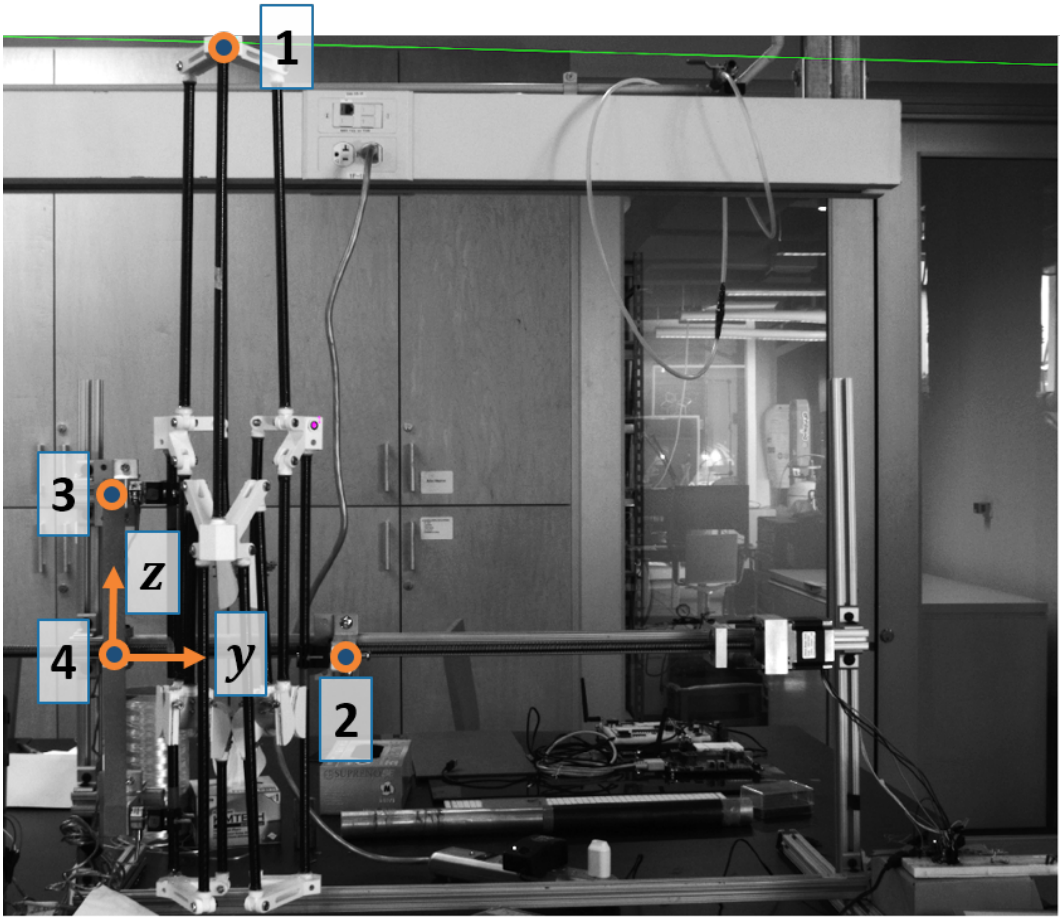

Figure 4.8: Photograph taken by one of the cameras in the stereo pair. The locations of the tracking markers are highlighted.

4.3.3 Measuring Hinge Rotations

Simple iPhone cameras were used to record each of the four Rolamite hinges, the visible bottom edges of which were painted red to increase visibility. When the

deployment was approximately 80% complete, the motor was paused and each of the cameras started recording. A bright light was flashed to create a common time marker and align the separate videos. After the flash, the motor was restarted and the deployment completed. Only the last 20% of the deployment was captured by the 2D iPhone cameras in order to keep rigid body out-of-plane motions minimal. In MATLAB, each of the videos were split into separate frames. An automatic routine was written to identify the red edges in each frame using the Hough transform. However, this procedure often found more than just the two edges. In order to make sure that the right edges were recorded, the endpoints of the edges were selected manually for a small set of frames at even intervals in time. The slopes of the edges were computed from the estimated endpoints, and the results were interpolated to obtain slope estimates for each frame. Then the slopes of the edges computed by the Hough transform were compared to the estimated slopes and only the close matches were kept. The angle between the edges, or the rotation of the hinge, was then computed and stored for each frame. An example of the manual endpoint selection and automatic edge detection is shown in Figure 4.9. To estimate the precision associated with this process, each hinge was observed at a constant angle for some time. The angle was computed for each frame, yielding a mean and standard deviation. For the four angles and four tests, the maximum standard deviation was 0.91°.

During the experiment, the time at which the motor paused was recorded. The stereo camera data was aligned with the hinge data by matching this time with the approximate time at which the hinges began rotating in the videos.

4.4 Equivalent Simulation Boundary Conditions and Step Properties

Figure 4.10 shows the global coordinate system and boundary conditions applied to the simulated wedge deployment, chosen to recreate those in the experiment. The nodes marked with squares are constrained to have zero displacement in all six degrees of freedom. The node marked with a triangle is the controlled node, constrained in all rotations and in x and z. During deployment, the controlled node moves along the y axis with a constant velocity. For the bulk of the deployment, the control node constrains the structure against the springs, and so the reaction forces at the fixed nodes in the y direction are net positive. When these reaction forces sum to -10 N, or 10 N in tension, the control velocity is set to 0. In this case, once the control stops, the simulation also stops. The baseline step parameters are given in Table 4.4. For the model without any errors, the controlled node moves a total of

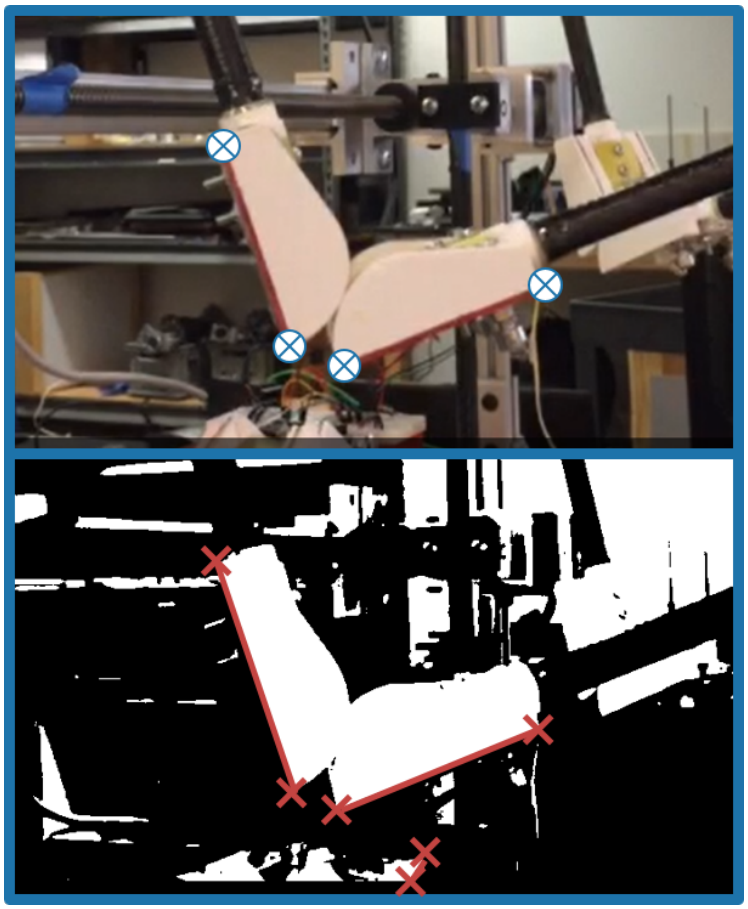

Figure 4.9: (Top) One frame from a video of the Rolamite hinge. The markers represent the endpoints manually estimated and selected. (Bottom) The same frame after using the Hough transform to detect edges. Note the unwanted edge at the bottom of the frame. This edge is disregarded, because its slope does not match either of the slopes estimated from the manual endpoint process.

Initial time step	.01 s
Maximum time step	.01 s
Control velocity	1 m/s
Stabilization fraction	5×10^{-7}

Table 4.4: Baseline step properties for the stabilized static analysis procedure.

$L - q = 37$ cm. Given the control velocity of 1 m/s, the total step time is about 0.37 s. The step time may be slightly longer or shorter if errors are applied, depending on when the reaction force stop criterion is met. The choice of stabilization fraction will be discussed in Section 4.6.

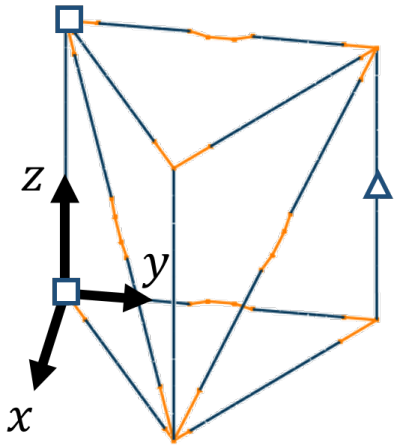

Figure 4.10: Boundary conditions applied to the wedge deployment simulation. The nodes marked with squares are fixed in space. The node marked with a triangle is the controlled node, which moves along the y axis with a constant velocity until the net y reaction forces in the fixed nodes are in tension.

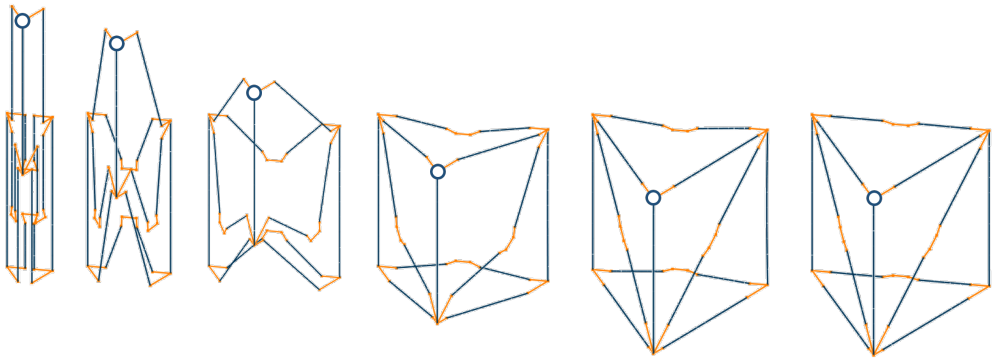

Figure 4.11: Stages of the simulated deployment of a perfect wedge model.

4.5 Results for a Perfect Module

To illustrate the deployment behavior and key characteristics that can be used as comparison measures between models, this section considers the perfect wedge model, such that the geometry is nominal and no errors are applied. Figure 4.11 shows stages of the simulated deployment. Figure 4.12 plots the rotations of each of the Rolamite hinges plotted against the displacement of the controlled node. Here, upper, lower, right, and left refer to the orientation shown in Figure 4.2. It is evident from the inset that the two diagonal hinges latch at the same time, followed by the bottom folding longeron and the top folding longeron in close succession.

Figure 4.13 shows the displacement of the node marked with a circle in Figure 4.11, which corresponds to marker 1 tracked by the stereo camera pair. This node is

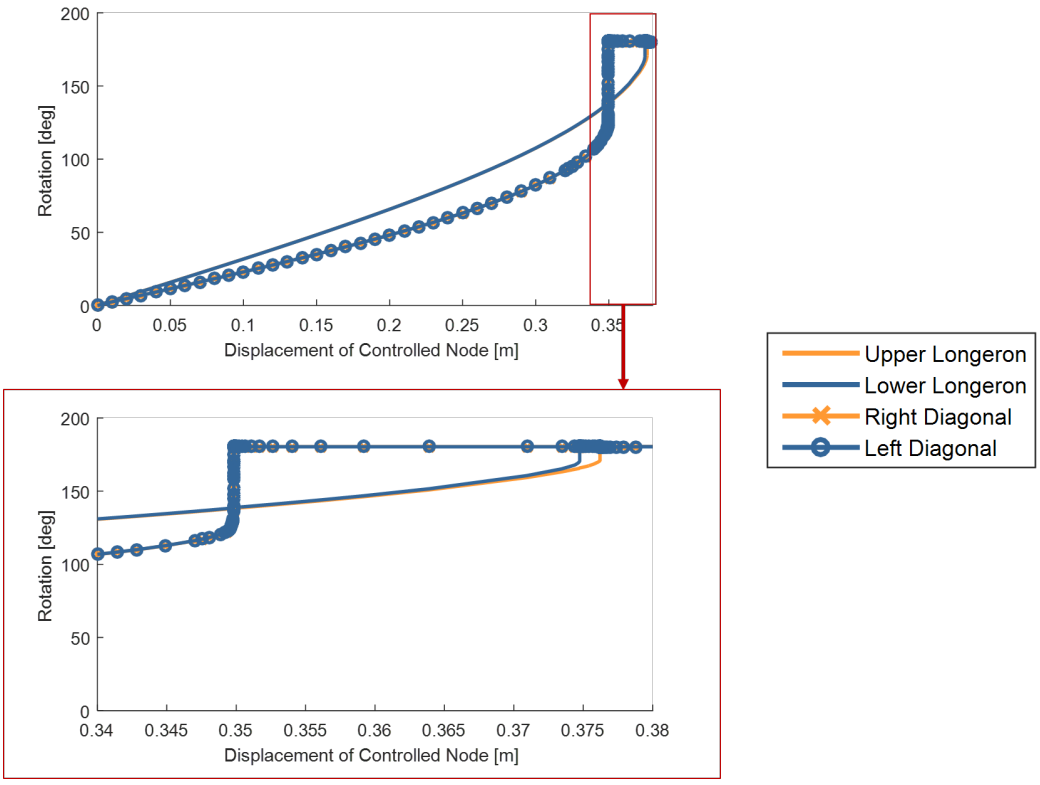

Figure 4.12: Stages of the simulated deployment of a perfect wedge model.

particularly useful for visualizing deployment behavior, because it has bulk motion in all three directions. The figure shows how the node becomes fixed, particularly in the z direction, toward the end of the deployment. This is due to the diagonal hinges latching first and holding the node in z. Since the longeron hinges latch after the diagonal hinges, there is still forced displacement in the y direction that corresponds to the control. Thus, the displacement in x must decrease in order to maintain the lengths of the members, as is evident in the figure.

4.6 Effect of Stabilization Fraction

As previously discussed in Section 3.2, Abaqus automatically sets the stabilization damping coefficient to be some fraction of the extrapolated strain energy. The default value for this fraction is 2×10^{-4}. It was found by trial and error that a value of 5×10^{-7} is sufficient to complete the deployment simulations. If the fraction is too low, then the solver cannot find a solution. In this section, the effect on the solution of increasing the fraction beyond the minimum value is investigated. Consider the case of the perfect wedge model with no velocity control, meaning that deployment is purely spring-actuated. Figure 4.14 plots the hinge rotations for various

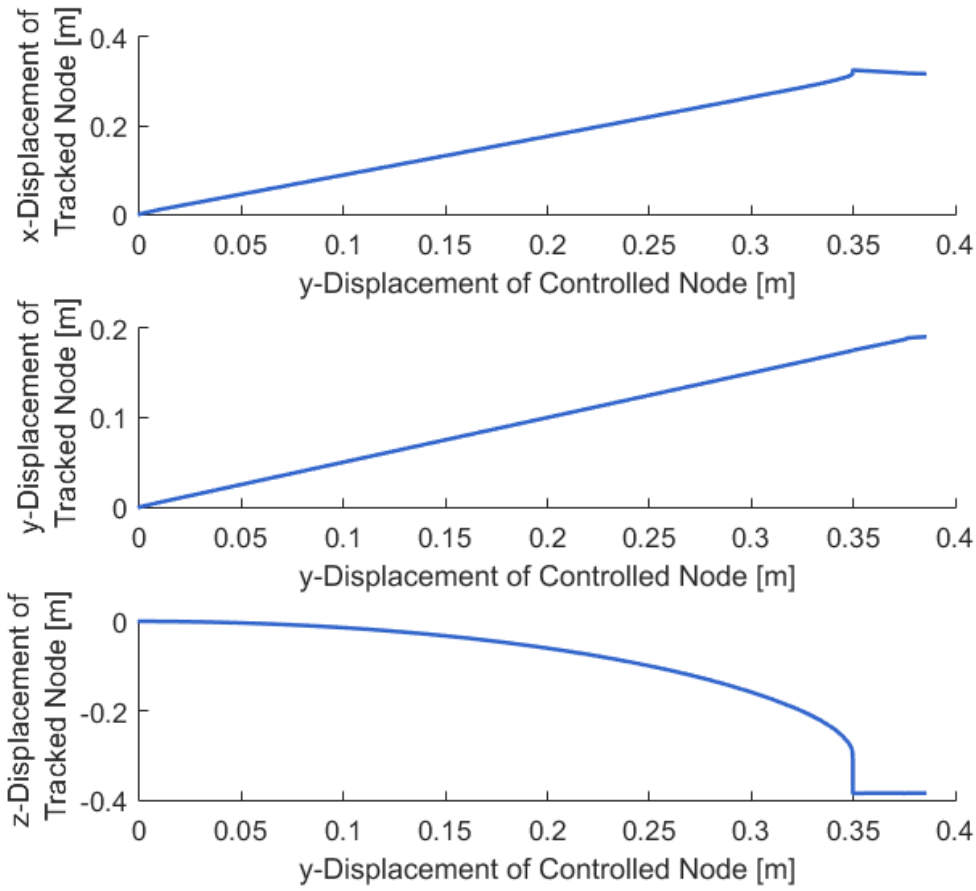

Figure 4.13: Displacement of the node marked in Figure 4.11 vs. y displacement of controlled node.

stabilization fractions as well as the hinge rotations that result from the equivalent undamped dynamic analysis. The rotations are plotted against the y displacement of the node that would otherwise be controlled, but is left free in this case. The figure suggests that changing the stabilization fraction has no effect on the overall deployment behavior. What does change is the artificial time required to complete the deployment. Increasing the fraction increases the magnitude of the energy lost to static dissipation, which decreases the nodal velocities. Thus, smaller fractions lead to shorter deployment times and thus shorter simulation run times.

4.7 Experimental Module Shape Measurements

In order to fairly compare the simulated deployment to the experimental deployment, the shape of the experimental module must be reproduced as closely as

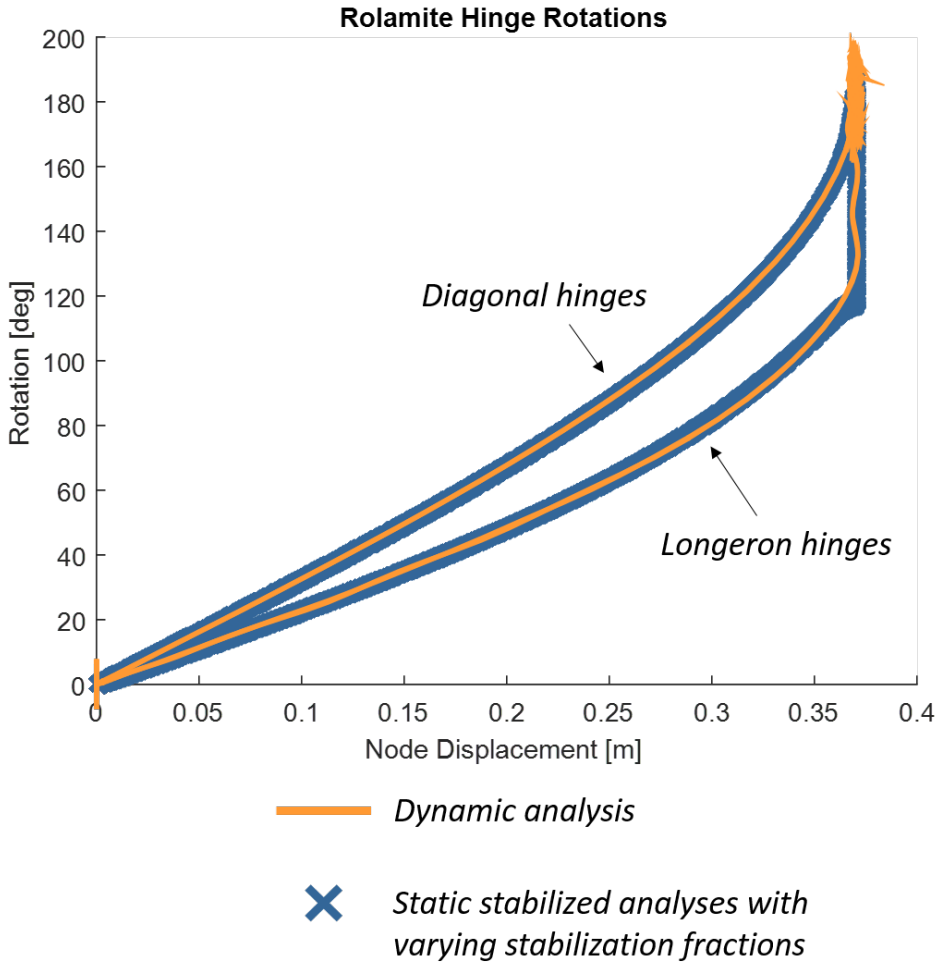

Figure 4.14: Effect of stabilization fraction on Rolamite hinge rotations. The following stabilization fractions were tested: 1×10^{-6}, 5×10^{-6}, 1×10^{-5}, 5×10^{-5}, 1×10^{-4}, 5×10^{-4}, and 1×10^{-3}. The hinge rotations in each case are identical, and so all of the stabilized static results are plotted with the blue markers. The result of the equivalent dynamic analysis is shown in orange. The dynamic analysis clearly includes vibrations; however, the bulk rotations between the dynamic analysis and the stabilized static analyses are the same.

possible in the simulation model, including any errors that were introduced during manufacturing. This requires determining the locations of all joint nodes (points at which member centerlines nominally meet), locations of all pinned hinges, locations of Rolamite hinge member attachment points, all pinned hinge axes, and all Rolamite hinge axes. Unfortunately, the experimental module was not designed to obtain these measurements directly. For instance, the joint node is a point located within the solid 3D-printed joints and thus cannot be immediately accessed. However, all necessary information that cannot be measured directly can be estimated

indirectly from the measurements shown in Figure 4.15. A coordinate measuring device called a FaroArm, shown in Figure 4.16, was used to obtain these measurements while the module was stowed and attached to the experiment frame. Each of the required information sets were obtained as follows:

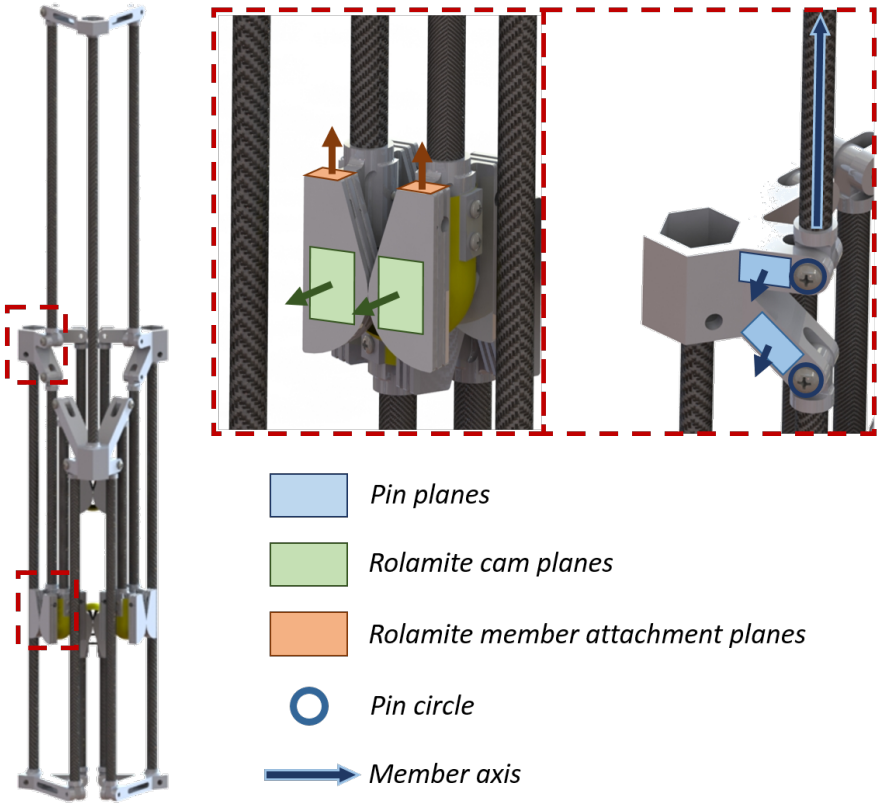

Figure 4.15: Map of measurements taken with the FaroArm. All shown measurements are made for each instance of that feature in the structure. Planes and associated normals are fitted to points measured on the surface. Member axes are fitted to points measured on the outer surface of the member along the length. Pin circles are fitted to points measured on the outer surface of the screw heads where they contact the joints.

- **Pinned hinge locations**: From the pin circles surrounding the screw heads, the pinned hinge locations were obtained by translating the center of the circle -1 cm ($a_j/2$) along the vector normal to the outward pin face, as shown in Figure 4.17.

- **Joint nodes**: For each joint, there are two pinned hinges that attach to longerons. These pinned hinges nominally lie in a plane perpendicular to

Figure 4.16: Image of a FaroArm courtesy of Faro.

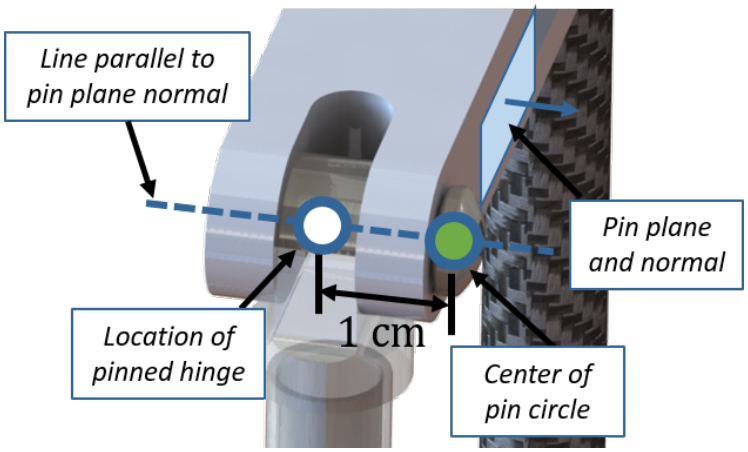

Figure 4.17: Illustration of how the pinned hinge location is determined from the measured pin circle and pin plane.

the axis of the vertical member attached to the joint. The joint node is then nominally the point at which the member axis intersects this plane. In the physical module, errors may alter this alignment. To obtain the joint node, the locations of the two longeron pinned hinges were projected perpendicularly onto the vertical member axis. The joint node was then set as the average between the two projected points, as shown in Figure 4.18.

- **Rolamite hinge member attachment points**: Each member attachment point was obtained by finding the intersection between the member and the associated Rolamite member attachment plane.

- **Pinned hinge axes**: Each pinned hinge axis was assumed to be equal to the outward normal of the associated pin plane.

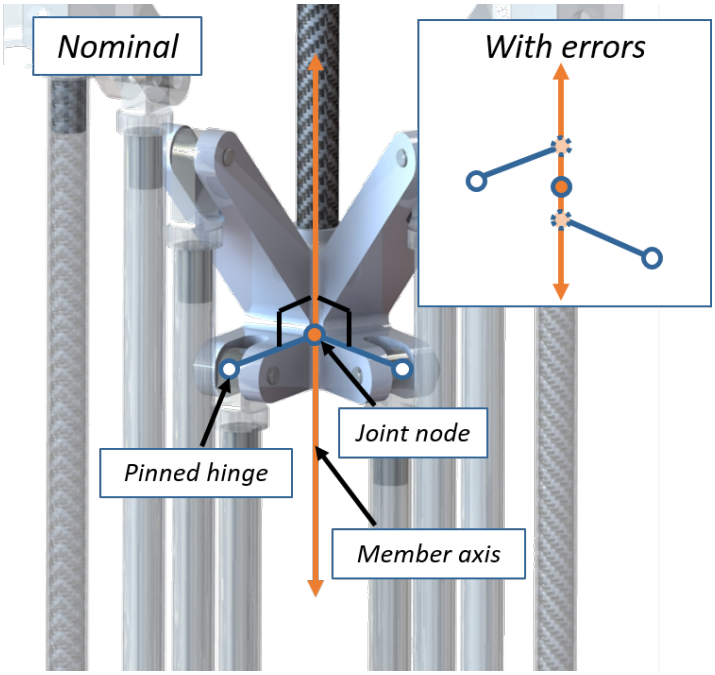

Figure 4.18: Illustration of how the location of the joint node is derived from the axis of the vertical member and the two longeron pinned hinges. For a nominal geometry, the joint node is the location of the perpendicular projection of pinned hinges onto the axis. The inset shows that, when the geometry has errors, the two pinned hinge projections may not align. In this case, the joint node is taken to be the average location of the two projections along the member axis.

- **Rolamite hinge axes**: Each Rolamite hinge axis was assumed to be the average of the two normals associated with the Rolamite cam planes.

Figure 4.19 shows the measured shape of the experimental module superimposed onto nominal shape. It is evident from the figure that the dominating source of error was not the manufacturing process directly but gravity sag enabled by compliance in the joints. Unlike random errors, these errors were relatively consistent throughout the structure and did not significantly hinder the deployment. The FaroArm was used to obtain the shape of the deployed module, and found that, once the structure was stiffened, these errors were reduced to a maximum of 3 mm.

The connectivity and endpoint matrices were created from the FaroArm measurements and fed into the simulation model. It is evident in Figure 4.19 that some of the Rolamite hinges started in a partially open state, with an initial angle of up to 2°. The toolkit accounted for this effect automatically by computing the initial angle between the attached member axes and shifting the moment-rotation curve accordingly.

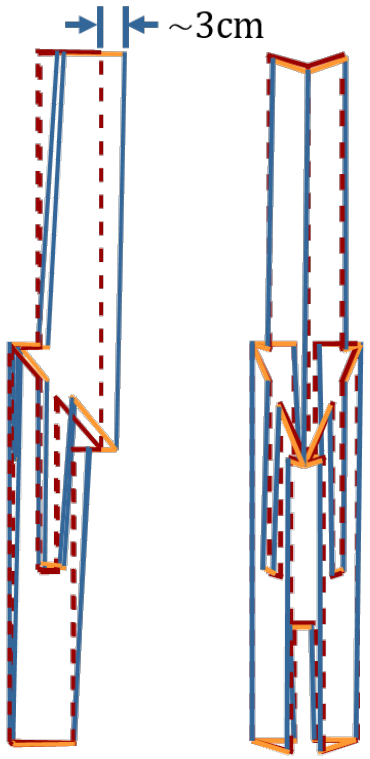

Figure 4.19: Results of FaroArm measurements. The measured members are in blue and measured joints in orange. The nominal shape is plotted with red dashed lines.

4.8 Results and Comparison to Simulations

The entire experiment was repeated four times, from fully stowed to fully deployed. Figure 4.20 shows photos of the deployment at various stages. The sequence reveals the order in which the Rolamite hinges latched. Between stages 5 and 6, the diagonal hinges latched. Between stages 6 and 7, the bottom longeron hinge latched. Finally, in stage 8, the upper longeron hinge latched.

Figure 4.21 plots the hinge rotations extracted from the videos. The independent variable is the displacement of the carriage (marker 2) tracked by the stereo camera pair. Each of the plots corresponds to one of the four tests. The hinges are latched when the rotation reaches approximately 180° and becomes constant. The plot shows that the two diagonal hinges generally followed the same path until just before latching. However, the left diagonal hinge latched first. Unexpectedly, this action temporarily jammed the right hinge, holding it at an intermediate rotation value for a short time, as highlighted by the red oval in the first plot. For the four tests, this value was 168° ± 1°. Eventually the right diagonal hinge did latch,

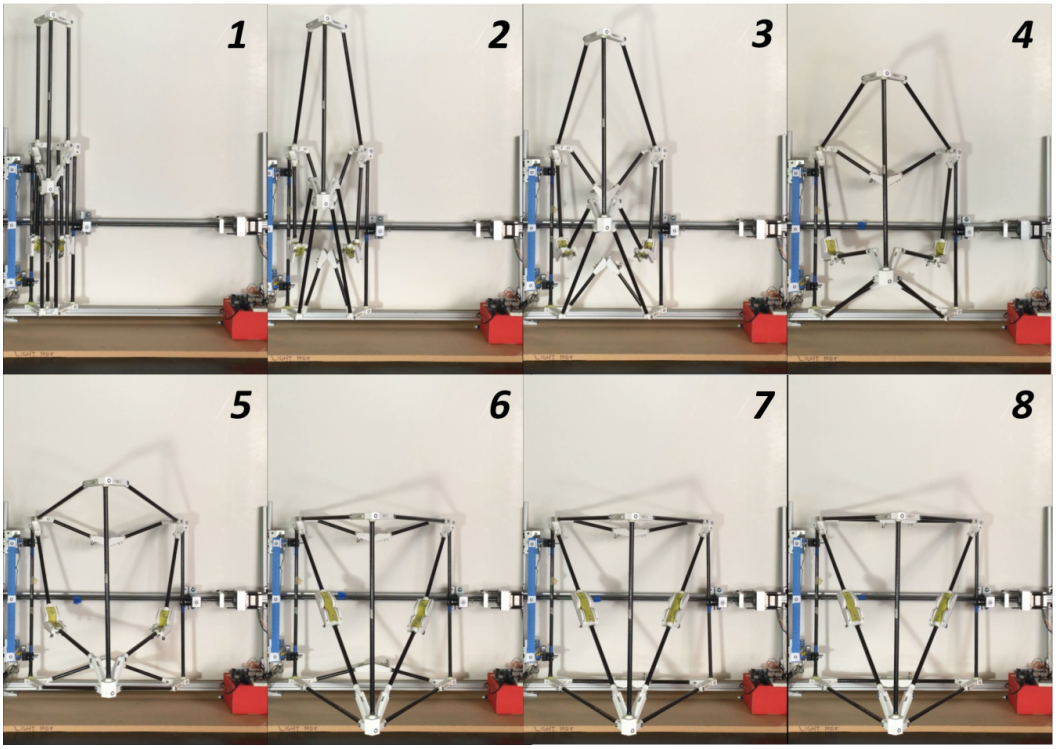

Figure 4.20: Stages of deployment experiment.

followed by the lower longeron hinge and then the upper longeron hinge.

In Figure 4.22, the rotation of each hinge is plotted for all four tests, as well as two simulations. The first simulation is that of the actual module, such that the model was recreated from the FaroArm measurement data. The second simulation is that of the perfect module, the same results presented in Section 4.5. The first observation to note from the figure is that the four tests were very consistent with each other for the bulk of the deployment, with less than 3 mm spreads in the independent variable, as indicated on the fourth plot. The second observation is that the two simulations did yield different results, emphasizing the importance of studying the effect of these errors. As expected, the actual module simulation results generally matched more closely with the experimental results than the perfect module simulation. This is especially evident in the rotation of the lower longeron hinge. There was a discrepancy in the timing of the upper longeron hinge; the simulation of the actual module predicted that it would latch earlier than the lower longeron hinge, and thus the order of latching was different than that observed in experiments. However, the temporary jamming behavior of the right diagonal hinge was precisely predicted by the simulation of the actual module; the simulated intermediate constant rotation of

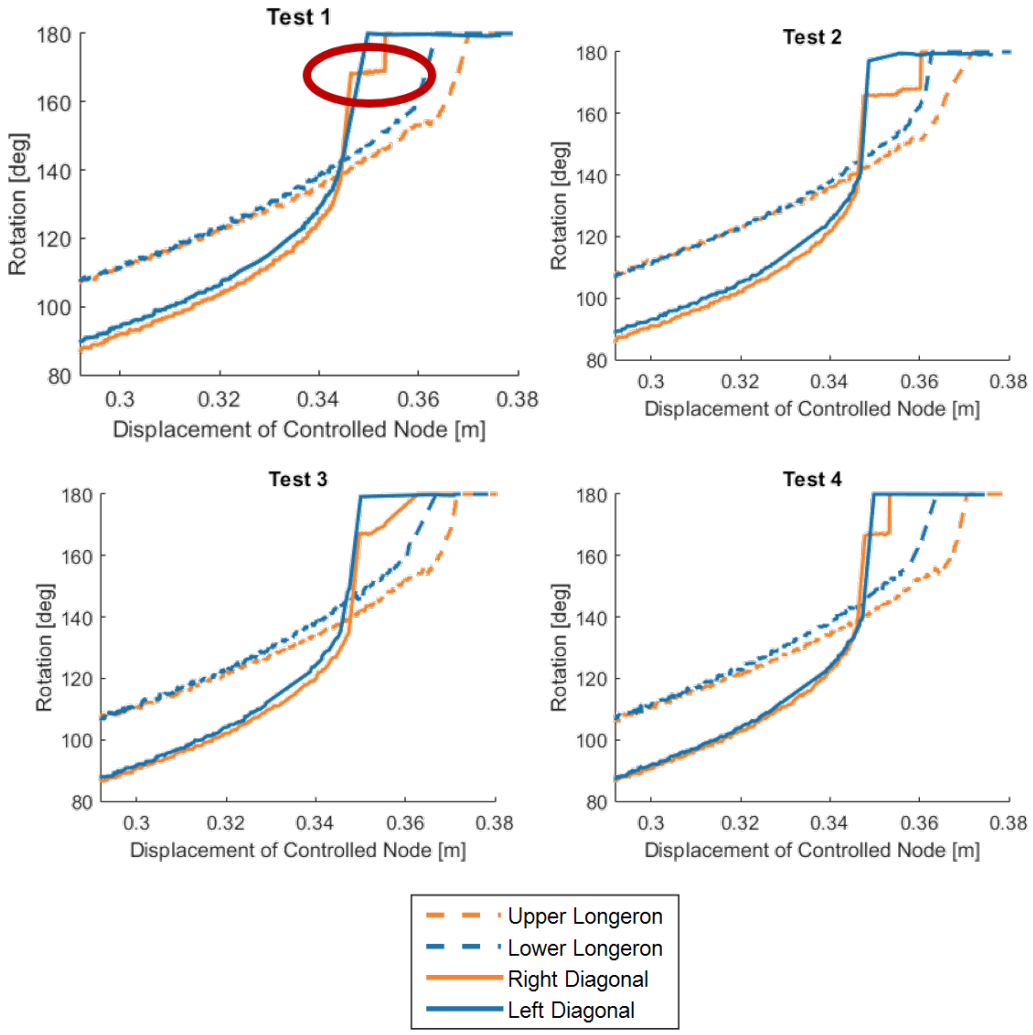

Figure 4.21: Measured hinge rotations for each test. The rotations are plotted against the displacement of the controlled node, as measured by the stereo camera pair.

167.2° was within the error bounds of the experimental results (168° ± 1°). This unexpected behavior was not captured by the simulation of the perfect module.

Figure 4.23 shows the displacement of marker 1 plotted against the displacement of marker 2 for all four tests. The displacement of the equivalent node is also plotted for the simulation of the actual module and the simulation of the perfect module. As with the hinge rotations, the two simulations produced different results. In the experiment and the simulation of the actual module, the total displacement of the controlled node was about the same, indicating that the reaction force stop criterion was met at the same point in the deployment. In the simulation of the perfect module, however, the controlled node moved further before the stop criterion was met. At the end of the deployment, the simulation of the actual module predicted

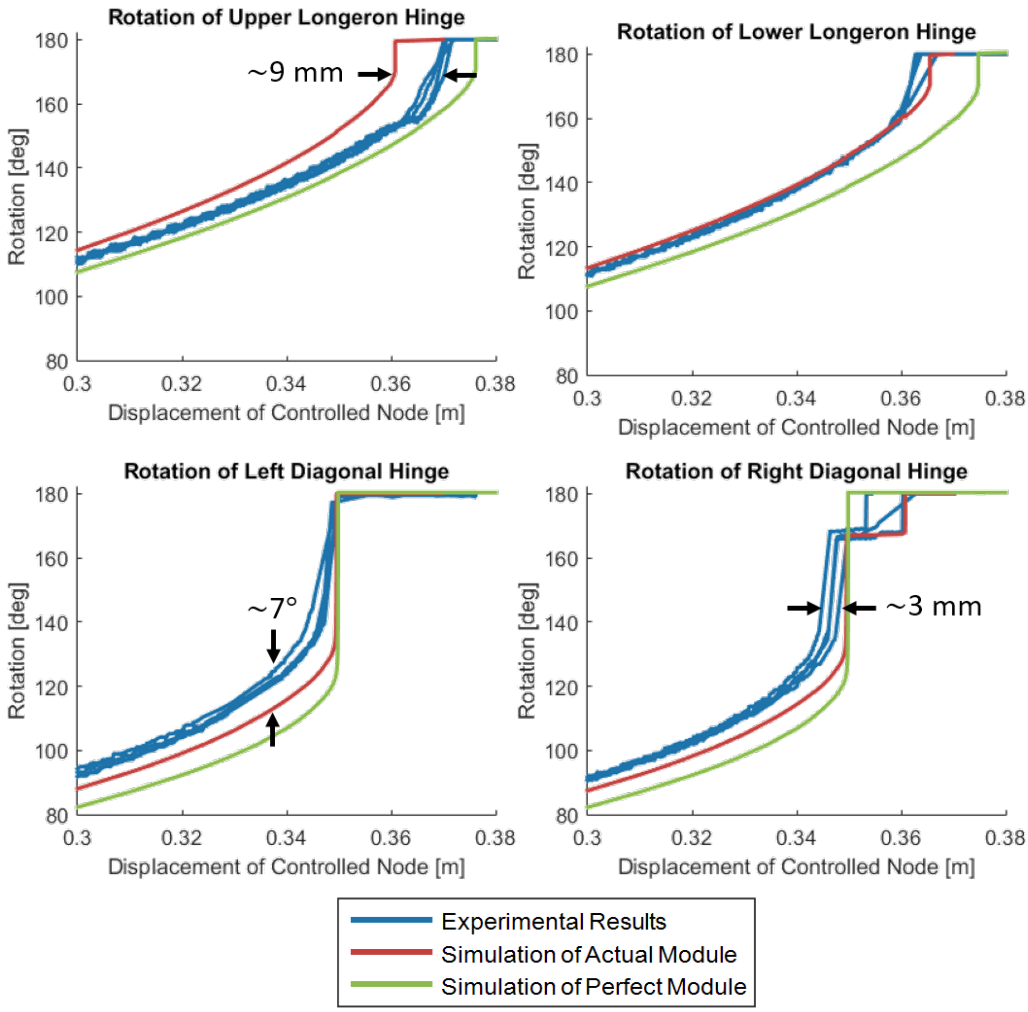

Figure 4.22: Rotations of each hinge, as measured in all four tests and as predicted in the two simulations. The rotations are plotted against the displacement of the controlled node, as measured by the stereo camera pair.

the experimental displacement of the tracked node in any direction to within 4.1%. For the perfect module simulation, this discrepancy was 9.4%. Thus, applying the FaroArm measurements to the simulation model reduced the discrepancy by more than half.

4.9 Chapter Conclusions

In this chapter, the experiments performed to validate the deployment simulation were described. The experimental results were compared to two simulations: one with the shape of the experimental module with fabrication errors accurately reproduced, and one with just the nominal shape. The results of the comparison showed firstly that the two simulations produced different deployment behavior, demonstrat-

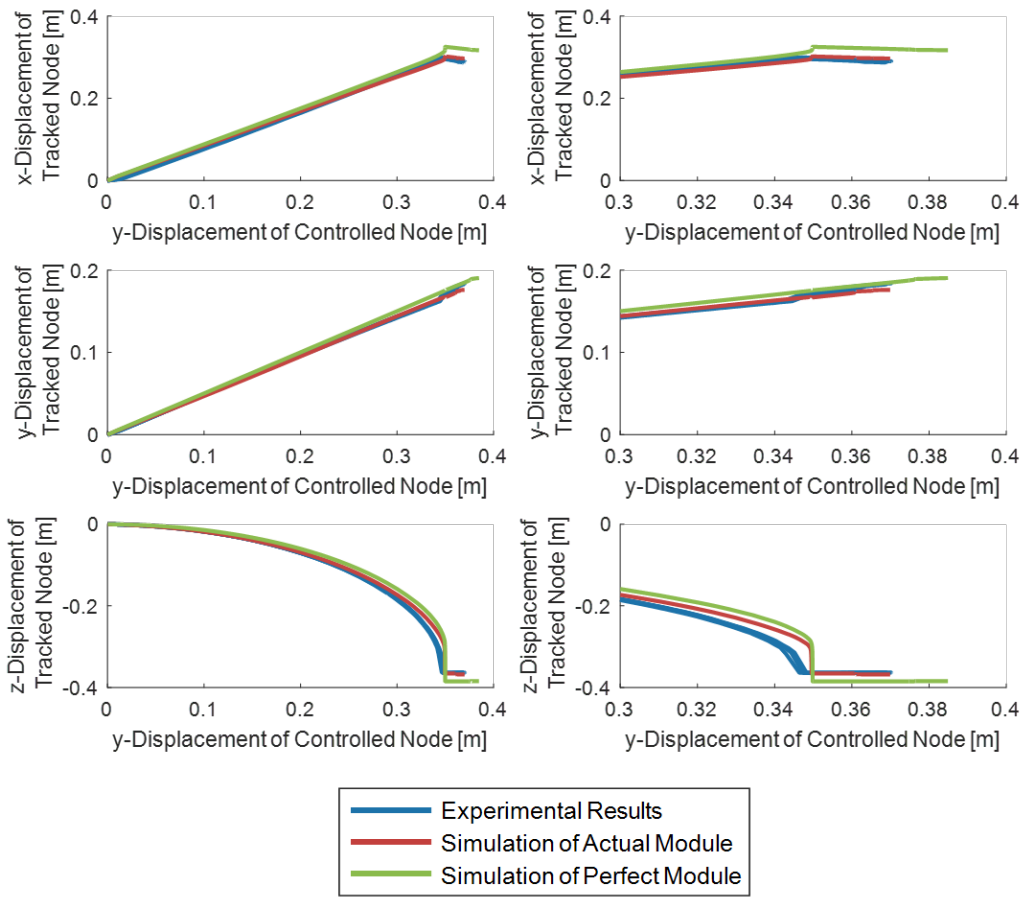

Figure 4.23: (Left) From top to bottom, the displacement of marker 1 in x, y, and z as measured by the stereo camera pair, plotted against the displacement of marker 2, or the controlled node. (Right) Identical to the left plot, except the x axis range has been narrowed to focus on the end of the deployment.

ing that small errors in geometry do have an effect. Secondly, the simulation of the experimental module did accurately predict the experimental results, with one notable discrepancy in the order of latching. This discrepancy may be due to a number of factors, including:

- errors in the shape measurements while using the FaroArm, caused by the structure moving slightly when touched with the arm,
- errors in the estimated compliance properties,
- differences in the moment-rotation curves among the Rolamite hinges,
- oversimplified model of the joints,

- difference in boundary conditions due to loose connections at the load cells and improper alignments in the frame,
- and lack of friction in the simulated hinges.

Further work may attempt to improve this discrepancy. However, the primary objective of the deployment simulation is to determine whether or not a deployment has failed. In this respect, the relative timing of the hinges is inconsequential. A potentially jammed hinge, however, is an important result. The simulation accurately predicted the jamming behavior observed in experiments. Another important result may be the final shape and precision of the module. The simulation was able to predict the measured location of marker 1 at the end of the deployment to within 5%. Thus, the deployment simulation is assumed to sufficiently model deployment behavior and will be used to produce reliability trade studies for the full ISTAR truss module in Chapter 5.

Chapter 5

RELIABILITY TRADE STUDIES

The previous two chapters discussed the development and experimental validation of the reliability estimation toolkit. The toolkit's generality to many deployable modules was emphasized. However, its primary purpose in this research is to estimate the deployment reliability of the ISTAR truss module. In the event of a deployment failure, there are two recovery options possible with the ISTAR architecture. Either the robot must have enough complexity and mobility to identify and correct the cause of the failure (e.g. a jammed Rolamite hinge), or the failed module is abandoned and additional back-up modules must be launched. Thus, the potential for failed deployments requires either significant additional complexity in the robot design or wasted launch mass, and thus the number of failures must be minimized and the deployment reliability maximized. To do this, two critical questions should be answered:

- Which type of fabrication error is most detrimental to reliability?
- How do the truss module design parameters affect reliability?

The answer to the first question informs the required tolerances of the manufacturing process and determines what part of the module must be manufactured most precisely. The answer to the second question informs the design process and how the truss module can be optimized to maximize reliability.

In this chapter, the design of the ISTAR truss module is first presented in sufficient detail to be accurately modeled by the toolkit. Then, the specific criteria for deployment failure are stated, specifying how reliability is defined in this research. Using this criteria, the toolkit is used to first estimate the reliability of the truss module as designed, identifying the effects of the different error types individually. Then, a set of potentially relevant design parameters are identified. Each design parameter is varied independently to establish its effect on reliability. Based on these results, improvements to the truss module design and reasonable manufacturing tolerances are suggested.

5.1 Detailed ISTAR Truss Module Design

Some basic dimensions of the ISTAR truss module were chosen in Chapter 2. However, in order to build the simulation model as described in Chapter 3 and accurately predict the deployment reliability, a more detailed design is required. Table 5.1 gives a comprehensive list of all the parameters required to fully define the truss module. Refer to Section 3.1 for a more detailed description of each parameter. The values marked with an asterisk were set in Chapter 2 and are reiterated here. The methods and justification for choosing each of the remaining variables is the subject of this section. Note that some of these parameters will be adjusted based on their effect on reliability; what is given here is only an initial design. A CAD model of this design is shown in Figure 5.1.

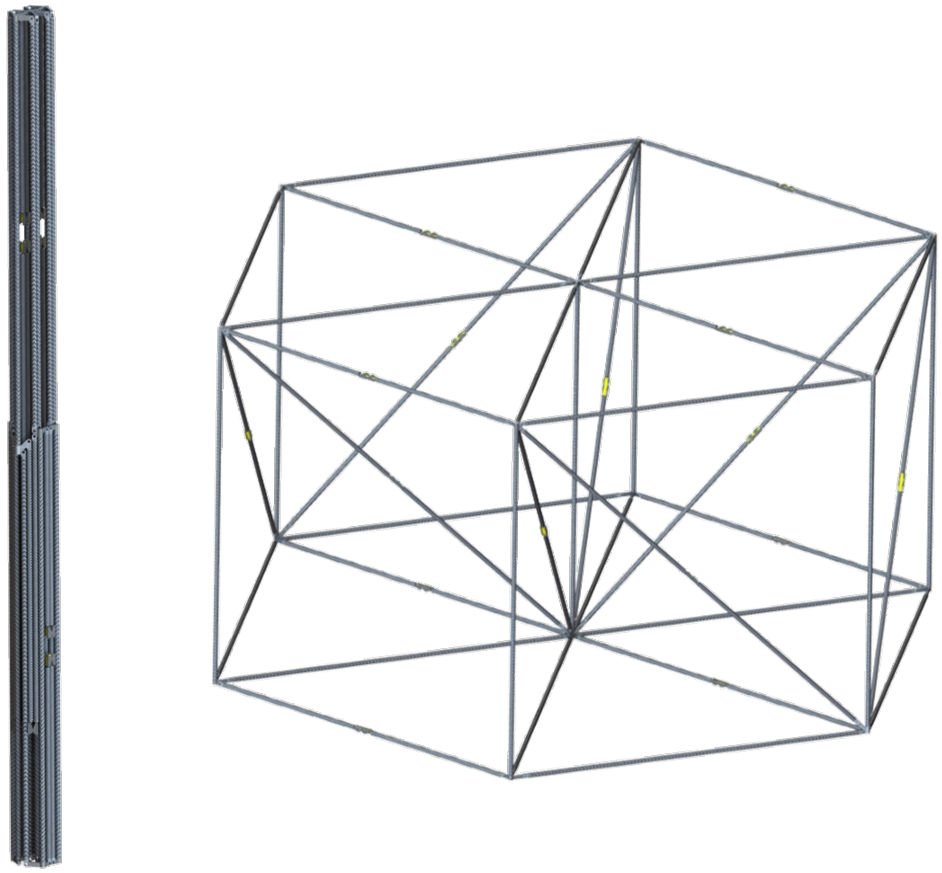

Figure 5.1: The ISTAR Truss Module Design shown stowed (left) and deployed (right).

	Truss Geometry	
L	Deployed side length	2.76 m*
H	Depth	2.76 m*
q	Folded side length	140 mm
l_j	Joint offset	35 mm
μ	Distance between folding member center lines when stowed	35 mm
	Member Cross Section and Material Properties	
d_o	Member outer diameter	35 mm*
t	Member wall thickness	3 mm*
E_m	Member material elastic modulus	340 GPa*
ν_m	Member material Poisson's ratio	0.3*
ρ_m	Member material density	1620 kg/m^2*
	Joint Cross Section and Material Properties	
a_j	Width of rectangular joint cross section	15 mm
b_j	Height of rectangular joint cross section	30 mm
E_j	Joint material elastic modulus	70 GPa
ν_j	Joint material Poisson's ratio	0.33
ρ_j	Joint material density	2700 kg/m^2
	Compliance Properties	
δ_{stop}	Compliance/slack threshold	750 μm
k_{low}	Compliance/slack stiffness	10^4 N/m
k_{high}	Wall stiffness	10^6 N/m
θ_{stop}	Rotation overextension threshold	2°

Table 5.1: ISTAR truss module properties. The values marked with an asterisk were set in Chapter 2 and are reiterated here.

The folded side length, joint offset, and folded distance between the center lines of the members attached to the Rolamite hinges are the minimum allowable, so that the module can be folded as compactly as possible, with all members completely vertical and tangent to each other where applicable. As discussed in Section 3.1, the minimum values of q, l_j, and μ are $4d_o$, d_o, and d_o respectively. The Rolamite hinges are assumed to use the same tape section and material as those of the experimental wedge module described in Section 4.2. However, μ in the experimental module was only 26 mm, less than the minimum of 35 mm set by d_o. Thus, all cam dimensions have been scaled from the experimental design by a factor 35/26.

The analytical equations in Section 3.1 state that the minimum deployment moment is only a function of the tape cross section and material. Similarly, the maximum latching moment is generally governed by the tape cross section and material and only a weak function of the cam dimensions. Indeed, the values of the minimum deployment moment and maximum latching moment for the ISTAR hinges

are 0.065 Nm and 11.96 Nm respectively, mostly unchanged from the experimental hinge values given in Section 4.2. Thus, it can also be assumed that the critical angle is unchanged from the value of 176.5°. However, the deviations from the minimum deployment moment shown in Section 4.5 are known to be dependent on the detailed cam geometry. Thus, the full moment-rotation curve of the experimental hinges generally cannot be applied to the ISTAR hinges with different cam dimensions. Rather than build a hinge with the ISTAR dimensions and repeat the moment-rotation experiment, the deployment moment is conservatively assumed to remain constant at the minimum analytical value of 0.065 Nm.

The joint material is assumed to be aluminum, though future iterations may instead use titanium for improved stiffness if mass constraints allow. The joint design was selected after reviewing a number of joint designs for similar structures [63][64][65][54][23]. Figure 5.2 shows a detailed view of a joint, with cross-section dimensions a_j and b_j.

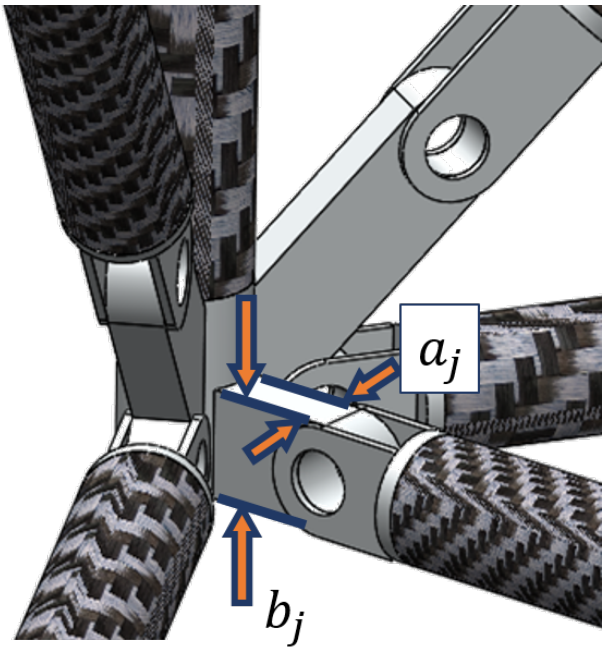

Figure 5.2: Illustration of a joint with rectangular cross-section in the ISTAR truss module.

The compliance properties are assumed to be the same as those of the experimental wedge module described in Section 4.1.

Initially, the robot is assumed to hold the centers of the two opposing verticals connected to the interior folding longeron face, as shown in Figure 5.3. The geometry

of this face is emphasized in Figure 5.4. As with the wedge model, moving these two verticals apart in the direction perpendicular to their axis is sufficient to deploy the module. The robot applies a constant velocity of 1 m/s in the y direction to the two nodes shown with circles in Figure 5.3, until the reaction forces in these nodes reaches a threshold of 5 N in tension. At that point, the control stops and the simulation continues for a short time to allow the model to equilibrate. The stabilization factor is set to 5.5×10^{-7}, with an initial and maximum time step of .05 s and a total simulation time of 5 s.

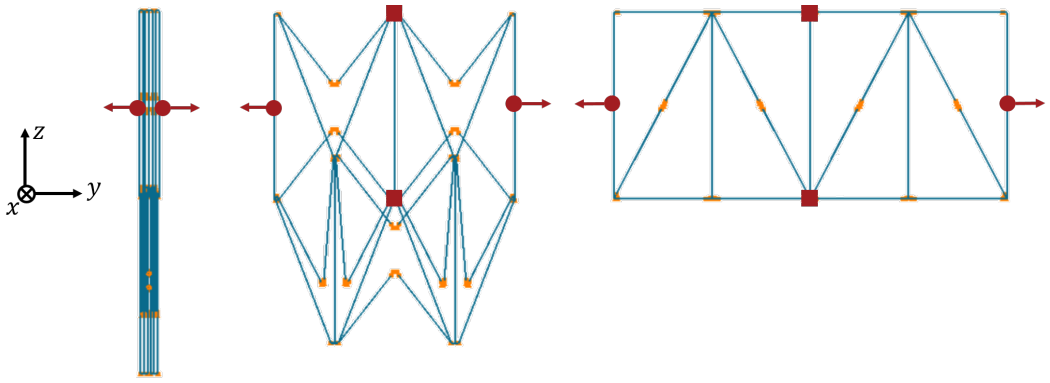

Figure 5.3: The boundary conditions applied to the deployment simulation of the ISTAR truss module. The two nodes marked with squares are fixed in space, while the two nodes marked with circles are moved apart until the reaction force in those nodes reaches a certain tolerance.

5.2 Failure Criteria

Again, reliability is estimated as the number of modules, each with a unique set of errors, that deploy without failure. In this research, a deployment has failed if any one of the Rolamite hinges has not latched or the reaction forces at the controlled nodes have exceeded 500 N in any direction. A typical example of a latching failure is shown in Figure 5.5. In practice, this is the only failure mode for all studies presented in this chapter. The reaction forces required to constrain the Rolamite hinges are small, because the hinge moments are benign (12 Nm maximum). Even with errors, these reaction forces do not increase substantially during deployment. However, large force spikes do occasionally occur just after control stops and the robot begins simply holding the controlled nodes in place. Some Rolamite hinges may continue to latch, pushing the nodes outward against the robot and causing large reaction forces. Even if these forces exceed the limit, this is not considered a

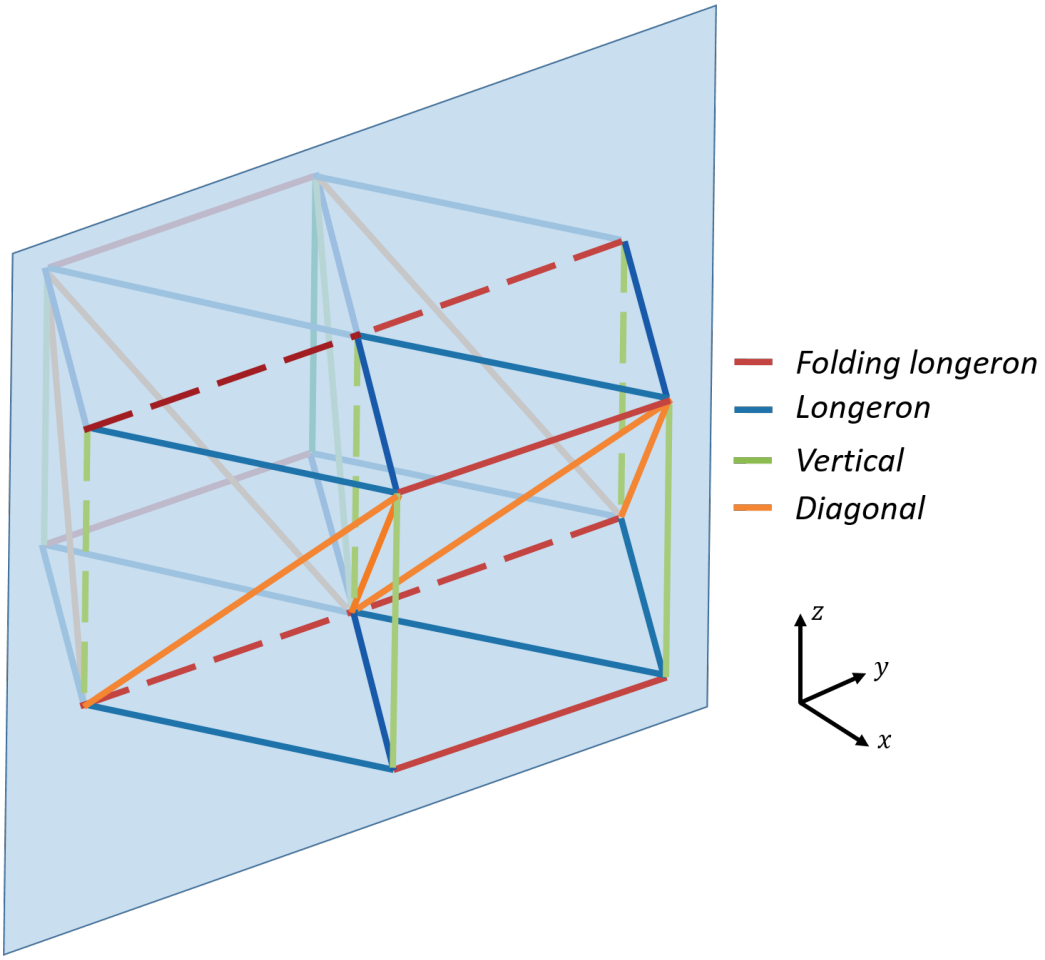

Figure 5.4: Diagram of the deployed wedge model emphasizing the folding longeron face, shown with dashed lines. This face does not have any diagonals. During deployment, the three verticals in this face only move apart in the y direction relative to each other.

failure, since deployment control has already completed; in the actual mission, the robot would be allowed to move to accommodate these forces.

As discussed in Section 2.3, rigid body actuators can account for errors up to 10 mm on the top surface of the truss, much smaller than the errors that are considered in these deployment studies. Thus, the precision requirement is not included in the deployment failure criteria. However, for the assembly process, it is necessary to know the magnitudes of errors that may be present after deployment. This investigation will be briefly discussed in Section 5.11.

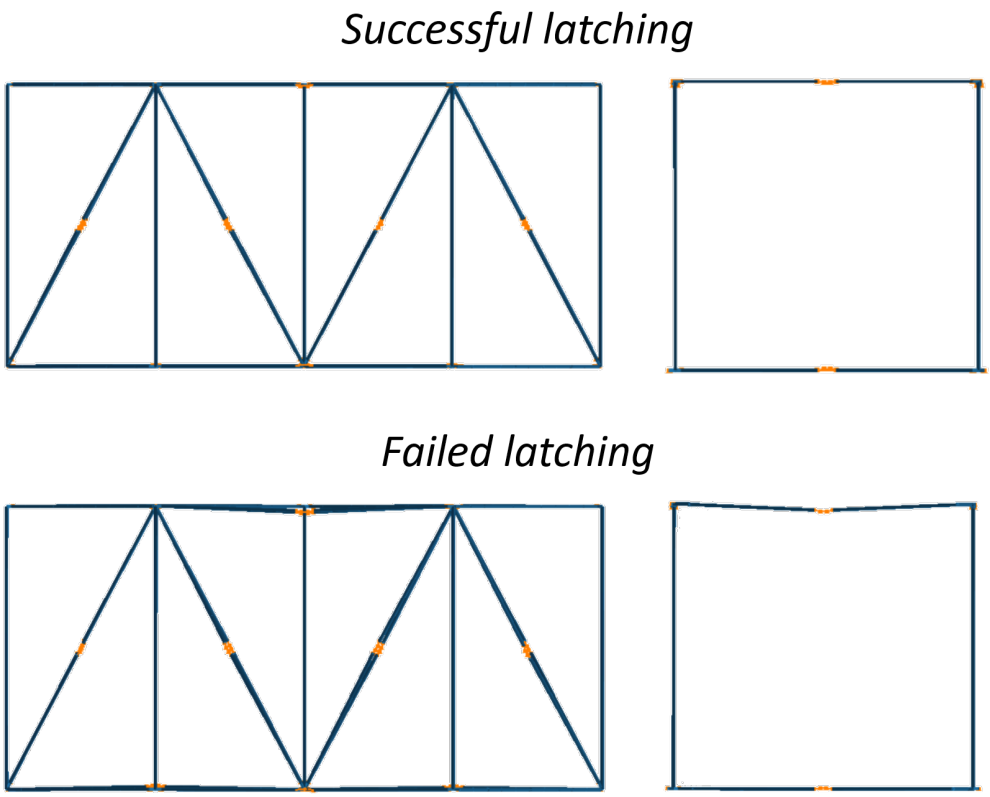

Figure 5.5: (Upper) Example of a deployed module with all hinges successfully latched. One longeron face is shown for detail. (Lower) Example of a deployed module with some hinges unlatched. One longeron face is shown to contrast the unlatched upper hinge from the latched lower hinge.

5.3 Reliability of ISTAR Design and Effect of Error Type

The first step in this research is to estimate the reliability of the above truss module design with fabrication errors. As explained in Section 3.1, the three types of errors are member length errors, member alignment errors, and hinge axis errors. In a single deployment simulation, the error applied to a relevant location in the model is randomly drawn from a uniform distribution. The bounds of the distributions are $\pm dL_{max}$ for member length errors, $\pm dP_{max}$ for member alignment errors, and $\pm d\theta_{max}$ for axis errors. A uniform distribution is used over a normal distribution, since tolerances are often quoted with guaranteed definitive bounds, rather than means and standard deviations. Uniform distributions have also yielded more realistic results in previous literature [42]. Furthermore, in the FaroArm measurements of the experimental module described in Section 4.7, most errors were close to 0, but large outlying errors were measured that may not be captured in a normal distribution. Still, the effect of using a normal distribution will be

discussed briefly in Section 5.4.

The individual effect of length errors on reliability was first investigated by setting dP_{max} and $d\theta_{max}$ to 0 and varying dL_{max}. For each value of dL_{max} tested, the deployment simulation was run for n = 50 trials, meaning that 50 models with unique random error distributions were deployed. The number of successes out of 50, or the estimated reliability, was recorded, and the results are given in Figure 5.6. The error bars on the plot are the binomial 95% confidence interval on the proportion, defined by the Clopper-Pearson method [66]. Unless otherwise stated, all quoted confidence intervals and error bars use this method. The plot shows that, for length errors less than 1 mm (dL_{max} = 1 mm), the deployment is expected to be 100% reliable. The same process was repeated for member alignment errors and axis errors, and the results are given in Figure 5.7 and Figure 5.8 respectively. Reliability estimates of nearly 100% were achieved for member misalignment errors less than 1 mm and for hinge axis errors less than 1°.

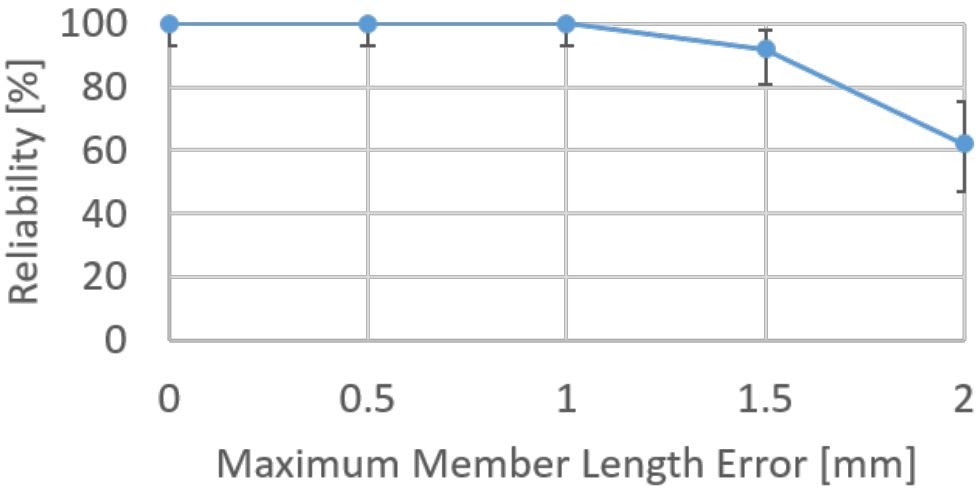

Figure 5.6: Reliability vs. maximum length error (dL_{max}).

The above results yield tolerances for nearly 100% reliability for each error type. Comparing the relative difficulty of achieving these tolerances gives insight into which error is most detrimental for reliability and what needs to be manufactured most precisely. Rods can routinely be cut to within 0.1 mm, so the 1 mm tolerance on length errors should be easily obtained. Member alignment errors are most likely caused by the members not being straight. Commercial rods can achieve a quoted straightness of 0.25 mm over 1.5 m; assuming that it extends linearly to the

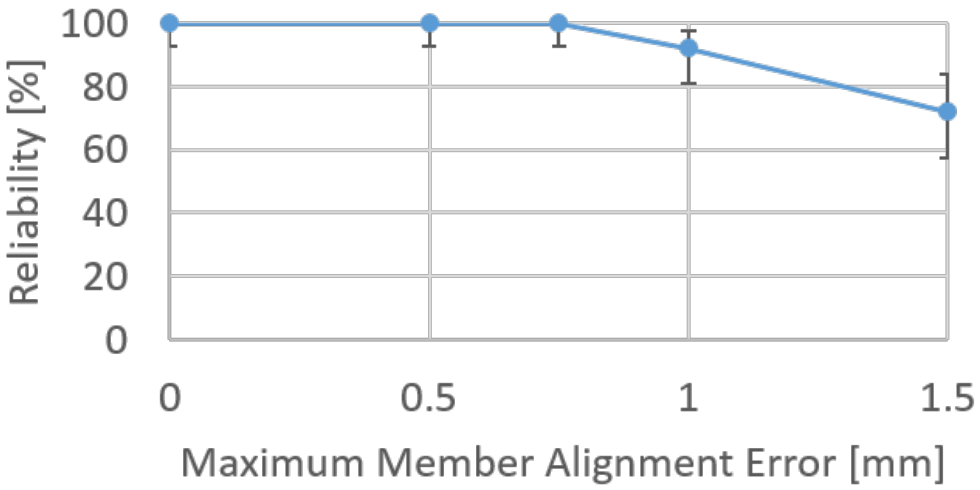

Figure 5.7: Reliability vs. maximum member misalignment (dP_{max}).

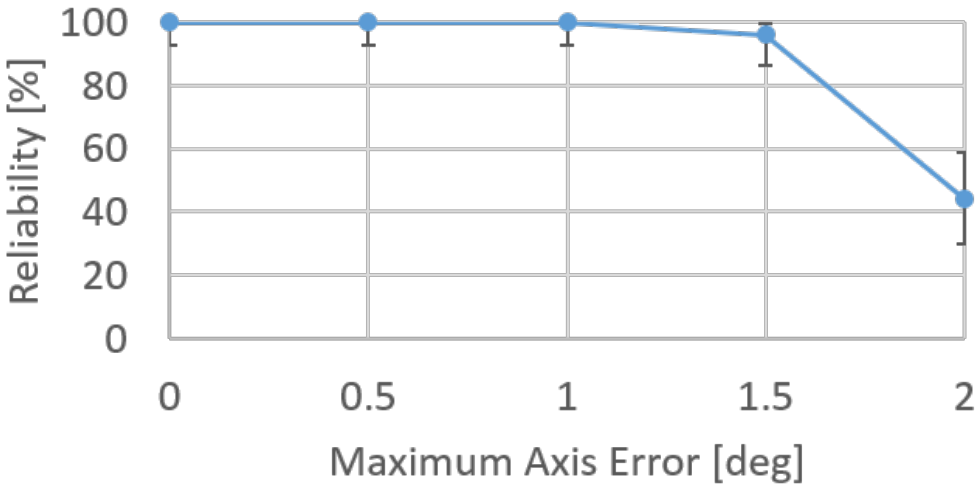

Figure 5.8: Reliability vs. maximum hinge axis error ($d\theta_{max}$).

maximum length in the ISTAR truss module of about 3.9 m (a diagonal member), this yields a straightness of 0.65 mm, within the 1 mm tolerance [67]. An axis error in a pinned hinge may be caused by offsets in the positions of the holes that hold the pin. A tolerance of 1° for the pinned hinges across the 15 mm joint implies a tolerance of 0.26 mm in the relative position of the holes. A standard CNC tolerance is 0.1 mm, so 0.26 mm should be achievable. Alignment errors in the Rolamite hinges may be caused by a relative twist in the cam sets introduced by a tension difference in the two wires. For the experimental module described in Section 4.7,

the plane of each cam set was measured with the FaroArm for the four Rolamite hinges. It was found that the normals of these planes, or the hinge axes, differed from the nominal design by up to 5°. Certainly, the hinges were not carefully manufactured for the experiment and the twist can be greatly reduced by simply measuring and controlling the tension in the wires. However, a tolerance of 1° may be still be difficult to achieve. Thus, the hinge axis error is the most detrimental to the reliability, and the focus of the manufacturing efforts should be on the Rolamite hinges.

In the actual module, all three error types may be present. The deployment simulation was run 100 times with the bounds dL_{max} = 1 mm, dP_{max} = 1 mm, and $d\theta_{max}$ = 1°. The resulting reliability was estimated to be only 77% (between 67% and 85% within 95% confidence). This is a sharp decrease from the reliability estimates for any single error type, suggesting that the error types are not independent in their effect on the deployment behavior. A reliability of 77% is unacceptably low; however, as just discussed, these bounds are unnecessarily high given standard manufacturing capabilities. The remainder of this chapter presents the effect of various design parameters on reliability. In each investigation, these error bounds were applied, providing a low reliability baseline that allows for significant improvements. Keeping all other design parameters nominal, one selected parameter was varied and the reliability for each value was estimated after 50 trials. In many of the investigations, some tested values were not feasible or within mission requirements. The range of values was simply chosen to clearly show any effect on reliability.

5.4 Effect of Distribution Choice

As previously mentioned, a uniform error distribution was chosen for the ISTAR module over a normal distribution, because it is easily derived from commonly quoted tolerances, has been demonstrated to be more realistic in literature, and more closely represents the experimental module measurements. However, depending on the manufacturing process, a normal distribution may be more applicable for other missions. To investigate the effect of the choice of distribution on reliability, a normal distribution of errors was instead applied to the model. Each of the three error types were drawn from normal distributions with means of 0 and standard deviations equal to half the equivalent uniform distribution bound, so that approximately 95% of the errors would be less than that bound. For instance, the member length errors were drawn from a distribution with mean of 0 and a standard deviation of 0.5 mm. As expected, this significantly increased the reliability to >93% after 100 trials,

since the individual errors tended to be closer to 0 than in a uniform distribution. Next, the standard deviation for each error type was set to twice the equivalent uniform distribution bound, such that only approximately 68% of individual errors would be less than that bound. As expected, the reliability was drastically reduced to 50%±14.5% after 50 trials. This suggests that the reliability resulting from a uniform error distribution with bound $\pm\sigma$ is between the reliability values resulting from normal error distributions with standard deviations σ and $\sigma/2$. Which distribution is more realistic and which bounding values to use again depend on the specifications from the manufacturer and the type of manufacturing process. However, it can be said that the uniform distribution yields intermediate reliability values and thus can be used as a good benchmark for any distribution choice.

5.5 Effect of Hinge Moment

Intuitively, increasing the deployment moment of the Rolamite hinges would decrease their sensitivity to errors and facilitate latching, therefore increasing reliability. Higher moments can be achieved by simply stacking additional tape sections together on both sides of the hinge; the moment is then proportional to the total number of tape sections, according to the equations given in Section 3.1. To test this hypothesis, the hinge moment in the simulation model was multiplied by factors of 2, 4, and 6, equivalent to having 2, 3, and 4 tape pairs respectively. The results, plotted in Figure 5.9, suggest that an increase in moment does have a significant positive effect on reliability, and that a reliability greater than 98% may be achieved with just three tape pairs total.

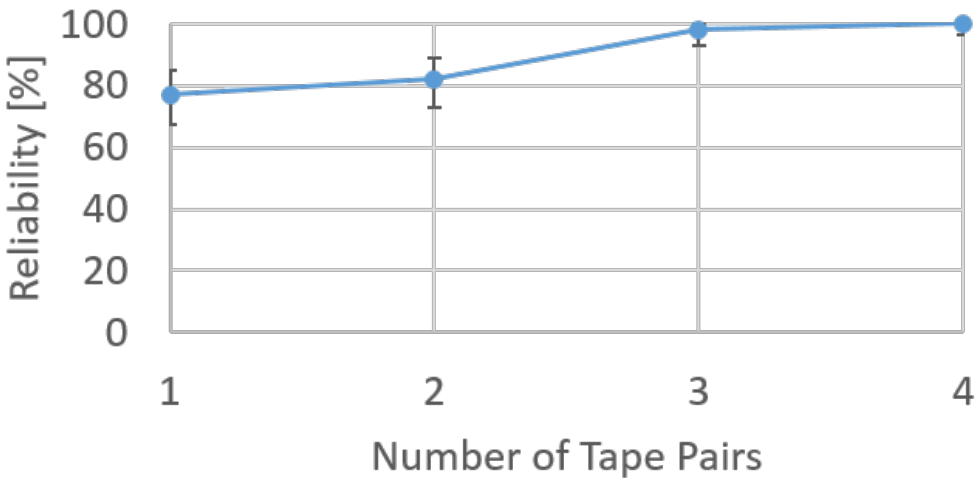

Figure 5.9: Reliability vs. number of tape section pairs.

5.6 Effect of Joint Stiffness

It was hypothesized that stiffer joints, or joints with larger cross-sections, would prevent the structure from accommodating errors, leading to higher stresses and lower reliability. This hypothesis was tested by multiplying the nominal values of a_j and b_j by the same factor. The results, plotted in Figure 5.10, suggest that in fact the joint cross-section has no statistically significant effect on the reliability for this structure.

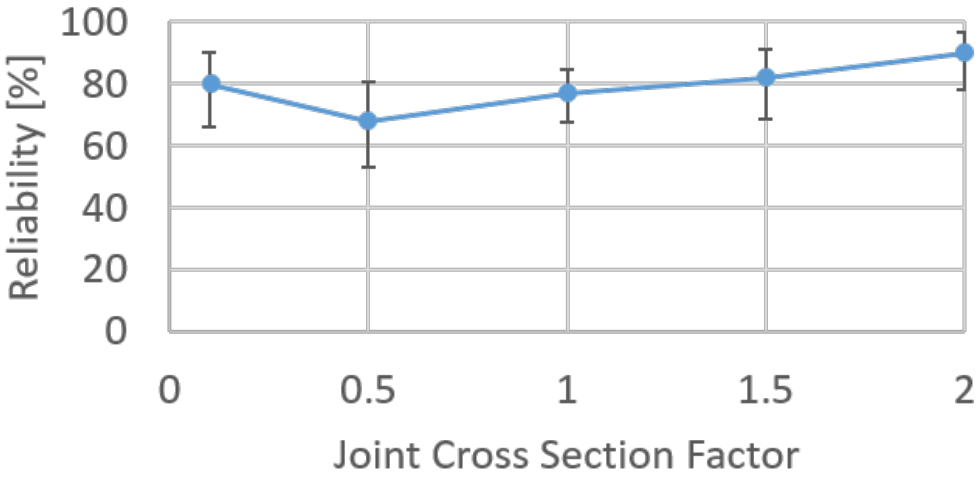

Figure 5.10: Reliability vs. joint cross-section factor multiplying the width a_j and height b_j.

5.7 Effect of Member Properties

The member wall thickness determines the stiffness and mass of the members. As with the joints, it was hypothesized that stiffer members may lower reliability. However, Figure 5.11 shows that, for the majority of the range tested, the reliability is statistically unaffected by the wall thickness, with very thin members possibly leading to lower reliability.

The member outer diameter affects not only the stiffness and mass of the members, but also the length of the hinge offsets, the folded side length, and thus the entire geometry of the structure. The effect of diameter on the reliability is plotted in Figure 5.12. The results show that reliability sharply decreased for diameters larger than 5 cm, with no successful deployments achieved with a diameter of 10 cm.

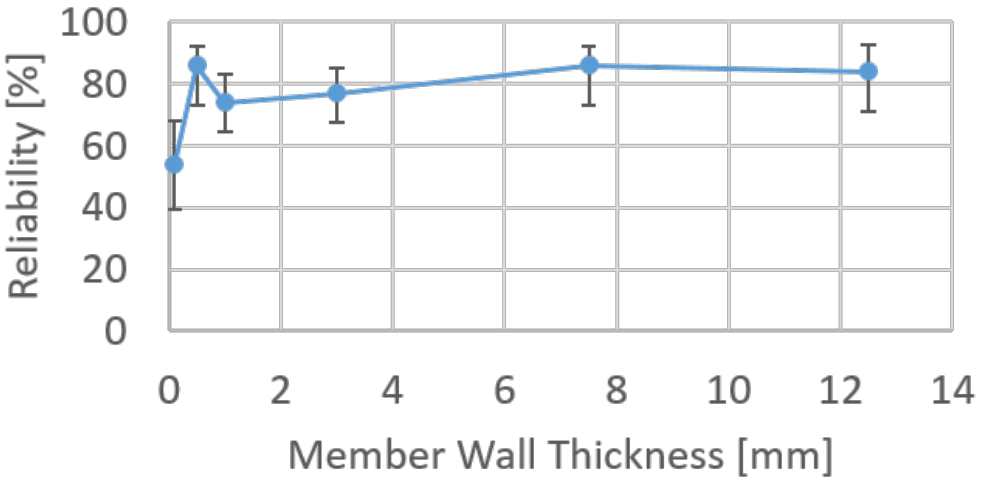

Figure 5.11: Reliability vs. member wall thickness.

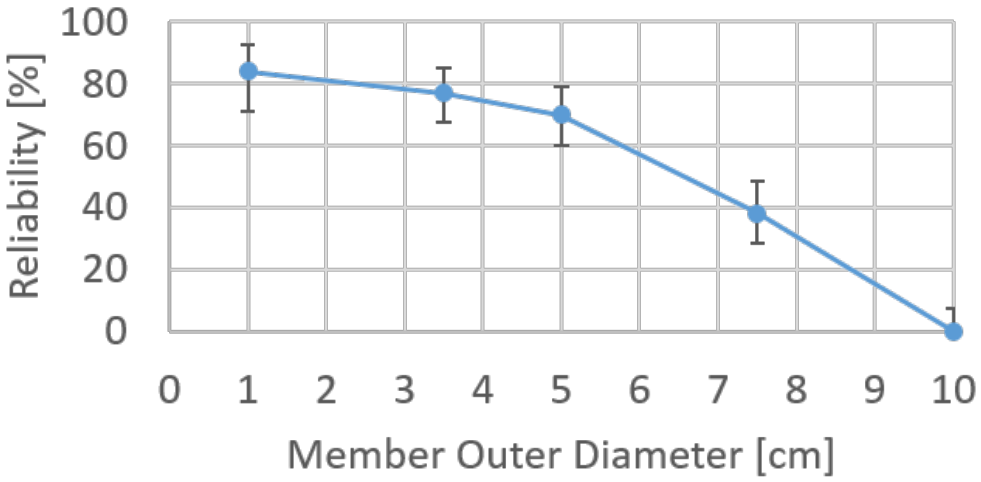

Figure 5.12: Reliability vs. member outer diameter.

5.8 Effect of Compliance Properties

Without any compliance, the structure would not be able to accommodate any errors without stressing the members. Thus, reliability was expected to be a strong function of the compliance. As described in Section 3.1, the compliance is defined by the threshold δ_{stop}, which separates a region of low stiffness k_{low} from high stiffness k_{high}. In the initial design, the value of k_{low} is not directly specified; rather, the force at the threshold is set to 25 N. For this investigation, δ_{stop} was varied while keeping the force at the threshold constant, such that k_{low} also varied proportionally. The results, plotted in 5.13, support the hypothesis, showing that reliability increases

as the compliance threshold increases.

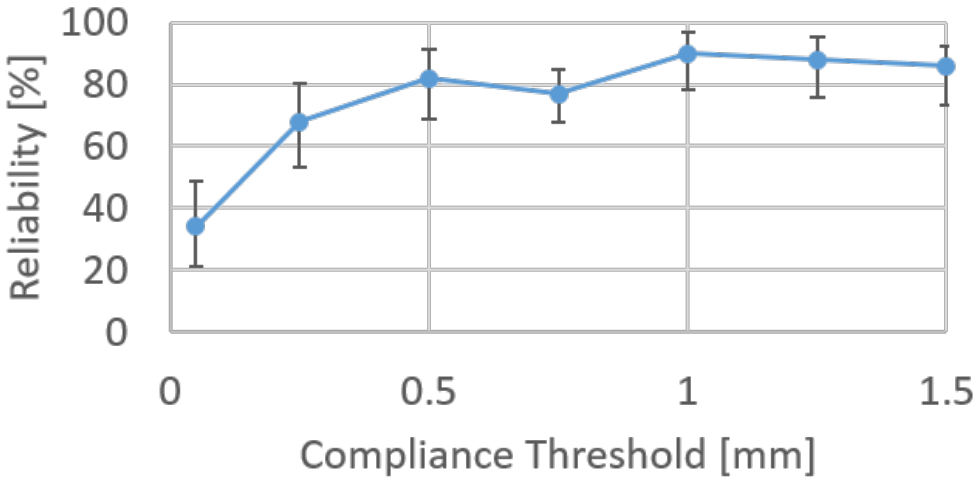

Figure 5.13: Reliability vs. compliance threshold.

5.9 Effect of Module Depth

In the initial design, the ratio of the module depth H to the side length L is set to 1. This decision was made to not only satisfy the precision requirements as outlined in Section 2.5, but also to avoid eccentricities during the deployment that were assumed to reduce reliability. The ratio of H/L was varied from 0.25 (H = 0.69 m) to 2 (H = 5.52 m), and the reliability values are plotted in Figure 5.14. The results show that very low truss depths lead to very low reliability, but for ratios greater than 1, the reliability is statistically unaffected.

5.10 Effect of Control Location

Nominally, the controlled nodes are located at the midpoints of the two vertical members, as shown in Figure 5.3, rather than the top or bottom. It was hypothesized that controlling the deployment from different points along the vertical members would lead to eccentricities that raise stresses and lower reliability. Yet, no statistical difference in reliability was found between controlling the midpoints, tops, or bottoms of the two vertical members. However, the spike in reaction forces at the end of the deployment significantly increased when the tops or bottoms were controlled, reaching up to 16 kN in some trials. Again, these spikes were not officially included in the failure criteria, because the robot can move after deployment to mitigate residual forces, but even the potential for such large reaction forces may

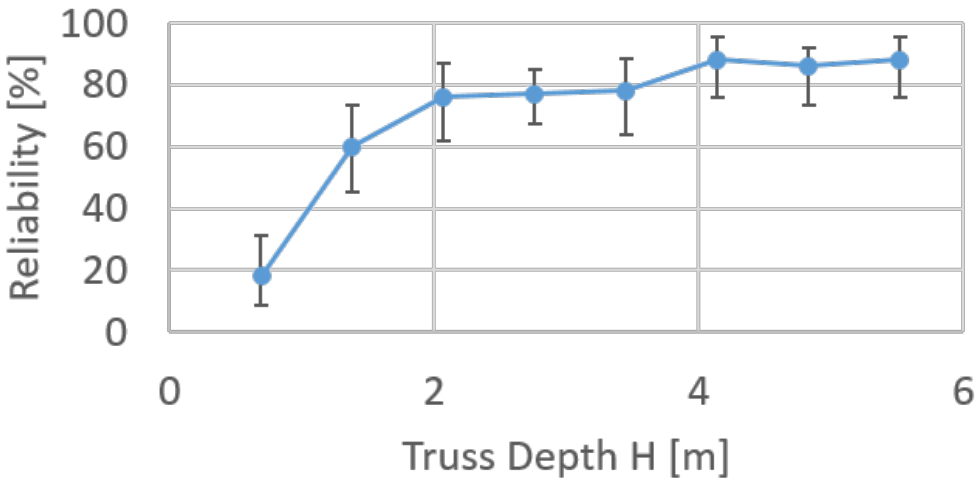

Figure 5.14: Reliability vs. truss depth.

be undesirable for the control system. Thus, controlling from the midpoints is still considered more reliable.

5.11 Chapter Conclusions

In this chapter, the deployment reliability of the ISTAR truss module with fabrication errors was investigated using the reliability estimation toolkit. The trade studies found that reliability is most strongly affected by the hinge moment, compliance threshold, member outer diameter, and module depth. The member outer diameter and module depth were previously chosen in Section 2.5 to satisfy mass and precision requirements, and thus changes to these parameters may have significant effects on the structure beyond reliability. While increasing compliance also increases reliability, it may weaken the structure's ability to carry loads. High reliability can still be achieved with the same diameter, depth, and compliance by simply adding two more tape pairs (three total) to each Rolamite hinge, a design change that has minimal impact on the mission as a whole.

All of the trade studies were performed using the error bounds dL_{max} = 1 mm, dP_{max} = 1 mm, and $d\theta_{max}$ = 1°. Individually, these bounds resulted in reliability values close to 100% for the initial design. These results suggested that hinge axis errors, particularly in the Rolamite hinges, are the most detrimental error type to reliability, in that the tolerance required for nearly 100% would be the most difficult to achieve. The member length and alignment tolerances were actually unnecessarily high given standard machining practices. However, combining the

errors compounded their effect on the reliability, reducing it to only 77%. While unacceptable for the final design, this initial reference point was low enough to clearly see improvements in the trade studies.

Given the results presented in this chapter, for the final ISTAR truss module design, the Rolamite hinge moments should be increased by a factor of 4. The manufacturing tolerance on the member length and alignment should be set to 0.5 mm, within the conceivable range of ordinary manufacturing processes and commercially available parts. The hinge axis tolerance should be defined separately for the Rolamite hinges and pinned hinges: set to 2.5° and 1° respectively. The Rolamite hinge axis is a more relaxed tolerance than initially employed, but may still require careful construction, particularly to avoid twisting the cam sections by unevenly tensioning the wires. With these parameters and all others unchanged from the initial design presented in this chapter, the toolkit predicts a reliability of >96.3% after 100 trials.

For each of the 100 trials performed to obtain the above reliability estimate, the final positions of the major nodes (center vertices of the top and bottom hexagon face) were recorded and compared to the nominal positions. Recall from the experimental validation that these positions can be assumed accurate to within 5%. On average, the difference was 0.5 mm in any direction, with a maximum difference of up to 4.5 mm. This result suggests that, even though the applied member length and alignment errors are only 0.5 mm, they compound with hinge alignment errors to reduce the final precision by almost a factor of 10.

Chapter 6

ASSEMBLY ANALYSIS AND INTERCONNECT CONCEPT

As described in the introduction, the precise connection of many modules is likely the most difficult aspect of the ISTAR architecture. After deployment, each module has a certain set of geometric errors from its nominal shape due to imperfections introduced during fabrication. In Section 5.11, a set of manufacturing tolerances were proposed that yield the desired deployment reliability. With these tolerances, the *module errors*, or residual errors from the nominal shape after deployment, may be up to 4.5 mm in any direction. The *connection points* on any two adjacent modules have some nominal locations (distance and direction) with respect to each other, defined by the required inter-module gaps in the backplane. If module errors are present, the connection points will be misaligned. *Connection misalignments* are defined in this context as the initial distance of one connection point to its nominal position with respect to the other connection point before an actual connection is made. A connection misalignment is illustrated in Figure 6.1. The *interconnects*, or the mechanisms that make the physical connections between connection points, must have a sufficient capture range to accommodate connection misalignments. As an interconnect engages, the connection points may be forced into alignment, stressing the structure. Once all interconnects are fully engaged, the backplane will reach an equilibrium shape and stress state. The resulting stresses cannot exceed the strength of the member material, which is 1300 MPa axially and 50 MPa in shear [60]. The equilibrium shape of the backplane will have *surface errors*, defined as the out-of-plane distance of each major node (module vertex or center) on the top surface of the backplane to its nominal position. The maximum surface error, or the total *surface precision*, must not exceed 10 mm, as required by the wavefront control system described in Section 2.3. The following questions are thus posed in this research:

- What bounds on the module errors maintain safe stress levels in the backplane throughout the assembly process? What bounds on the module errors maintain the required surface precision of the completed backplane, and do the surface errors increase with the size of the backplane? Are the corresponding manufacturing tolerances more or less constraining than those required for

successful deployment?

- How do module errors contribute to connection misalignments? Given a module error distribution, do connection misalignments grow with the number of assembled modules? What is the maximum connection misalignment that can be expected at any given point in the assembly?
- What level of complexity is required of the interconnect design to accommodate the maximum expected connection misalignment?

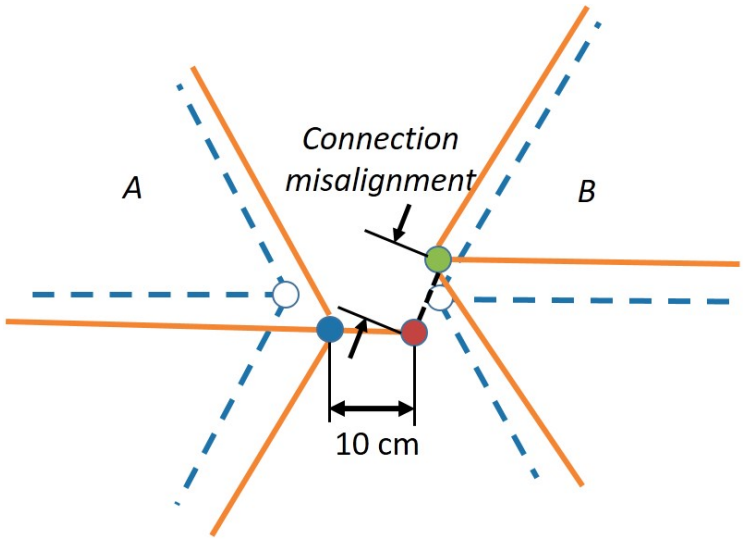

Figure 6.1: Illustration of a connection misalignment between two modules. The erred shapes of the modules are shown with solid orange lines, whereas the nominal shapes are shown with blue dashed lines. Assume that module A is already part of the structure, and module B is currently being assembled. If both modules were perfectly constructed, their connection points would be in the locations of the white circles. However, since errors are present, the connection point on module A is actually in the location of the blue circle. The red circle marks *the nominal location of connection point B with respect to the actual location of connection point A*, which is 10 cm from the blue circle along a line from the center of module A. The green circle marks the current location of connection point B. To engage the interconnects, the green circle will have to become coincident with the red circle. Thus the connection misalignment is defined as the distance between the green circle and the red circle.

In this chapter, the ISTAR architecture assembly plan is first outlined in greater detail, including the order of assembly and how many connections are required for each module. Then, a new Abaqus-based step-by-step assembly simulation method is described and used to answer the first two sets of questions. With this information,

a simple interconnect design is initially proposed and a detailed simulation model of one module with interconnects is developed. The model is used to determine if the simple interconnects can fully engage when the maximum expected connection misalignment is present, or if greater complexity in the design is required.

6.1 Step-by-step Assembly Simulation

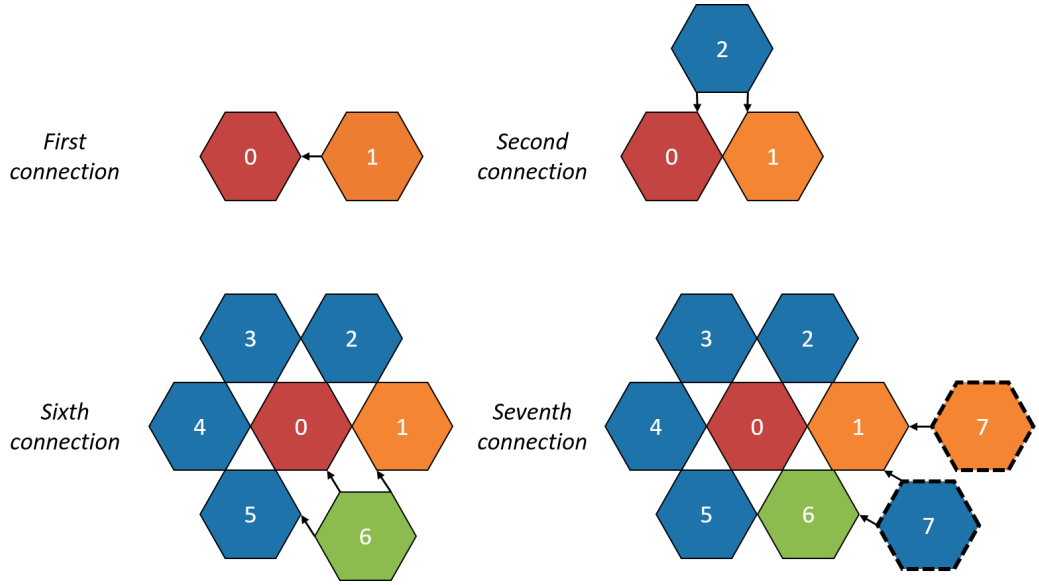

Figure 6.2: Assembly of the first ring of modules and the start of the second ring. The module in red is the hub. Modules in orange are connected along one edge when assembled. Modules in blue are connected along two edges, and in green along three edges. The first module in the second ring can either be connected along one edge or two.

Section 2.2 briefly outlined the assembly plan proposed in the ISTAR architecture. In this plan, the truss modules are assembled in rings around a central hub that is rigidly connected to the spacecraft driving the primary mirror. The hub is essentially a non-deployable version of the truss module. The modules are tiled edge-to-edge, rather than face-to-face, and connection points are located at the top and bottom of each edge vertical member. Thus, each edge connection between two modules involves four connection points (two per module), joined by two interconnects that are engaged simultaneously. Figure 6.2 illustrates the assembly of the first ring of modules. The first module is connected to the hub along one edge. Modules 2-5 are connected along two edges: one to the hub and one to the previous module. The final module in the ring must be connected along three edges, meaning six interconnects must engage simultaneously. The first module in the next ring can be connected to the previous ring along one edge or two. Since a connection along

a single edge provides minimal resistance to rotations about the horizontal plane, the two-edge connection is more desirable. A full map of connections is illustrated in Figure 6.3.

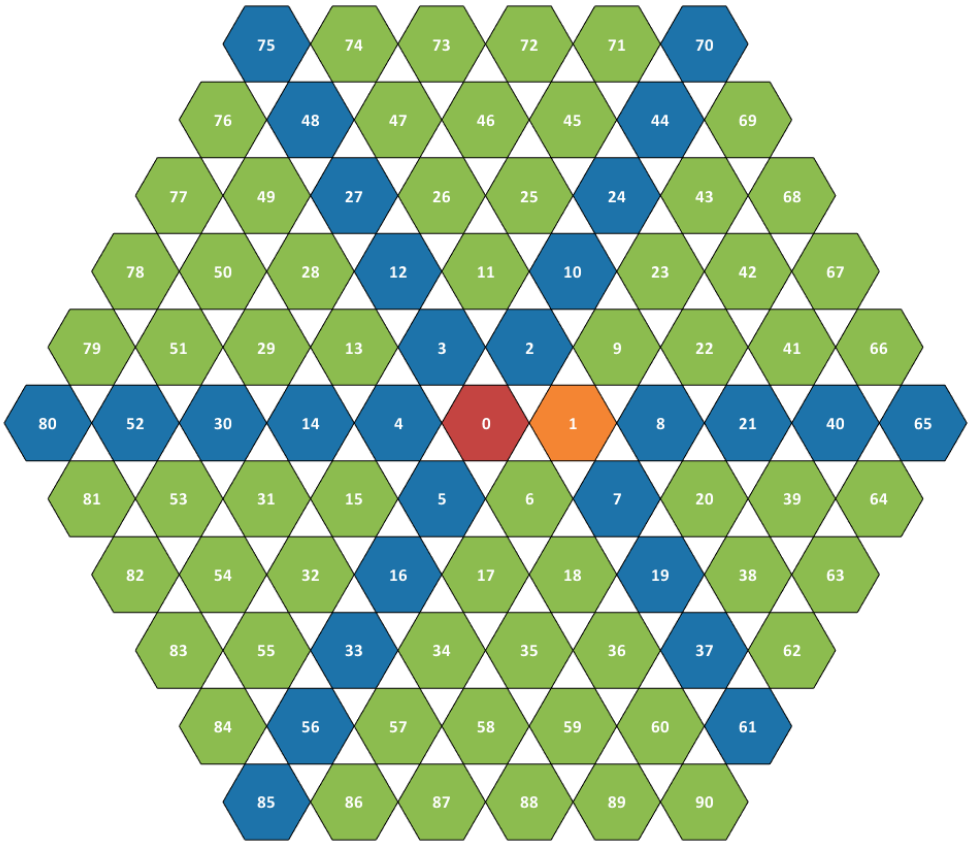

Figure 6.3: Map of assembly connections. The module in red is the hub. Modules in orange are connected along one edge when first assembled. Modules in blue are connected along two edges, and in green along three edges.

This basic assembly process is translated into a general simulation methodology as follows. In the first assembly step, two modules are placed in the model space, each with a unique set of module errors that result in connection misalignments. To mimic the interconnects engaging, the connection points along one edge of the second module are forced into alignment with those on the first module. The fully engaged interconnects are then added between the connection points to form the connection. This allows the stresses in the second module caused by the forced alignment to dissipate through the first module until the intermediate structure is in equilibrium. Then another module is added and the process is repeated until the

entire backplane is assembled.

6.1.1 Simple Example and Analytical Verification

In order to develop and illustrate the assembly process in Abaqus, a simpler example of assembling pin-jointed truss members in a 2D geometry is initially considered, as shown in Figure 6.4. In the initial model, the entire truss is created. Joining connectors, represented as orange lines, effectively merge nodes 2 and 4; 3, 6, and 9; 5, 7, and 10; and 8 and 12. The nominal locations of the nodes are set by the 1-m square geometry, but each node is randomly displaced in x and y by up to 1 cm, meaning that each truss element has some associated length error. The connected nodes are therefore not initially coincident, as illustrated, but exaggerated in the figure. In the first analysis step in Abaqus, all elements are removed except those shown using the "model change" tool. In the next analysis step, or the first alignment step, node 6 is then displaced to be exactly coincident with node 3, and node 4 is displaced to be exactly coincident with node 2. The truss elements connecting nodes 4 and 5 and nodes 5 and 6 become stressed as a result. However, there is no physical connection between nodes 3 and 6 and nodes 2 and 4, and so the other members remain unstressed. In the first equilibrium step, the connectors joining these nodes are reinstated, and the structure reaches an equilibrium stress state. In the second alignment step, nodes 7, 8, and 9 and associated truss elements are added back to the model. Node 9 is displaced to be exactly coincident with nodes 3 and 6, and node 7 is displaced to be exactly coincident with node 5. The truss elements connecting nodes 7 and 8 and nodes 8 and 9 become stressed as a result. All other truss elements remain in the same stress state that resulted from the first equilibrium step. In the second equilibrium step, the connectors joining these nodes are reinstated, and the structure reaches a new equilibrium stress state. Each subsequent alignment step adds a section of the truss and aligns the nodes to be connected, and each following equilibrium step adds a physical connection between those nodes and allows the structure to reach an equilibrium stress state.

All alignment and equilibrium steps are nonlinear, stabilized, static analysis steps in Abaqus. Much like the deployment simulation, the Abaqus input file for the entire simulation is written by a Python shell. Since each step is part of the same simulation, one input file must be written to describe every step. However, the coordinates of the nodes necessarily change throughout the simulation as the structure reaches equilibrium. These coordinates are thus unknown when the input file is written, and the displacements in any given alignment step cannot be prescribed directly.

Instead, they must be automatically computed by Abaqus during the simulation with the user subroutine UAMP.

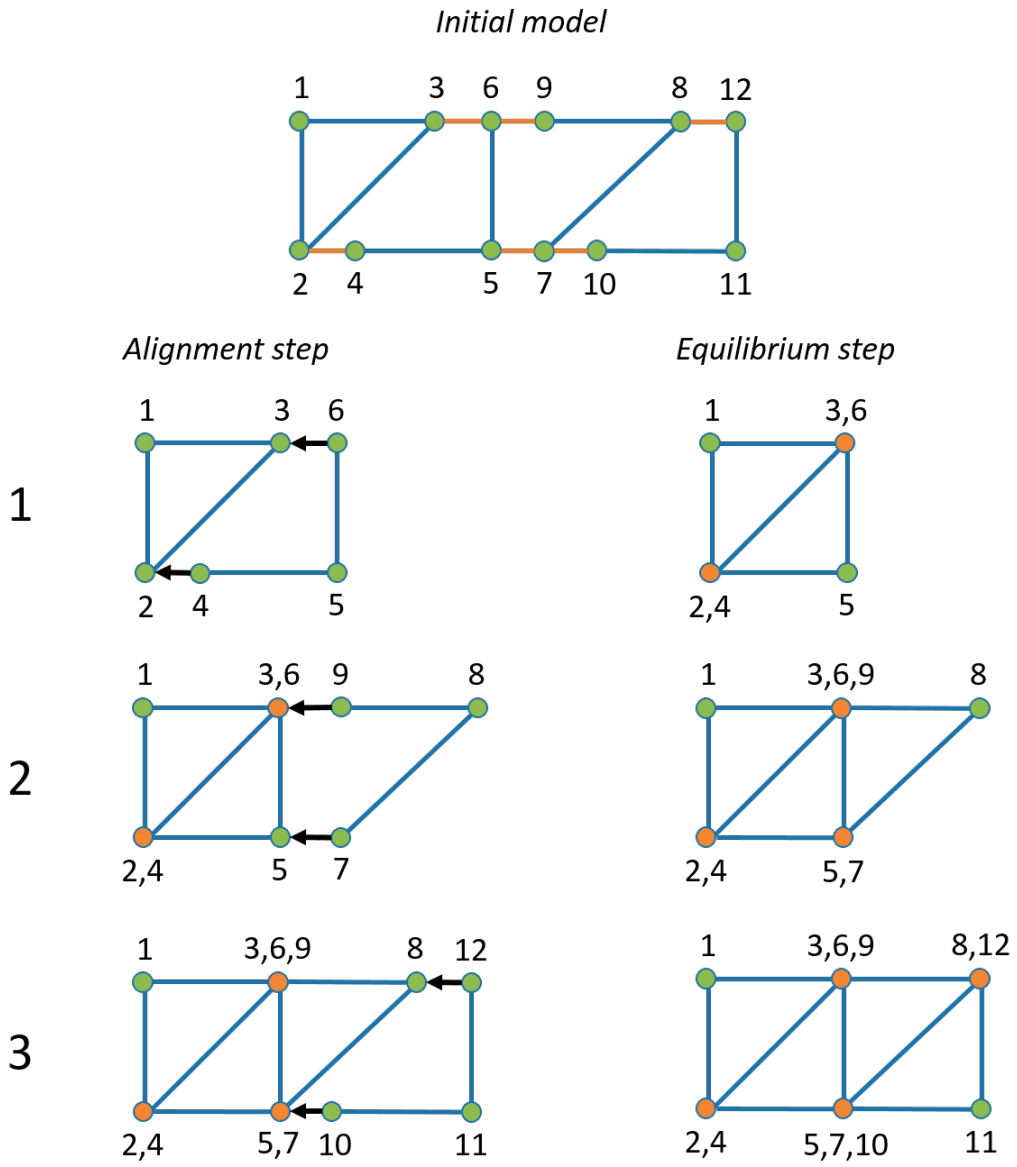

Figure 6.4: Method for simulating the assembly of a structure in Abaqus, illustrated with a simple 2D truss. Connectors are shown with orange lines in the initial model. In the steps, green circles mark the locations of single nodes. Orange circles mark the locations of multiple coincident nodes, all effectively merged with a joining connector.

In the simple 2D example, the final structure is simply a pin-jointed truss, with members linked by shared nodes. Theoretically, the equilibrium stresses and displacements can be obtained analytically by applying the length errors as initial

strains in the nominal geometry and using the singular value decomposition (SVD) method developed by Pellegrino [68]. Figure 6.5 compares the equilibrium shape of the structure as computed by Abaqus and the SVD method with the same set of length errors. The results are nearly identical for the two approaches, even when the displacements from the nominal geometry are magnified five times. Since the lengths are compatible and there are no external loads, the stresses should be zero. Indeed, the analytical solution computes exactly zero stresses, while the Abaqus solution computes stresses on the order of 10^{-5} Pa. The small discrepancies in the shapes are likely coupled to the small but non-zero stresses outputted by Abaqus, which are presumably the effect of numerical approximations.

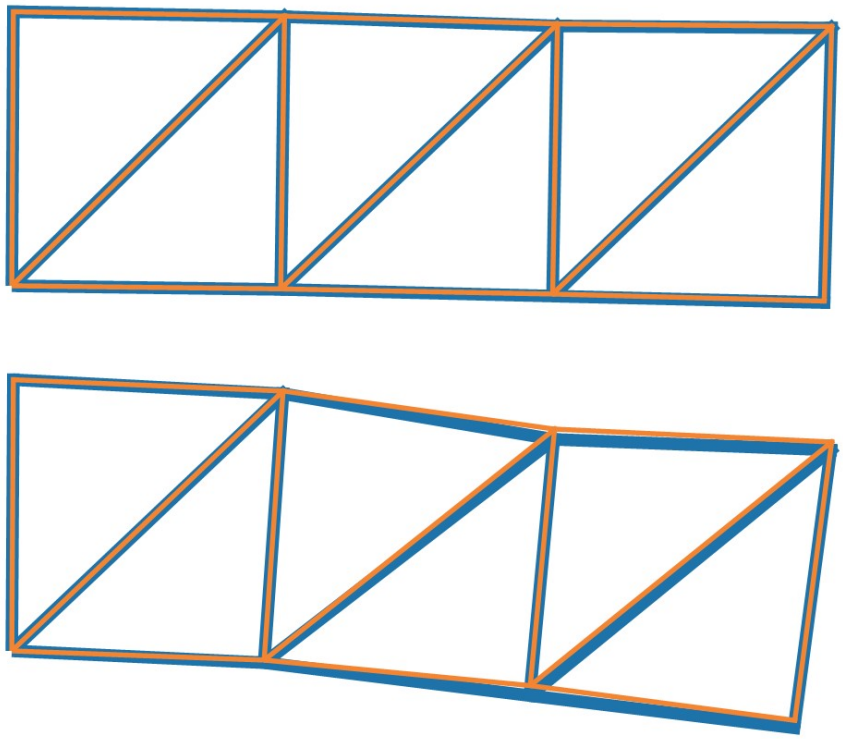

Figure 6.5: (Upper) Result of assembling a 2D erred truss structure with Abaqus (orange) and with SVD (blue). (Lower) the same result, with the displacements from the nominal geometry magnified five times.

6.1.2 Simulation with Modules

The procedure for assembling the ISTAR truss modules in Abaqus is very similar to that just outlined. The modules are modeled with beam elements, using the same overall geometry, member material and cross-section, joint material and cross-

section and all other relevant parameters described in Section 5.1. However, each module is constructed in the deployed position, and all hinges are replaced with rigid beams. Module errors are introduced by offsetting the endpoints of each member from their nominal positions in any translational direction. Again, these errors represent the residual effect of length errors, member alignment errors, and hinge axis errors post-deployment. Each endpoint offset in each direction is randomly drawn from a uniform distribution with bounds $\pm dE_{max}$. In the initial model, all modules are created such that their centroids align with the nominal tessellation of the backplane with 10 cm inter-module gaps. The backplane curvature is ignored for the purposes of this simulation. The connection points on each module are simply the nodes located at the vertices. The interconnects linking the connection points are modeled as single beam elements, assumed to have the same cross-section and material as the module joints.

At the start of the simulation, all elements are removed, except for those comprising two modules. The first module represents the hub, and is fixed at three vertices on the bottom surface. This module is said to be the *affixed module* in this step, or one that is already part of the assembled structure. The second module is the *free module*, or that currently being assembled by the robot. In the first alignment step, the connection points on the free module are displaced to their nominal location with respect to the connection points on the affixed module, as shown in Figure 6.6. This location is 10 cm from the affixed module connection point along a line from the center of the affixed module. The forced displacement causes stresses in the free module, but since they are not yet physically connected, the affixed module remains unstressed. In the first equilibrium step, the interconnects between the modules are restored in a strain-free state, since they are necessarily the nominal length of 10 cm after alignment. The stresses in the free module dissipate through the interconnects into the affixed module as the structure reaches equilibrium.

In the second alignment step, a third module is added, as shown in Figure 6.7. This new module is now the free module, while the first two modules are now both affixed modules. The user subroutine UAMP obtains the current coordinates of each connection point. From this information, the connection points on the free module are forced into alignment with the corresponding connection points on the affixed modules. Again, the forced displacement causes stresses in the free module, but since they are not yet physically connected, these stresses do not equilibrate with the affixed modules. In the second equilibrium step, the interconnects between

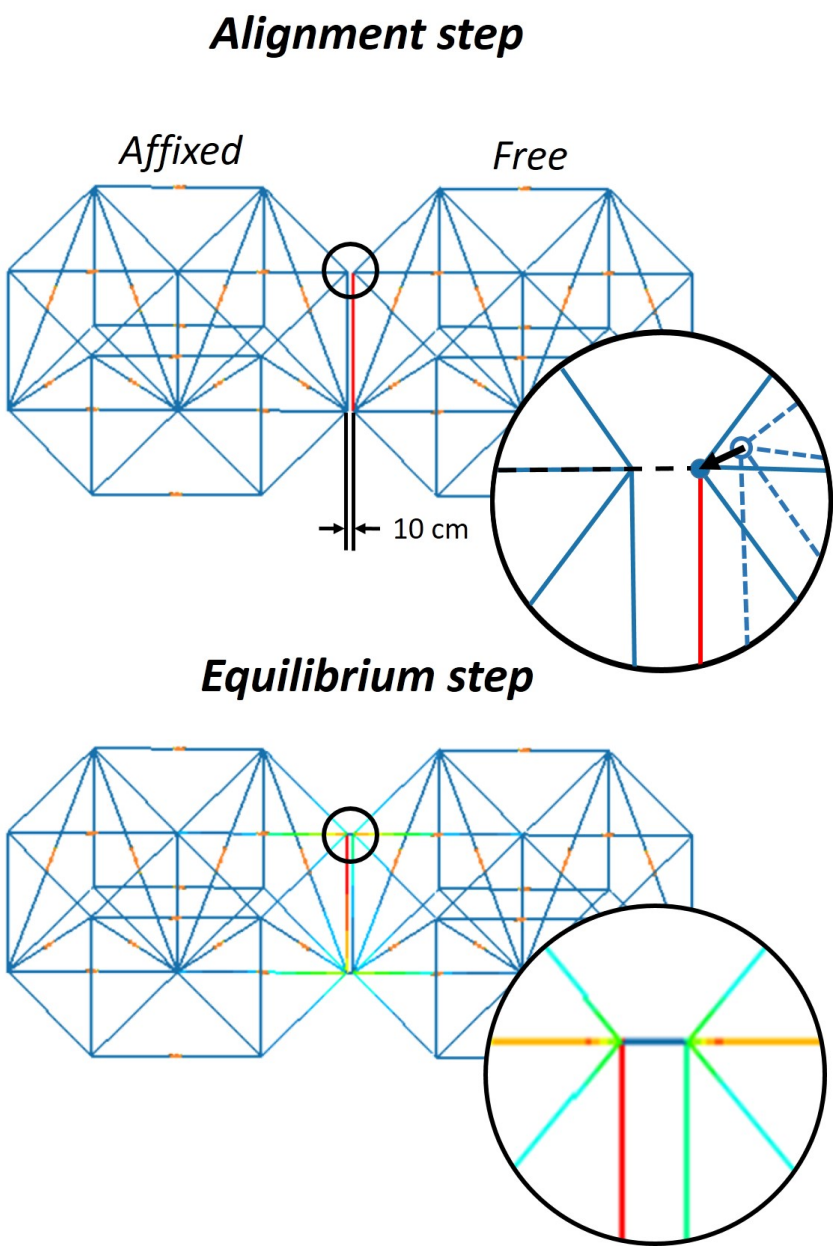

Figure 6.6: Illustration of the structure after the first alignment and equilibrium steps have been completed. The stresses are color-coded, with red being the highest and blue being the lowest. (Upper) In the first alignment step, the connection point on the free module is displaced to its nominal position 10 cm from the affixed connection point along a line from the affixed module center, as shown in the inset. Members in the free module become stressed as a result of the alignment, with stresses clearly concentrated in the red vertical member. (Lower) In the first equilibrium step, the beam element representing the interconnect is replaced in a strain-free state, and the structure reaches an equilibrium shape and stress distribution.

the modules are restored and the entire structure reaches an equilibrium stress state. Each subsequent alignment step adds a new free module and aligns it with the affixed modules, and each equilibrium step adds the interconnects and allows the structure to reach equilibrium.

6.1.3 Results

The assembly was initially simulated with dE_{max} set to 4.5 mm, corresponding to the manufacturing tolerances suggested in Section 5.11 for 100% deployment reliability. With these module errors, the shear strength of 50 MPa in the members was exceeded after just five modules were assembled. dE_{max} was then reduced to just 1 mm. With this bound, safe stress levels were maintained for up to 217 modules, corresponding to the $n_m = 9$, $D_{pm} = 94.3$ m design described in Section 2.4. Unfortunately, the largest design could not be assembled with this simulation method, as the Fortran code for the user subroutine UAMP was too large to compile. Figure 6.8 plots the surface errors for the $n_m = 9$ design with $dE_{max} = 1$ mm. This plot shows that the surface precision was nearly 20 mm, exceeding the maximum requirement of 10 mm. Furthermore, the surface error clearly increased radially from the center, indicating that the precision would worsen for the largest design. This trend is further emphasized in Figure 6.9, which plots the maximum surface error within each ring around the hub. The figure suggests that, for small aperture sizes, the growth of surface errors is less rapid. However, as the aperture size increases, the relationship to the maximum surface error becomes approximately linear, as predicted analytically by Hedgepeth[41]. This is a critical result, providing answers to the first set of questions posed at the beginning of this chapter. To maintain safe stress levels and 10 mm surface precision, the module errors will have to be less than 1 mm, meaning that the manufacturing tolerances required for a successful assembly are far more restricting than those required for a successful deployment. Increasing the range of the rigid body actuators may in fact be simpler and more cost effective than restricting the manufacturing tolerances to this level. Thus, a 1 mm module error bound that maintains safe stress levels but stretches the surface precision requirement is still considered a possibility for this mission.

In each assembly step, the free module was initially placed with its centroid in the nominal location and connected to adjacent modules at either 2, 4, or 6 connection points. Figure 6.10 plots the initial connection misalignments for each module in the $n_m = 9$ design. An upward linear trend is clearly visible, with misalignments on the edge of the backplane reaching up to 20 mm. However, even the minimum

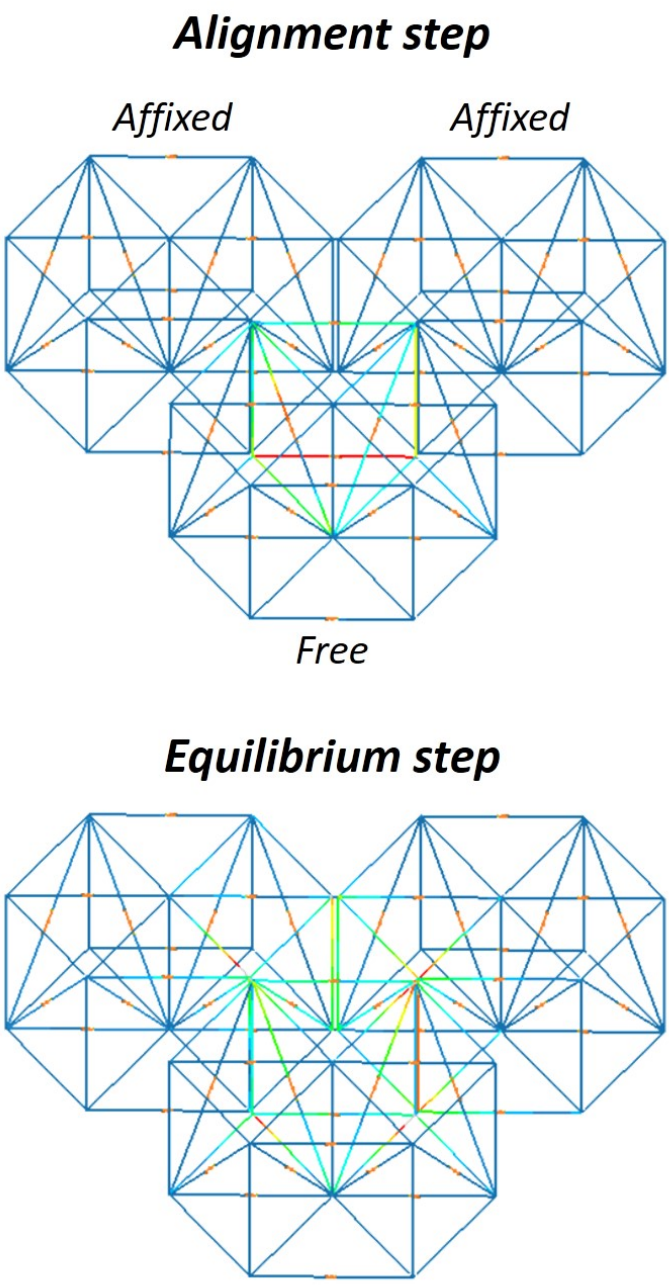

Figure 6.7: Illustration of the second alignment and equilibrium steps. At the start of the second alignment step, a new free module is added and its connection points aligned with those on the affixed (first and second) modules. The affixed modules still have the same stress distribution resulting from the first equilibrium step, but the stresses are much lower than those in the free module after the second alignment step. In the second equilibrium step, the interconnects are replaced, and the structure reaches a new equilibrium state as shown.

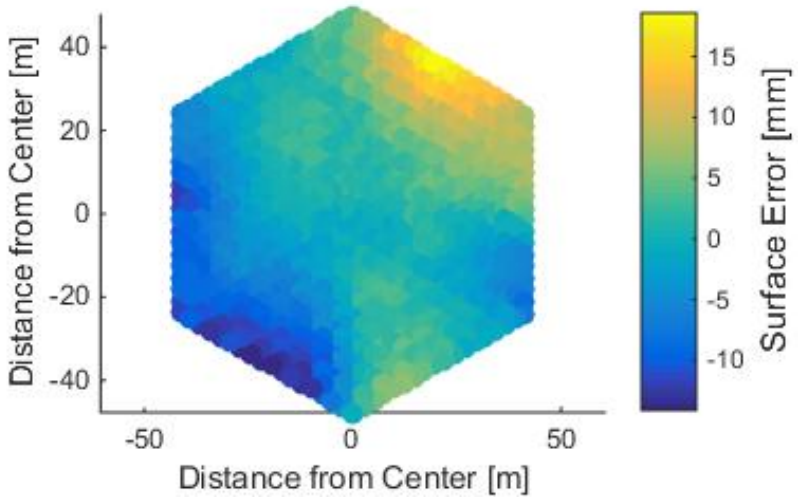

Figure 6.8: Surface errors for the $n_m = 9$ design.

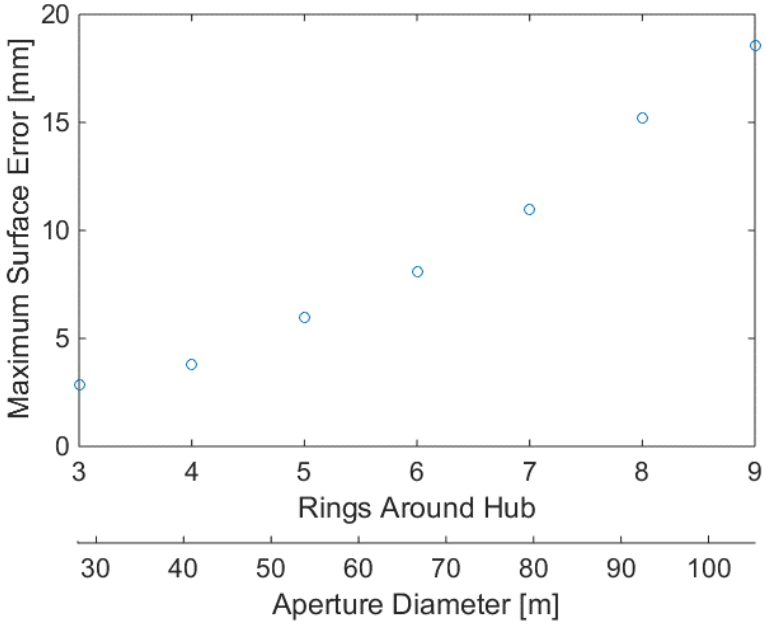

Figure 6.9: Maximum surface error within each ring around the hub. The secondary x axis translates the number of rings to the aperture diameter.

connection misalignment for each module clearly follows the same slope, suggesting that the entire module may have been offset as a rigid body from neighboring modules in its initial placement. This effect is clearly evident in Figure 6.11, which plots the mean in-plane direction of the connection misalignments for each module. This plot shows that the entire backplane was twisted about the center, with the amount

of twist increasing radially. Thus, module errors may lead to rigid body offsets that grow with the size of the backplane. However, these offsets can easily be removed during assembly by adjusting the initial position of the module accordingly and do not contribute to the stress in the structure. Thus, the interconnects only need to accommodate the residual connection misalignments after rigid body components are removed. With this correction, no upward trend with module number is evident, as shown in Figure 6.12. In fact, the combined module error distribution between any two modules, which is independent of the assembly process, is logically recovered, with the mean misalignment of 1.73 mm corresponding to a 1 mm error in all three directions. This result does exhibit how the applied module errors combined to yield connection misalignments up to 5 mm, even though the error at any one member endpoint in each module was less than 1 mm. Thus, the second set of questions posed at the beginning of this chapter is answered. In summary, module errors may cause bulk displacements in the backplane, such that the initial placement of each free module is increasingly offset from neighboring modules as the backplane size increases. However, the connection misalignments do not grow with the number of connections, but merely reflect the combination of random module errors at the connection points. Yet, these combinations may significantly amplify errors at any given connection point, yielding misalignments of up to five times the applied error level.

6.2 Interconnect Design and Prototype

With the above information, concepts for the interconnect between modules can be investigated. The direction from which each module approaches the partially completed backplane during assembly determines how the interconnects must be designed. For the three-edge connection, the approach is limited to two directions, illustrated in Figure 6.13: purely horizontal and purely vertical. The module cannot make one edge connection then rotate to make another. Rather, all three edges (six interconnects total) must be connected simultaneously. With the horizontal approach, the specific direction of each interconnect is not consistent; some must be oriented tangentially to the module and others radially. This significantly complicates either the interconnect design or the assembly process, forcing the robot to correctly orient the modules. With the vertical approach, all edge connections can be identical.

Following the vertical assembly approach, one simple concept for the interconnect is sketched in Figure 6.14. It draws upon similar concepts found in literature

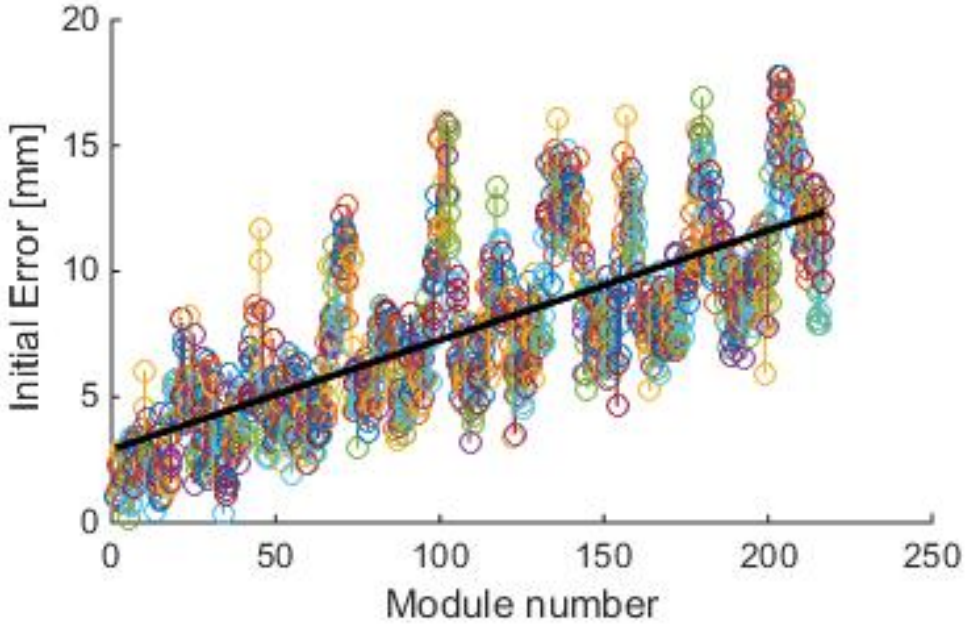

Figure 6.10: Initial connection misalignments for each module. Note that each module has between two and six connection points. The misalignment at each point is plotted with a circle, and every circle corresponding to points on a specific module are connected by a line. The linear regression trendline is shown in black.

and uses a magnetic interlocking cup and cone [37][36]. Again, the module currently being held by the robot and attached to the assembled structure is described as free, whereas the module that is already part of the structure is described as affixed. To make an edge connection, the free module must have the cup on the top connection point and the cone on the bottom connection point. This arrangement is described as a *free edge*, and a top cup or bottom cone is called a *free interconnect half*. Conversely, the affixed module must have the cone on the top connection point and the cup on the bottom connection point. This arrangement is described as an *affixed edge*, and a top cone or bottom cup is called an *affixed interconnect half*. Each module must have the correct number of free edges that attach to the assembled structure when that module is placed, and affixed edges to which other modules may attach as assembly progresses. According to the connection map in Figure 6.3, blue modules must have two free and four affixed edges, green modules must have three free edges, etc. The robot does have to orient each module correctly to align the free edges with the affixed edges. However, the vertical approach is still desirable over the horizontal approach, because the number of unique orientations and interconnect types is still reduced.

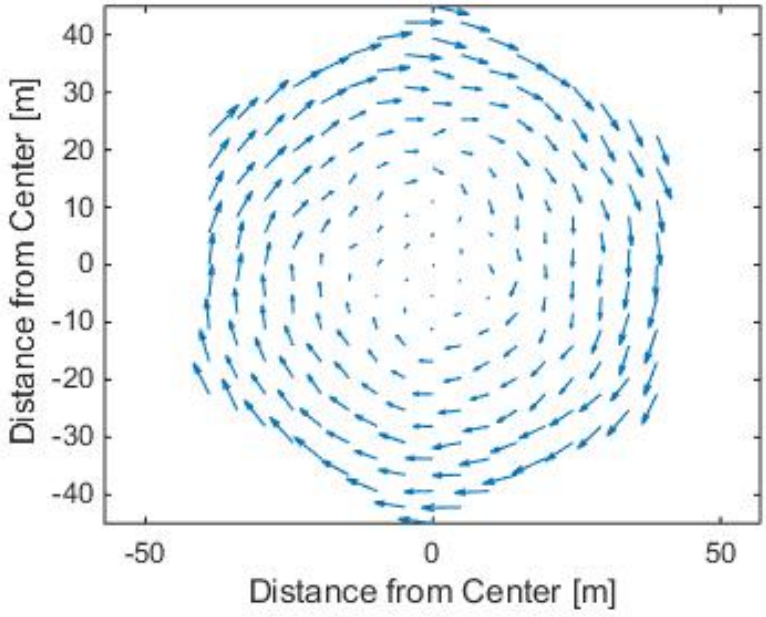

Figure 6.11: Illustration of the mean in-plane directions of the initial connection misalignments. The vectors can be interpreted as the rigid body displacement of the module from its initial location, or nominal location in the backplane, to its location just after alignment. Its final position in the backplane may still change once an equilibrium state is reached. The lengths of the vectors are simply scaled to show relative magnitudes, and do not have any quantitative meaning.

The diameter of each cup/cone base is set to 6 cm. For convenience, the cup/cone height is set to be equal to the radius. Again, the nominal gap between modules is 10 cm, which must be spanned by the *gap spacer* that holds the cup interconnects (see Figure 6.14). Furthermore, this spacer must be adjustable to create the curvature of the mirror, with a range up to 10 mm. Large adjustments may be made with a simple screw system, while fine adjustments may be made with a piezo actuator; the details of the mechanism are beyond the scope of this research. It should be noted, however, that the gap on the bottom of the modules must necessarily be larger than the gap on the top to create the curvature. Thus, the gap spacer must also allow for an angle between the connected edges. The geometry is shown greatly exaggerated in Figure 6.15. The smallest value of R_{pm} enabled in the ISTAR architecture is 222.4 m, corresponding to the smallest value of D_{pm} of 27.8 m (see Section 2.4). The design value of H is again 2.76 m. This yields an angle β of only 0.13°. The kink angle in the bottom interconnect is only $\beta/2$, making x only 5.62 μm. Furthermore, the difference between the gap lengths at the top and bottom of the module is only 1.2

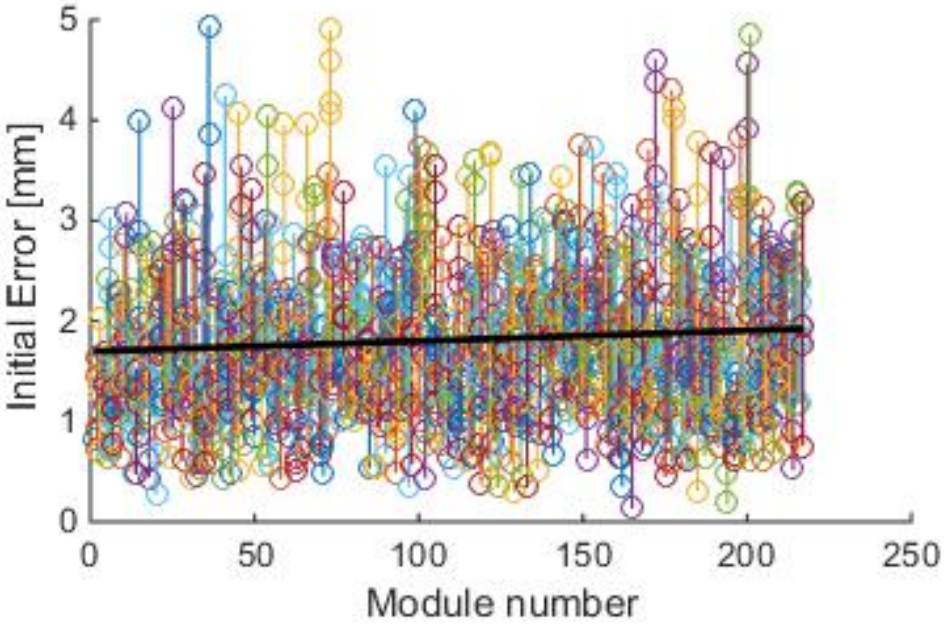

Figure 6.12: Initial connection misalignments for each module with rigid body components removed. Note that each module has between two and six connection points. The misalignment at each point is plotted with a circle, and every circle corresponding to points on a specific module is connected by a line. The linear regression trendline is shown in black.

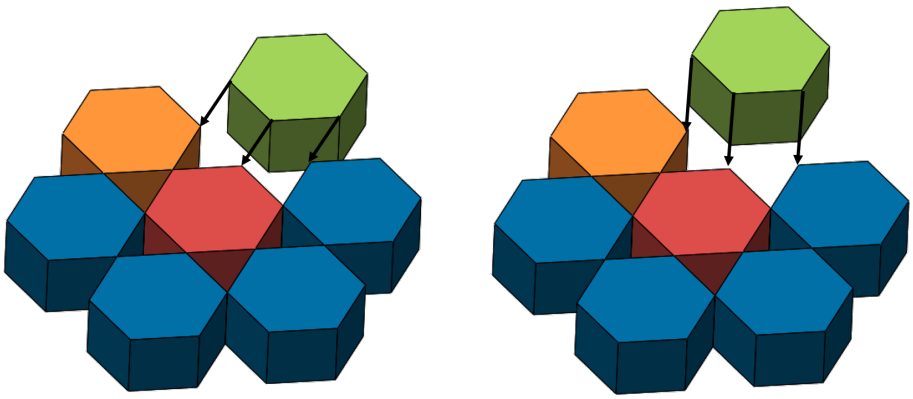

Figure 6.13: Illustration of approaching a connection horizontally (left) and vertically (right). The arrows show that, with the horizontal approach, two of the edge connections must be oriented tangentially to the modules, and the third must be oriented radially.

mm. Thus, while the angle is necessary, it should not be difficult for the mechanism to provide, and the kink should not significantly affect the structural integrity.

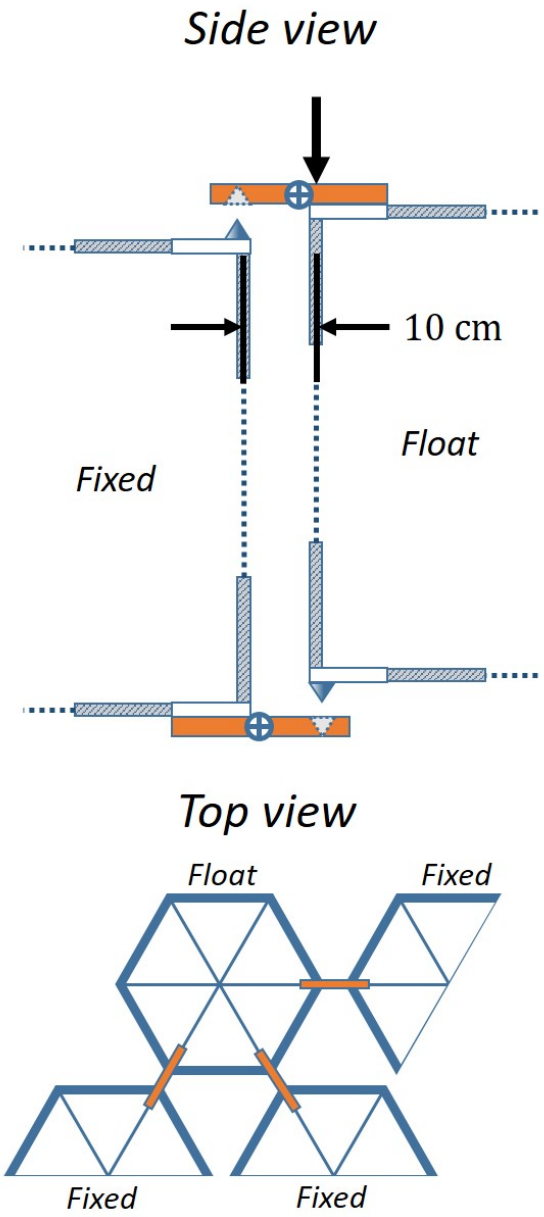

Figure 6.14: Sketch of two interconnects linking a free edge and to an affixed edge. Affixed edges have a cone on the top surface of the module and a cup on the bottom surface of the module. Free edges have a cup on the top surface of the module and a cone on the bottom surface of the module. The cups are held by adjustable gap spacers with lengths set by the robot to create the required gap between the modules. The nominal gap distance is 10 cm, with variations determined by the curvature of the backplane structure.

To better visualize the process of connecting modules, a mock-up of the hub and each module in the first ring was designed and 3D printed, as shown in Figure

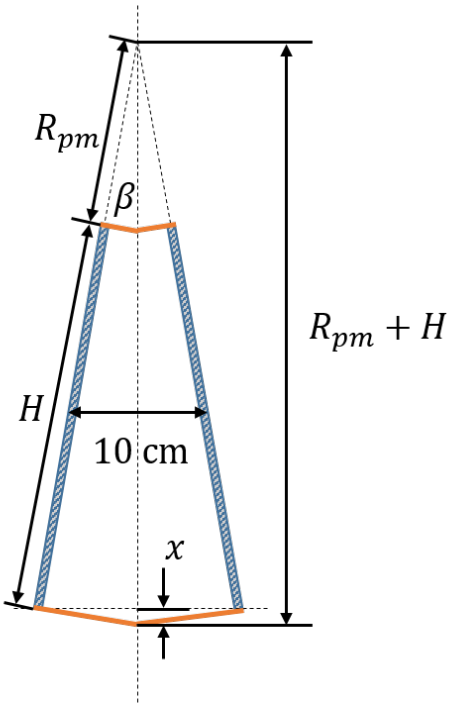

Figure 6.15: Diagram of the gap variation from the top to bottom surfaces of the backplane structure. R_{pm} is the radius of curvature of the top surface and H is the module depth. The nominal gap between the centers of the modules is 10 cm. The curvature is shown greatly exaggerated for clarity; R_{pm} is actually much larger than H, and thus the angle β is close to zero.

6.16. Each cup and cone were equipped with small but strong magnets to model the interconnect behavior.

6.3 Interconnect Simulation

This simple interconnect design is not feasible unless the interconnects are demonstrated to fully engage despite module errors. As determined by the assembly investigation, the module error bound dE_{max} is set to 1 mm. This section describes the Abaqus simulation model and technique developed to predict the performance of the interconnects with these error levels and determine their feasibility.

6.3.1 Simulation Building Blocks

In Abaqus, each cone is modeled with a combination of hexahedral (C3D8R) and tetrahedral (C3D6) elements, seeded such that nodes are concentrated near the tip, as shown in Figure 6.17*a*. Cones are assumed to be aluminum, with corresponding material properties. Each cup is modeled as a conical analytical rigid surface. Numerical problems resulting from the discontinuity at the tip of the

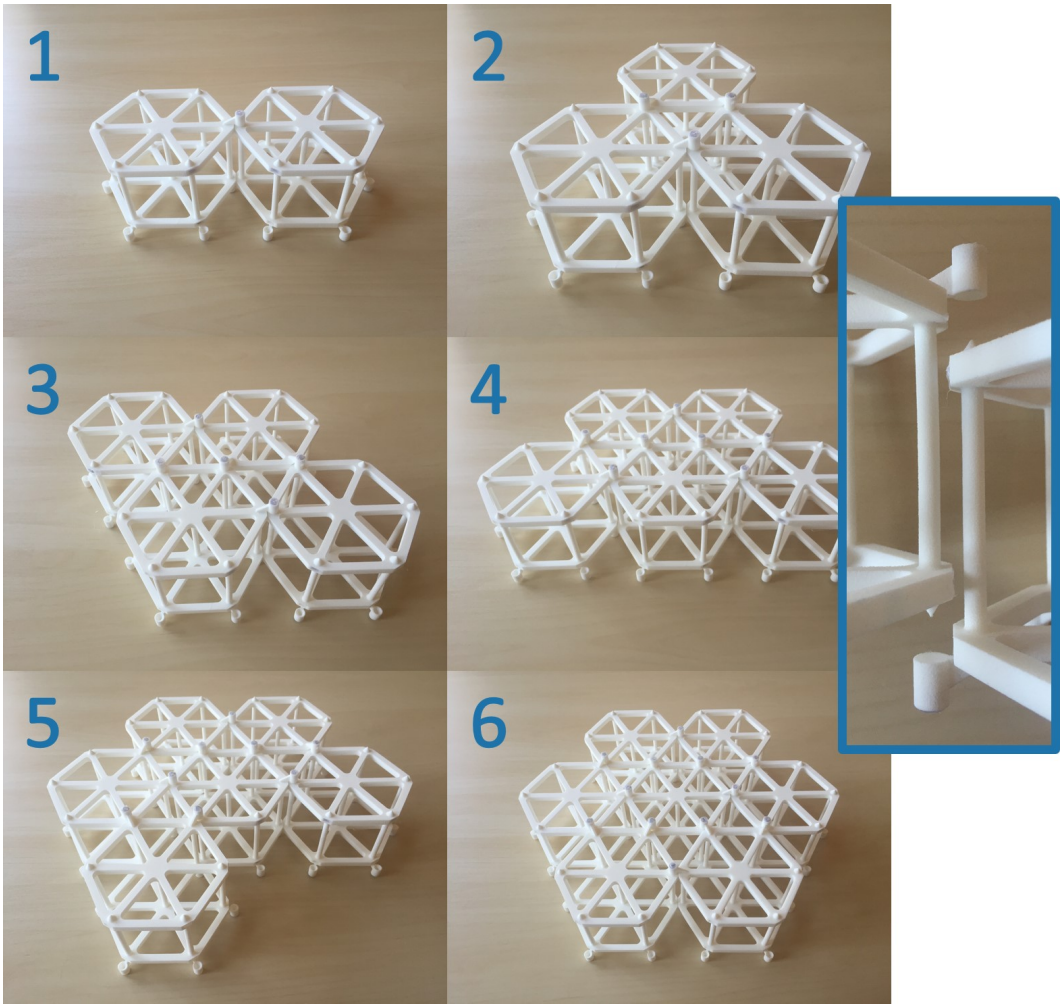

Figure 6.16: Photos of the 3D-printed mock-ups of the first seven modules. The inset shows the detail of one edge connection.

cup are avoided by placing a secondary flat rigid surface at this point, as shown in Figure 6.17*b*. The size of the secondary surface can be arbitrarily small for the simulation to run smoothly, but it is set to have the same radius as the base of the cup for convenience. Again, the base radius and height of each cup and cone are both 3 cm. The cup surfaces (conical and flat) are defined to interact with the outer nodes on the cone, acting as a hard boundary with sliding friction. The friction coefficient is set to 0.04, assuming that all surfaces are coated with Teflon [69]. The magnetic force between the cups and cones is not modeled, but rather it is assumed that the magnets will hold the interconnects together once fully engaged, or the cups and cones are in complete contact with each other.

To verify that the interconnect model behaves realistically, three simple tests were performed. In the first and simplest test, a cone and much larger cup were

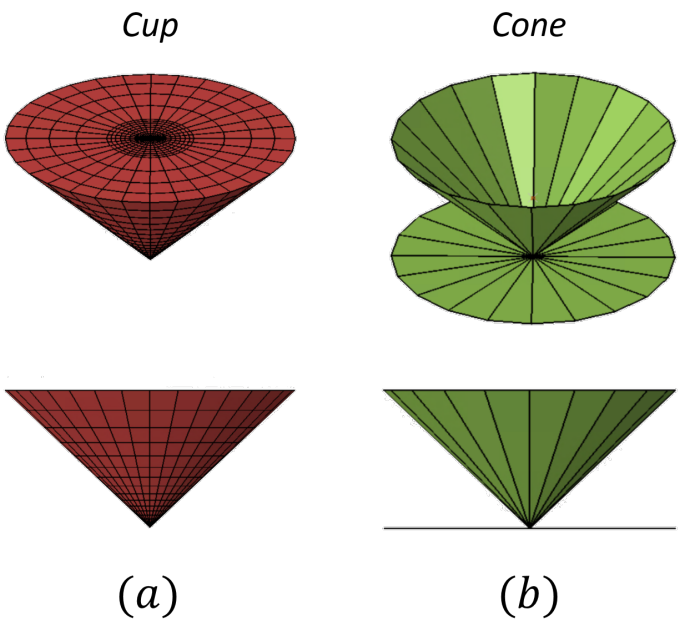

Figure 6.17: Abaqus models of the cup, composed of solid elements, and the cone, composed of two analytical rigid surfaces.

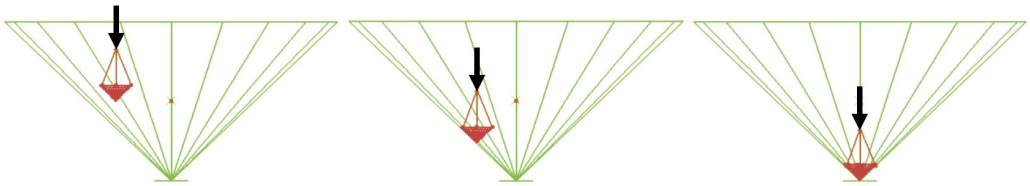

Figure 6.18: Diagram of the simple test performed to verify that the cup acts as a hard boundary. The cone is connected to a tripod of rigid beams at three points around the edge of its base. The tip of the tripod is linearly displaced downward until the cone touches the cup, slides down to the bottom, and is held in place. At this point, the interconnect is fully engaged.

constructed. The top surface of the cone was linearly displaced toward the cup. As expected, once the tip of the cone touched the cup surface, the displacement was deflected such that the cone moved along the cup until it was held in place at the bottom, or the interconnect was fully engaged, as shown in Figure 6.18.

The second test evaluated whether the interconnect would yield realistic displacements and stresses in a simple system. An M55J CFC cantilever beam with a length of 2.76 m and circular cross-section with diameter 3.5 cm was constructed. The node at the free end of the beam, or the beam tip, was attached to a cone with one rigid beam connector per each node on the cone base surface, as shown in Figure

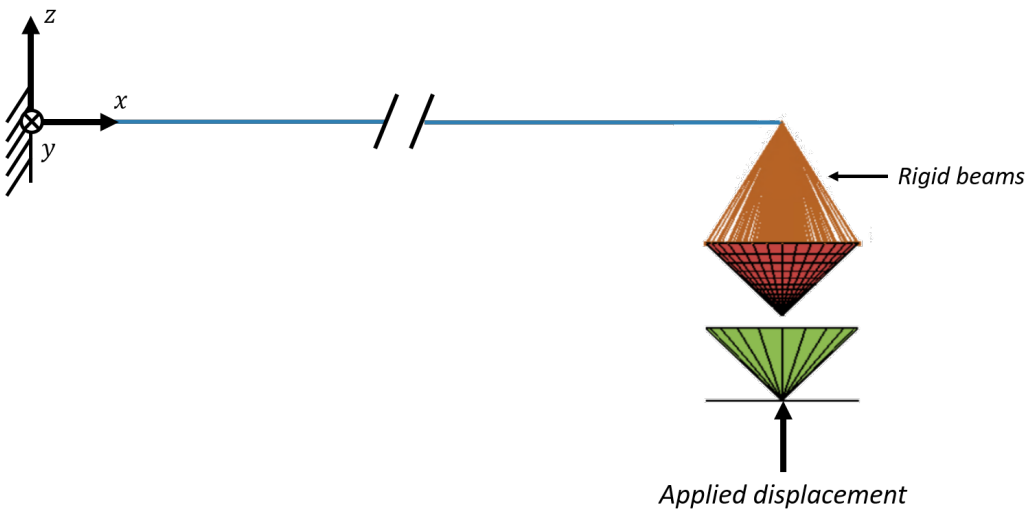

Figure 6.19: Diagram of the cantilever beam system with the cup/cone pair. The beam is much longer than shown.

6.19. Three different simulations were performed. First, in a linear static step, the tip was simply deflected in the z direction by 0.5 cm. All other degrees of freedom at the tip were constrained. Second, again in a linear static step, the cup was moved in the z direction by 0.5 cm starting from the point at which it met the cone. Thus, the cone was deflected by approximately 0.5 cm, with some potential slip between the surfaces. The third simulation was the same as the second, but the analysis was nonlinear. For each simulation, the stresses and displacements along the length of the beam were recorded.

The boundary condition at the tip in all three simulations can be approximated as a clamped constraint. From Euler-Bernoulli beam theory, this is equivalent to requiring that $w(2.76\text{ m}) = 0.5\text{ cm}$ and $w'(2.76\text{ m}) = 0$, where $w(x)$ is the displacement of the beam in z at a distance x from the root. With the additional constraints that $w(0) = w'(0) = 0$, the standard beam equation, $w''''(x) = 0$, can be integrated to yield $w(x)$:

$$w(x) = \frac{0.5\text{ cm}}{(2.76\text{ m})^3}\left(3(2.76\text{ m})x^2 - 2x^3\right).$$

The magnitude of the stress at the top and bottom of the beam is then $\frac{3.5\text{ cm}}{2}EIw''(x)$, where E is the elastic modulus of the beam and $I = \pi(3.5\text{ cm})^4/64$ (circular cross-section).

On the left, Figure 6.20 plots the displacements in z and stresses along the top of the beam as computed by the three Abaqus tests and the analytical solution. The

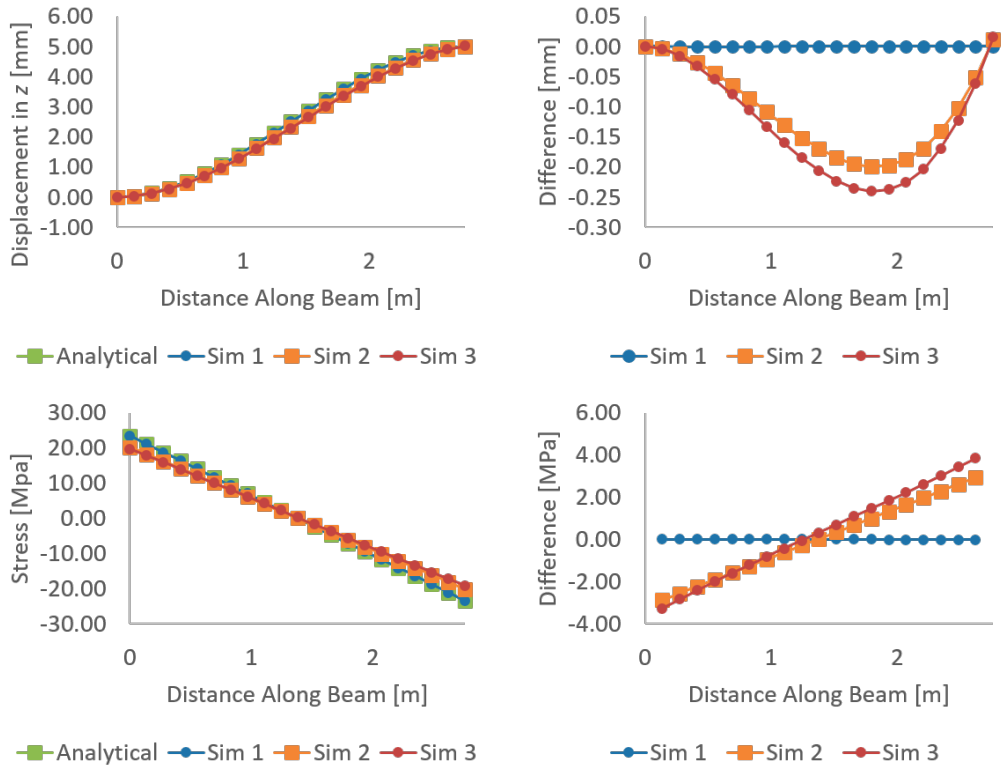

Figure 6.20: (Left) Displacement in the z direction and stress along the top of the cantilever beam for the three simulation models and the analytical solution. (Right) Differences in the displacement and stress from the analytical solution for the three simulation models.

differences between the Abaqus simulations and the analytical solution are plotted on the right. As expected, the first simulation in which the tip was deflected directly and the other DOFs were constrained almost exactly matches the analytical solution. The results of the second and third simulations show the effect of slip between the cup and cone surfaces. Rather than remaining straight in the cup, the cone tilted slightly back toward the beam, as shown in Figure 6.21. Thus, the slope near the tip of the beam was non-zero, and the displacements in z were slightly decreased (4% near the center), leading to lower stress magnitudes overall. The tilt also compressed the beam in the x direction, relieving the tension stresses and adding to the compression stresses, leading to a stress differential of about 2 MPa from the bottom to the top of the beam that was constant along the length. This is in contrast to the analytical solution and first simulation, in which the stresses along the top and bottom of the beam were equal in magnitude. In a final simulation, a force in the $-z$ direction was applied to the tip. As expected, this pushed the cone further into the cup, decreasing the tilt. The results of this test demonstrate that the cup and cone

behave as expected; the cone acts as a hard boundary, but slip between the surfaces is possible and may affect the connected structure.

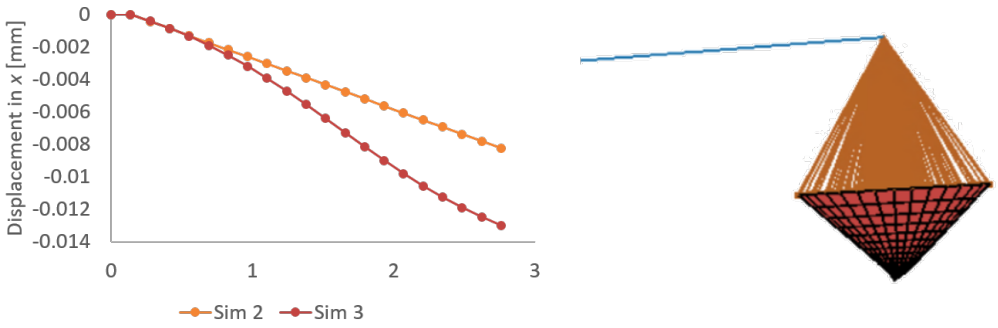

Figure 6.21: (Left) Displacement along the beam in the x direction. (Right) Image of the cone tilt amplified 100 times.

Finally, the third simulation analyzed the effect of a slightly misaligned single edge connection. To model the free edge, a vertical beam was constructed with the same dimensions as the truss module vertical members: length of 2.76 m, outer diameter of 3.5 cm, and wall thickness of 3 mm (pipe cross section). A single beam element with the same material and cross-section as the ISTAR module joints was attached to the top of the vertical beam on one end and to a cup on the other to model the gap spacer, as shown in Figure 6.22. A cone was attached to the bottom of the beam. Another cup and cone were fixed in space to mimic the affixed edge of another module. First, the affixed interconnect halves were placed exactly below the free interconnect halves. The top of the beam was pushed down in the z direction until tips of the cones just touched the bottoms of the cups. As expected, the reaction force at the control point and the stress in the beam were approximately zero. Then, the affixed cone was offset by 1 mm in the $-y$ direction and the affixed cup was offset by 1 mm in the $+y$ direction. The top of the beam was displaced by the same distance. The stresses in the beam resulting from the misalignment were less than 2 MPa. However, the reaction forces required to displace the beam and push the interconnects together were up to 2 kN in both the y and z directions. The results of this test suggest the reaction forces computed in this model may be exaggerated, because the cups are unrealistically rigid. However, the stresses in the beam are likely realistic.

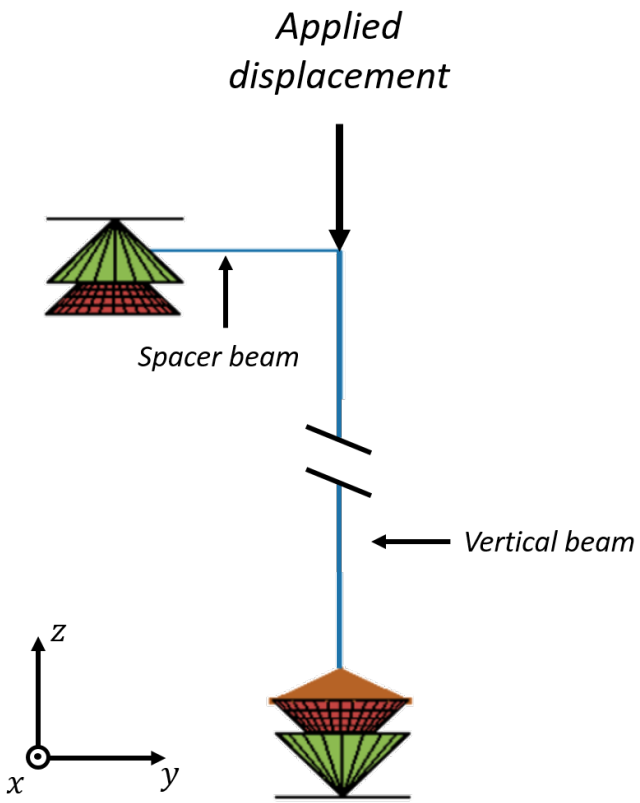

Figure 6.22: Diagram of the simple misaligned edge connection test. The vertical beam has the same length, material, and cross-section as those in the ISTAR truss module. The beam is treated as a free edge, equipped with free interconnect halves. The free cup is held by a spacer beam. Affixed interconnect halves are nominally located just below the free interconnect halves, but a small offset in the y direction is applied.

6.3.2 Full Model

Figure 6.23 shows the full model of the ISTAR truss module with three free edges to be connected. The spacer beams holding the free cups are 10 cm long and have the same material and cross-section as the joints. Each spacer is offset from the structure in the z direction by b_j to incorporate its width and the width of the joint. As in the assembly simulation, the module is not deployable, with rigid beams replacing the hinges. Endpoint errors within $\pm dE_{max}$ may be applied in each direction. Affixed interconnect halves are nominally placed just below the free interconnect halves, but may be offset in any direction by a random error within $\pm dE_{max}$.

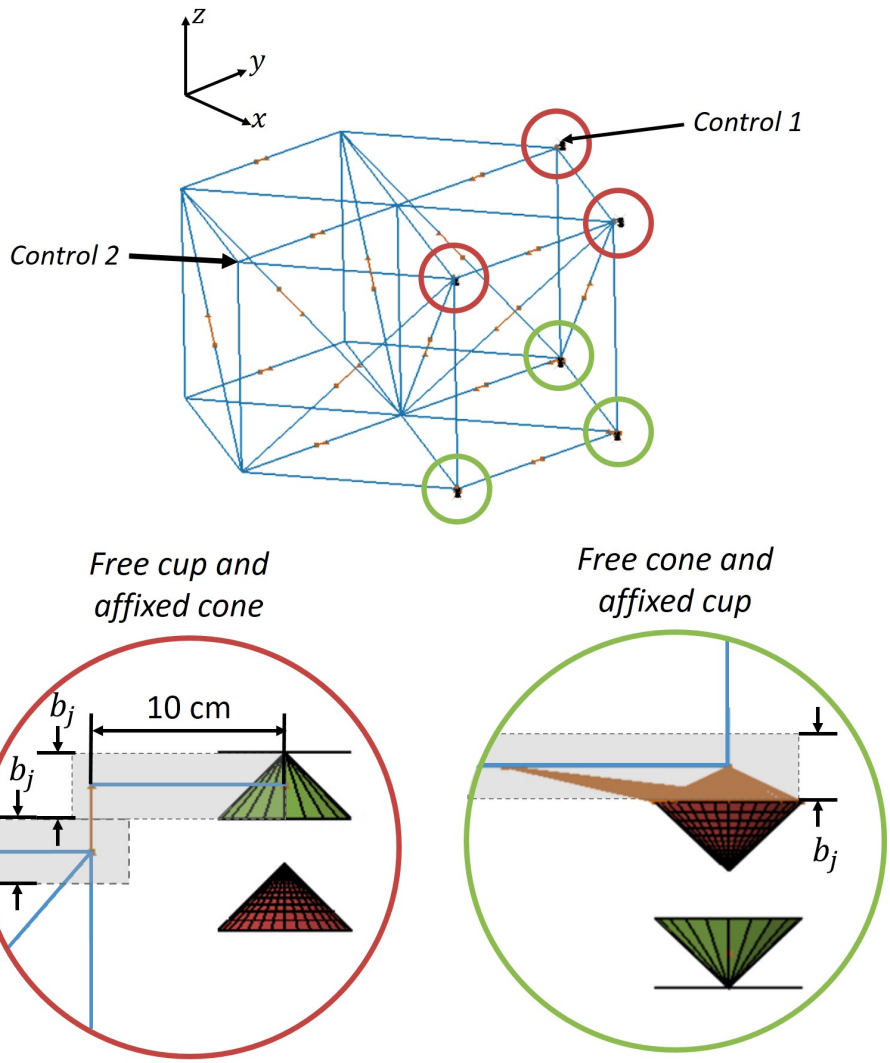

Figure 6.23: Diagram of the full module with three free edges equipped with free interconnect halves. The free cups and affixed cones are highlighted with red circles and the free cones and affixed cups are highlighted with green circles. The free cones are offset from the module in the $-z$ direction by a distance of $b_j/2$, to model the actual size of the joints to which they are connected. Each free cone is held by rigid beams that connect every node on its top surface to two nodes on the module as shown. The free cups on the top surface are offset from the module in the $+z$ direction by a distance b_j, to model the actual size of the joints and the spacers to which they are connected. The length of the spacer beam is set to 10 cm. Affixed interconnect halves, representing those on other modules, are nominally placed in line with the free halves in the z direction, such that the distances between the cone tips and cup bottoms are all equal. The nodes controlled during the simulation are labeled.

At the start of the simulation, for each interconnect, the tip of the cone and the

bottom of the cup have some initial distance. In a nonlinear stabilized static step, with a stabilization factor 5×10^{-7}, an initial constant velocity of 1 m/s in the $-z$ direction is applied to the controlled nodes, with all other DOFs unconstrained. Note that, because the analysis is static, the magnitude of the velocity has no affect on the results. The user subroutine UAMP tracks the cup/cone distances after each time step. When all distances are less than a given threshold, the control velocity is set to zero and the simulation is concluded. The distance threshold will necessarily be surpassed in the last time step, possibly leading to compression in the interconnects if the time increment is too large. If this is the case, the results of the last time step are ignored.

6.3.3 Results

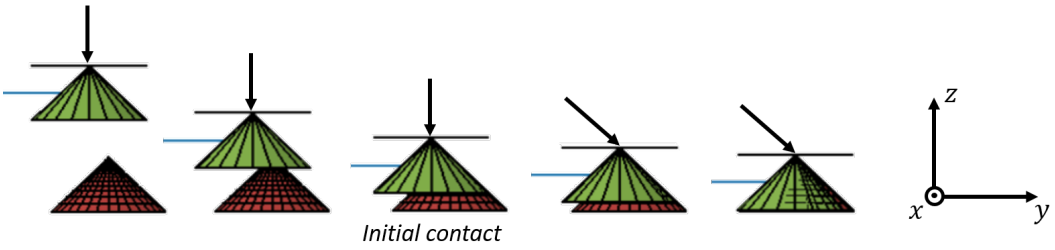

Figure 6.24: Frames depicting an interconnect with a free cup and affixed cone. Initially, the cup is displaced in the $-z$ direction. When it contacts the cone, the offset causes it to slide in the y direction until fully engaged.

As an initial test case, all errors were set to 0 and the control velocity was applied until the distances between the interconnect halves were less than 0.1 mm. As expected, the stresses in the module and reaction forces at the controlled nodes were approximately zero throughout the simulation, since the interconnect halves never came into contact. In a second test case, all of the affixed interconnect halves were moved by 1 cm in the y direction. The initial distance was set to 5 cm and the initial time increment was set to 1 ms. The same distance threshold of 0.1 mm was applied. As expected, when the cones and cups came into contact, the entire structure slid by 1 cm in the y direction, as shown in Figure 6.24. Figure 6.25 plots the distances between the cups and cones for each of the six interconnects. The six distances were all equal since the misalignment was uniform, and thus only one line is apparent. The independent variable is the enforced displacement of the controlled nodes in the $-z$ direction. Of course, the distances in z decreased linearly from 5

cm to 0, according to the applied control. The distances in y remained constant at 1 cm until contact was made, and then decreased linearly to 0. The distances in x should have been zero for the entire simulation, but some small numerical errors were evident after initial contact. As expected, the stresses in the module members and the reaction forces at the controlled nodes were approximately zero throughout the simulation.

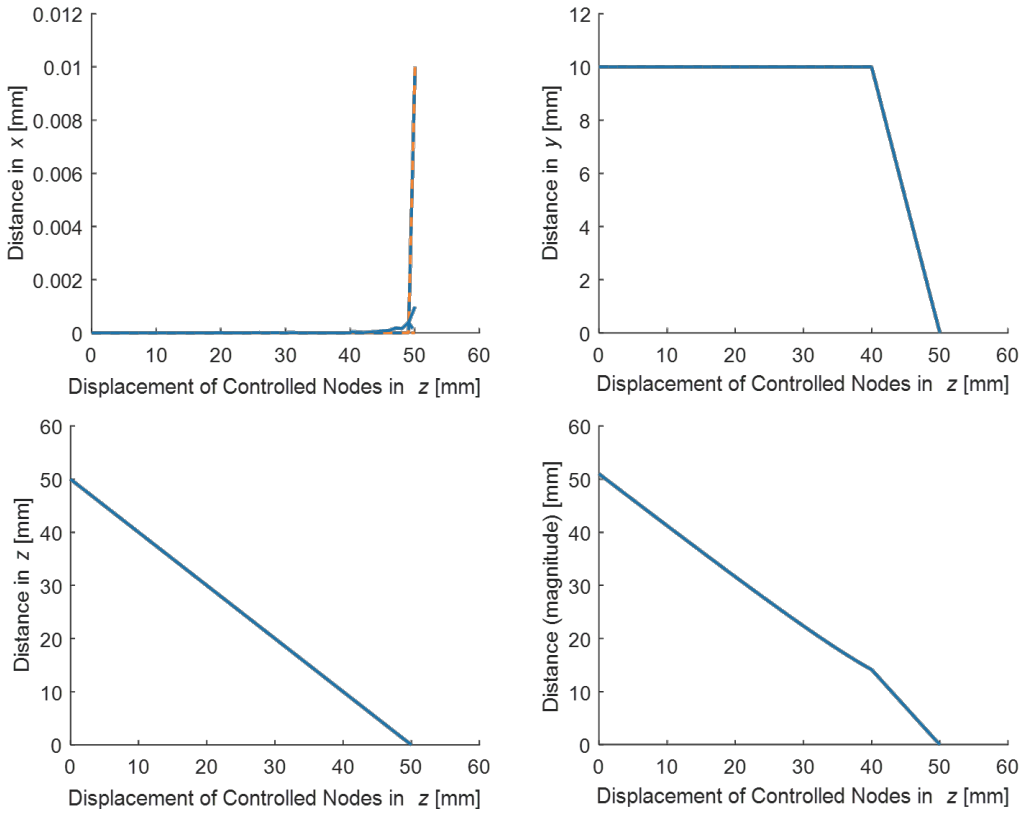

Figure 6.25: Plots of the cup/cone distances for each of the six interconnects in the full model for the uniform misalignment test. While all six distances are plotted, only one line is evident, since all of the distances are equal.

Then, dE_{max} was set to 1 mm, the same module error bound that resulted from the assembly investigation. The initial distance was decreased to 5 mm, and the initial time increment again set to 0.01 ms. In this simulation, the distance threshold was never reached, and the controlled nodes were displaced until too many iterations were required to find an equilibrium solution. Figure 6.26 plots the interconnect distances against the z displacement of the controlled nodes. The first vertical line marks the point at which the reaction forces in the controlled nodes exceeded 0.01 N, or contact was first made between the interconnect halves. The second vertical

line marks the point at which the reaction forces exceeded 300 N, or the maximum the robot can apply. Again, these forces are likely overestimated, since the cups and affixed interconnect halves are unrealistically rigid. The key result in the plot is that, at a certain point, pushing downward on the structure did not decrease the distances between the interconnect halves. Rather, for some interconnects, the distance actually increased, caused by the spacer beam bending, as shown in Figure 6.27. The largest *residual distance*, or the minimum distance of the interconnect, shown in blue in this case, was as high as 2.28 mm. Note that this is more than twice the applied error bound, again demonstrating how errors can combine and amplify in the module.

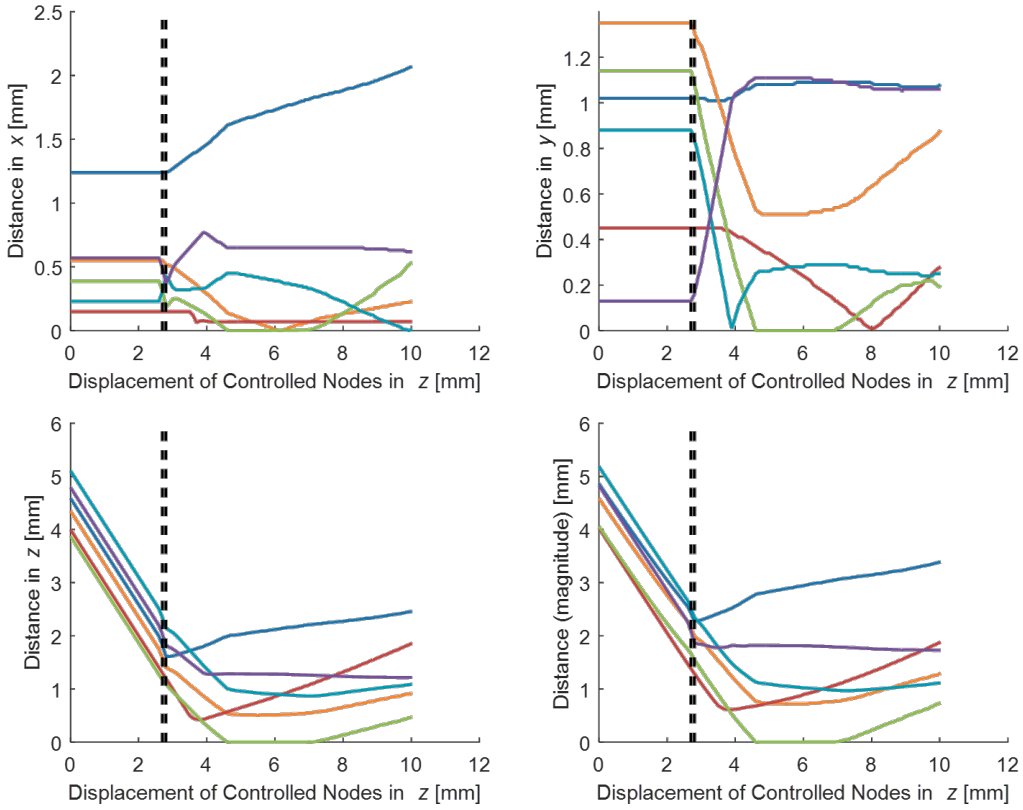

Figure 6.26: Plots of the cup/cone distances for each of the six interconnects in the full model for the random misalignment test. The first vertical line marks the point at which the reaction forces at the controlled nodes exceed 0.01 N and the second line marks the point at which the reaction forces exceed 300 N. These lines are nearly coincident, and thus may appear as one line depending on the quality of the image.

This is a critical result, suggesting that the proposed simple interconnect design may be insufficient to ensure full engagement with these applied errors. One possible

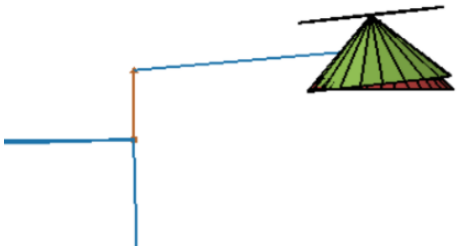

Figure 6.27: Image of a spacer beam bending, which increases the distance between the cup/cone pair despite the downward displacement.

modification involves a two-stage system: an initial "soft capture" stage and a locking stage. In the soft capture stage, the interconnects are allowed some movement to conform to misalignments. Once the interconnects are fully engaged, this motion is constrained, locking them in place and making the assembled structure rigid. Designing such a system is beyond the scope of this research. However, the soft capture can be modeled by adding springs to the fixed interconnects, as shown in Figure 6.28. The previous simulation was repeated with the same geometry and error distribution, but with the addition of springs. The spring constants were 5 N/mm in the x direction, 5.01 N/mm in the y direction, and 50 N/mm in the z direction. Note that slightly different spring constants in each direction were necessary to provide a preferential direction in the simulation; otherwise, Abaqus could not find a solution. To avoid having too many unconstrained degrees of freedom, the controlled nodes were fixed in all directions and rotations other than z, the direction of the controlled velocity. The resulting distances between the cup/cone pairs are plotted against the z displacement of the controlled nodes in Figure 6.29. Clearly, the residual distances were greatly reduced, with the maximum among the interconnect pairs only 0.56 mm. Compared to the maximum residual of 2.28 mm for the model without the springs, adding the springs improved the result by 75%. However, the residual distances were still non-zero, and thus the interconnects did not fully engage.

6.4 Chapter Conclusions

This chapter first outlined the assembly plan in detail. In this plan, modules are assembled in rings around a central hub. Each module is lowered into place by the robot from the top of the backplane, to reduce the number of unique connection types. Depending on its location in the backplane, a given module may be connected to adjacent modules along one, two, or three edges. Each edge connection is created

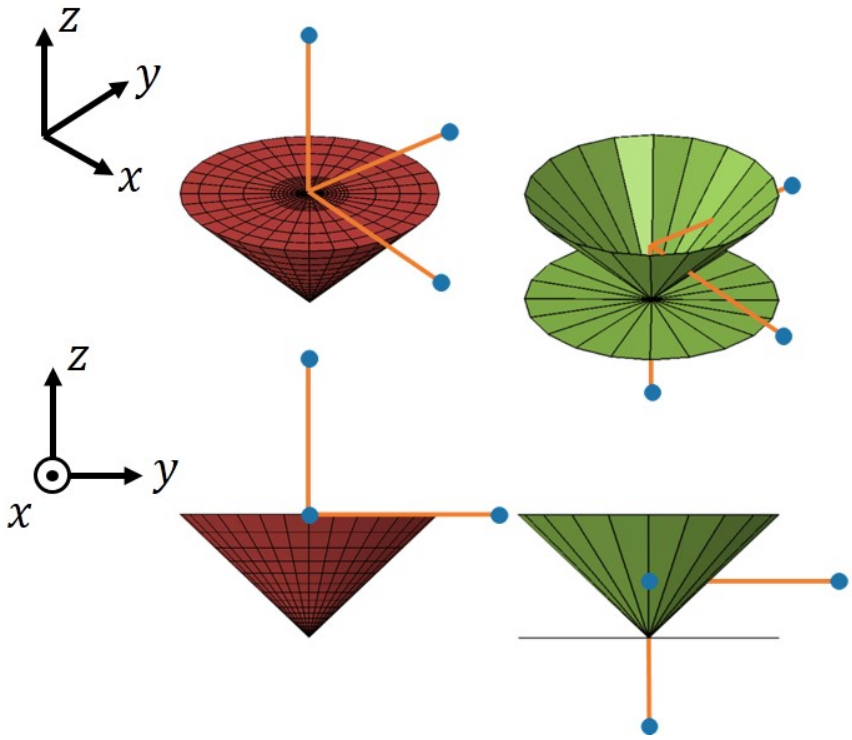

Figure 6.28: Affixed cup and cone with one attached spring in each direction. The springs are connector elements linking the nodes marked with blue circles to the node at the center of the cone base or the reference node of the cup analytical surface. The blue nodes are fixed in space.

by two interconnects, one between connection points on the top of the modules and one between connection points on the bottom of the modules. Thus, for modules connected along three edges, six interconnects must engage simultaneously.

The effect of fabrication errors on the assembly process was then investigated. A simulation technique was presented that sequentially adds modules with realistic material properties to a structure, allowing initial connection misalignments, stresses, and surface errors to be tracked during assembly. Using this technique, the assembly of the ISTAR modules was simulated, and the surface precision was shown to decrease as the size of the backplane increased. One critical conclusion was drawn from these results: the manufacturing tolerances are not limited by the deployment reliability, but by the required surface precision and maximum allowable stresses during assembly. In fact, the manufacturing tolerances posed by the assembly may be up to five times more restrictive, with subsequently soaring construction costs. Further investigation is required to determine whether an increase in capabilities of the wavefront sensing and control system would actually be simpler

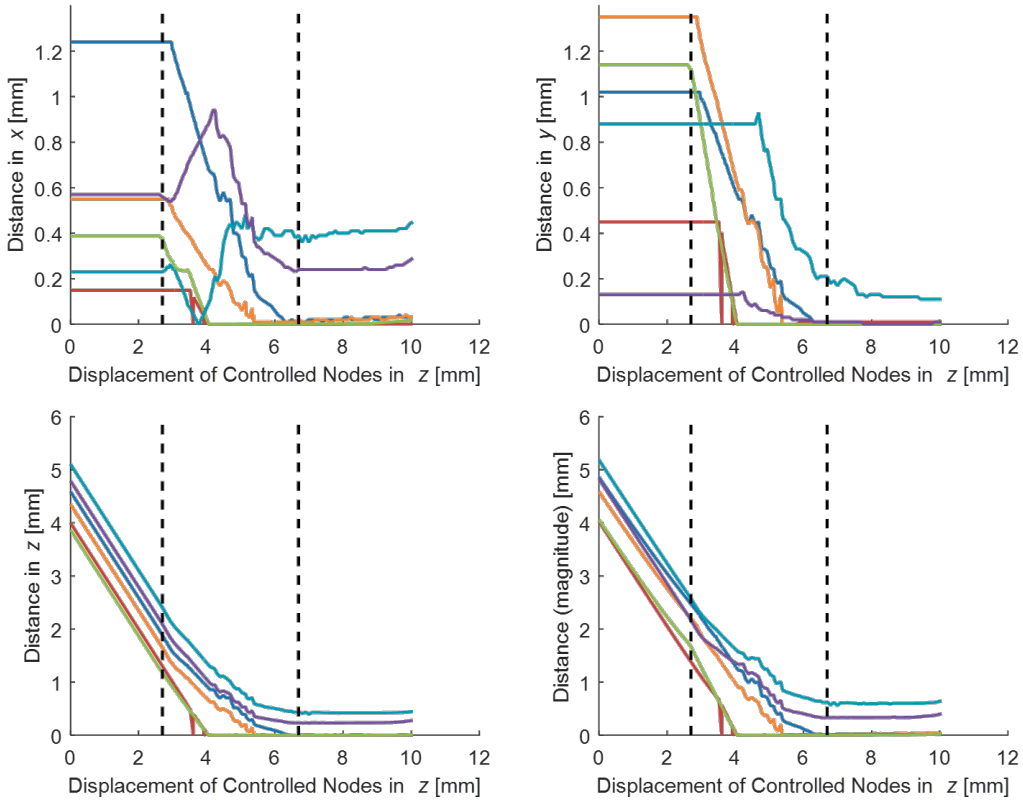

Figure 6.29: Plots of the distances between each of the six cup/cone pairs in the full model with springs for the random misalignment test. The spring constants in this case are 5 N/mm in the x direction, 5.01 N/mm in the y direction, and 50 N/mm in the z direction. The first vertical dashed line marks the point at which the reaction forces at the controlled nodes exceed 0.01 N and the second line marks the point at which the reaction forces exceed 300 N.

and cheaper than increasing the precision of the manufacturing processes.

With the above information, a simple interconnect concept was proposed. This design, drawn from previous literature, features a magnetic interlocking cup/cone system. A detailed simulation model of one module with six interconnects was created. Random errors with bounds determined from the assembly investigation were applied. The simulation showed that the interconnects could not fully engage with these errors, due in part to bending of the spacer beams that create the inter-module gaps. A "soft capture" system was tested by allowing the interconnects some freedom to move and accommodate these errors. This modification improved but did not eliminate the problem. One conclusion may be that the module is just severely overconstrained, with each of the six interconnects imposing a boundary condition in each of the three translational directions and two rotational directions. Thus,

engaging all six interconnects and constraining all of these degrees of freedom simultaneously may be impossible. However, if all degrees of freedom are not constrained after assembly, the stiffness and structural integrity of the completed backplane may be severely reduced. Thus, some or all of the following modifications to the interconnect design may be required:

- a more complex "soft-capture" system that strategically releases certain degrees of freedom entirely during assembly and constrains all degrees of freedom after engagement,
- a horizontal approach, rather than vertical approach, as shown in Figure 6.13, that potentially reduces the effect of spacer beam bending,
- a greater range of robotic adjustment and control that allows the robot to correct errors during assembly based on metrology measurements.

Chapter 7

CONCLUSIONS AND FUTURE DIRECTIONS

In this research, the In-Space Telescope Assembly Robotics (ISTAR) architecture for 20-m to 100-m robotically-assembled space telescopes was established. Elements from previous reputable but outdated concepts were combined with current state-of-the-art robotics and adaptive optics technologies to yield a modernized and viable concept for future missions. In this architecture, the primary mirror is uniquely divided into two types of modules: mirror modules, or groups of commercially available mirror segments and actuators, and deployable truss modules actuated by a combination of spring hinges and robotic control. In orbit, a crawling robot first deploys and connects truss modules to build the primary mirror backplane or supporting structure. The robot then attaches mirror modules to the completed backplane. Both new and traditional feasibility analysis techniques were employed to design the truss module and ensure that precision requirements can be met in the presence of typical space environment loads.

One critical requirement of the architecture is that the truss module deployment is reliable. The primary mirror may be composed of hundreds of modules, each bulk manufactured with standard practices to reduce cost. Thus, depending on the manufacturing tolerances, fabrication errors will be introduced that may hinder deployment. In this research, a comprehensive simulation-based toolkit was developed to quantify the reliability of a deployable truss module with any geometry given a nominal design and set of tolerances. The toolkit can then be used to investigate the effect of design parameters and tolerances on reliability, producing trade studies for optimizing the design and manufacturing process. At the core of the toolkit is the simulation of one deployment, performed using the finite element software Abaqus. The simulation requires a high-fidelity model of the structure, including joint offsets, compliance, and realistic spring hinge actuation. An experiment was performed to verify that the simulation could accurately model deployment behavior. A 1/6th section of the ISTAR truss module was constructed and its shape accurately measured. The experimental module was then deployed several times while tracking select displacements and hinge rotations. Using the shape measurement data, a simulation model was created, and the same displacements and hinge rotations were obtained. The experimental and simulated results were in good agreement, and thus

the deployment simulation was validated.

The validated toolkit was used to adjust the ISTAR truss module design and set the manufacturing tolerances, ensuring that the deployment would be nearly 100% reliable with statistical confidence. First, an initial truss module design was proposed. The individual effects of different error types on the reliability of this design were investigated. Three error types were considered: member length errors, member misalignment errors, and hinge axis errors. It was found that, individually, the tolerances required for near-100% reliability were 1 mm, 1 mm, and 1° for the three error types respectively. After assessing the capabilities of standard manufacturing processes, the hinge misalignment tolerance was determined to be the most difficult to achieve and thus the most detrimental to reliability. The three error types were then combined, yielding a reliability of only 77%, suggesting that the error types are not independent in their effect on the deployment. From this baseline, the following design parameters were varied: member outer diameter, member wall thickness, module depth, joint cross section, compliance level, spring moment, and robotic control points. It was found that increasing the spring moment was the most effective method of increasing reliability without affecting the stiffness or mass of the structure. The design of the truss module was adjusted accordingly, and the final manufacturing tolerances were set to 0.5 mm, 0.5 mm, and 2.5° for the three error types respectively, all reasonably achieved with standard manufacturing practices.

The final effort in this research was to explore the effect of fabrication errors on the assembly of the truss modules. An assembly plan was detailed in which modules are assembled in rings around a central hub, each lowered into place from the top by the robot. A simulation technique was developed to accurately model the assembly process. The results showed that, as the backplane size increased, the distance of any node from its nominal position increased, and thus the surface precision decreased. However, in a given module, the errors were primarily consistent with a rigid body offset. The initial connection misalignments encountered in each assembly step did not increase substantially with backplane size when rigid body components were ignored. However, in some assembly steps, the connection misalignments were as much as five times higher than the applied fabrication errors, a result of random unfortunate error combinations. With this information, a simple interconnect concept with interlocking magnetic cups and cones was initially proposed. However, simulations showed that these interconnects could not fully

engage with the misalignments observed in the assembly process, even with a "soft capture" modification that allowed for some accommodating compliance. Thus, it was concluded that this interconnect design would not meet requirements. Though further investigation was beyond the scope of this research, potential improvements to the design were suggested.

In the future, the deployment reliability toolkit can be used to expand the body of trade studies presented in this thesis, firstly adding more trials to the existing studies to increase statistical confidence, then exploring other truss module geometries and designs. The PACTRUSS was chosen in this research because of its heritage and packaging efficiency. Similarly, Rolamite tape spring hinges were chosen because of their heritage and thorough characterization. New deployable schemes and hinge designs were not in the scope of this thesis, but are active areas of research. One particularly interesting approach could be to replace the Rolamite hinges with simple material hinges, in which some material of the CFC folding member is removed in a strategic location, allowing the member to bend at that point. These hinges require no additional mechanism that adds mass or complexity; rather a CFC tape spring is effectively built directly into the member. One example of a material hinge is shown in Figure 7.1. These kinds of hinges could not only replace the Rolamite hinges, but even the pinned hinges in the module to potentially simplify the joint design and further reduce mass. The resulting moment-rotation behavior is similar to that of a Rolamite hinge, but the kinematics are different. The disadvantage is that the degrees of freedom are not as well constrained, and the material hinges may allow unwanted torsion in the member. The reliability estimation toolkit developed in this thesis can easily be adapted to work with these types of hinges. The toolkit can then be used to determine if the material hinges are more or less reliable than the Rolamite hinges.

As with the deployment reliability toolkit, the assembly analysis and simulation method can be used to explore other assembly plans or assess the effect of different disturbances during assembly. For instance, thermal gradients were not considered in this thesis but may significantly impact and increase the growth of errors. The assembly method could easily be adapted to include thermal loads that may vary spatially and transiently. Then, other assembly plans, like a linear pattern or assembling in large groups, could be simulated to investigate whether they result in reduced error growth and stresses.

Finally, the interconnect concept considered in this research will require sig-

Figure 7.1: Image of an unfolded and folded material hinge in a carbon fiber composite tube. The hinge is created by simply removing a section of material from the tube. Source: [70].

nificant modifications in order to effectively engage despite fabrication errors, and thus follow-up research may pursue entirely new concepts. It is possible that some degrees of freedom must be unconstrained during assembly to accommodate errors and constrained after assembly to rigidize the structure. The design of such a locking mechanism is one potential area of research. Even for a perfect structure, the interconnect must be variable in length to create the required curvature of the mirror. Bulk adjustments may be accomplished with a screw mechanism operated by the robot during assembly. If the precision of the screw mechanism cannot meet requirements, then a piezoelectric system may be required for finer corrections. The same mechanism can be used to reduce fabrication errors during assembly, with the robot making corrections after each connection based on readings from the metrology system. For any preliminary interconnect designs considered in future research, the same principles and simulation techniques applied in this thesis can be used to investigate the interconnect behavior and performance given the expected assembly errors.

BIBLIOGRAPHY

[1] *Hobby-Everly Telescope*. 2014. URL: http://www.as.utexas.edu/mcdonald/het/het.html.

[2] *Southern African Large Telescope*. 2014. URL: http://www.salt.ac.za/.

[3] *W. M. Keck Observatory*. 2016. URL: http://www.keckobservatory.org/.

[4] *Giant Magellan Telescope*. 2016. URL: www.gmto.org.

[5] *Thirty Meter Telescope*. URL: www.tmt.org.

[6] *The European Extremely Large Telescope*. URL: http://www.eso.org/public/usa/teles-instr/e-elt/.

[7] *HubbleSite - The Telescope - Hubble Essentials*. URL: http://hubblesite.org/the%7B%5C_%7Dtelescope/hubble%7B%5C_%7Dessentials/.

[8] *James Webb Space Telescope*. URL: http://www.jwst.nasa.gov/.

[9] *Space Launch System*. URL: http://www.nasa.gov/exploration/systems/sls/.

[10] Marc Postman et al. "Advanced Technology Large-Aperture Space Telescope: Science Drivers and Technology Developments". In: *Optical Engineering* 51.1 (2012), pp. 1–11. DOI: 10.1117/1.OE.51.1.011007. URL: http://dx.doi.org/10.1117/1.OE.51.1.011007.

[11] R. E. Freeland, R. G. Helms, and M. M. Mikulas. "The Applicability of Past Innovative Concepts to the Technology for New Extremely Large Space Antenna/Telescope Structures". In: July 2006. DOI: 10.4271/2006-01-2063. URL: http://papers.sae.org/2006-01-2063/.

[12] M. Card and W. Boyer. "Large space structures - Fantasies and facts". In: *21st Structures, Structural Dynamics, and Materials Conference*. Structures, Structural Dynamics, and Materials and Co-located Conferences. American Institute of Aeronautics and Astronautics, May 1980. DOI: doi:10.2514/6.1980-674. URL: http://dx.doi.org/10.2514/6.1980-674.

[13] Walter L. Heard and Mark S. Lake. "Neutral Buoyancy Evaluation of Extravehicular Activity Assembly of a Large Precision Reflector". In: *Journal of Spacecraft and Rockets* 31.4 (1994), pp. 569–577. DOI: 10.2514/3.26480. URL: http://arc.aiaa.org/doi/abs/10.2514/3.26480.

[14] Marvin D. Rhodes, Ralph W. Will, and Marion A. Wise. "A Telerobotic System for Automated Assembly of Large Space Structures". In: (Mar. 1989). URL: http://ntrs.nasa.gov/search.jsp?R=19890012453.

[15] Walter L. Heard et al. “Astronaut/EVA construction of Space Station”. In: (Jan. 1988). URL: http://ntrs.nasa.gov/search.jsp?R=19880044155.

[16] Judith J. Watson et al. “Results of EVA/mobile Transporter Space Station Truss Assembly Tests”. In: (Nov. 1988). URL: http://ntrs.nasa.gov/search.jsp?R=19890004112.

[17] John W. Ribble. *Modular Antenna Design Study*. Tech. rep. Sunnyvale, California: Lockheed Missiles and Space Company, Inc., 1981.

[18] A. A. Woods. “A Modular Approach Toward Extremely Large Apertures”. In: *NASA. Langley Research Center Large Space Systems Technology*. 1981, pp. 121–143.

[19] D. H. Vaughan. *Modular Reflector Concept Study*. Tech. rep. San Diego, California: General Dynamics Corporation, 1981.

[20] D. H. Vaughan. “Modular Space Structures”. In: *39th Annual Conference of the Society of Allied Weight Engineers, Inc.* St. Louis, Missouri, 1980.

[21] W. E. Agan. “Erectable Concepts for Large Space System Technology”. In: *NASA. Langley Research Center Large Space Systems Technology*. 1980, pp. 183–198.

[22] J. J. Watson, T. J. Collins, and H. G. Bush. “A History of Astronaut Construction of Large Space Structures at NASA Langley Research Center”. In: *Aerospace Conference Proceedings, 2002. IEEE*. Vol. 7. 2002, pp. 7–3569. DOI: 10.1109/AERO.2002.1035334. URL: http://ieeexplore.ieee.org/ielx5/8043/22224/01035334.pdf?tp=%7B%5C&%7Darnumber=1035334%7B%5C&%7Disnumber=22224.

[23] John M. Hedgepeth and Martin M. Mikulas. “Expandable Modules for Large Space Structures”. In: *Conference on Advanced Technology for Future Space Systems*. Meeting Paper Archive. American Institute of Aeronautics and Astronautics, May 1979. DOI: doi:10.2514/6.1979-924. URL: http://dx.doi.org/10.2514/6.1979-924.

[24] W. H. Armstrong, D. E. Skoumal, and J. W. Straayer. *Large Erectable Space Structures*. Tech. rep. Seattle, Washington: Boeing Aerospace Company, 1977.

[25] Mark A. Ealey and John A. Wellman. “Xinetics Low-cost Deformable Mirrors with Actuator Replacement Cartridges”. In: *1994 Symposium on Astronomical Telescopes & Instrumentation for the 21st Century*. Ed. by Mark A. Ealey and Fritz Merkle. International Society for Optics and Photonics, May 1994, pp. 680–687. DOI: 10.1117/12.176104. URL: http://proceedings.spiedigitallibrary.org/proceeding.aspx?articleid=961003.

[26] Allan Wirth et al. “Deformable Mirror Technologies at AOA Xinetics”. In: *SPIE Optics + Optoelectronics*. Ed. by Joachim Hein, Georg Korn, and Luis O. Silva. International Society for Optics and Photonics, May 2013, p. 87800M. DOI: 10.1117/12.2018031. URL: http://proceedings.spiedigitallibrary.org/proceeding.aspx?articleid=1686114.

[27] John Steeves et al. “Design, Fabrication and Testing of Active Carbon Shell Mirrors for Space Telescope Applications”. In: *SPIE Astronomical Telescopes + Instrumentation*. Ed. by Ramón Navarro, Colin R. Cunningham, and Allison A. Barto. International Society for Optics and Photonics, July 2014, p. 915105. DOI: 10.1117/12.2056560. URL: http://proceedings.spiedigitallibrary.org/proceeding.aspx?articleid=1892546%7B%5C&%7DresultClick=1.

[28] Keith Patterson, Sergio Pellegrino, and James Breckinridge. “Shape Correction of Thin Mirrors in a Recongurable Modular Space Telescope”. In: *SPIE Astronomical Telescopes + Instrumentation*. Ed. by Jacobus M. Oschmann Jr., Mark C. Clampin, and Howard A. MacEwen. International Society for Optics and Photonics, July 2010, p. 773121. DOI: 10.1117/12.861442. URL: http://proceedings.spiedigitallibrary.org/proceeding.aspx?articleid=750070.

[29] Reed L. Riddle et al. “The Robo-AO Automated Intelligent Queue System”. In: *SPIE Astronomical Telescopes + Instrumentation*. Ed. by Gianluca Chiozzi and Nicole M. Radziwill. Montreal, CA: International Society for Optics and Photonics, July 2014, 91521E. DOI: 10.1117/12.2056534. URL: http://proceedings.spiedigitallibrary.org/proceeding.aspx?articleid=1890827.

[30] Christoph Baranec et al. “High-Efficiency Autonomous Laser Adaptive Optics”. In: *The Astrophysical Journal* 790.1 (July 2014), p. L8. ISSN: 2041-8205. DOI: 10.1088/2041-8205/790/1/L8. URL: http://arxiv.org/abs/1407.8179.

[31] *RoboSimian*. URL: http://www.theroboticschallenge.org/teams/robosimian.

[32] Brett Kennedy et al. “LEMUR: Legged Excursion Mechanical Utility Rover”. In: *Autonomous Robots* 11.3 (2001), pp. 201–205. DOI: 10.1023/A:1012474603861.

[33] Lee D. Feinberg et al. “Modular Assembled Space Telescope”. In: *Optical Engineering* 52.9 (Apr. 2013), p. 091802. ISSN: 0091-3286. DOI: 10.1117/1.OE.52.9.091802. URL: http://opticalengineering.spiedigitallibrary.org/article.aspx?doi=10.1117/1.OE.52.9.091802.

[34] Santanu Basu, Terry Mast, and Gary Miyata. "A Proposed Autonomously Assembled Space Telescope (AAST)". In: *AIAA Space 2003 Conference & Exposition*. Reston, Virigina: American Institute of Aeronautics and Astronautics, Sept. 2003. ISBN: 978-1-62410-103-8. DOI: 10.2514/6.2003-6369. URL: http://arc.aiaa.org/doi/10.2514/6.2003-6369.

[35] R. M. Muller. "Assembly and Servicing of a Large Telescope at the International Space Station". In: *Proceedings, IEEE Aerospace Conference*. Vol. 7. IEEE, 2002, pp. 7–3611. ISBN: 0-7803-7231-X. DOI: 10.1109/AERO.2002.1035337. URL: http://ieeexplore.ieee.org/lpdocs/epic03/wrapper.htm?arnumber=1035337.

[36] Craig Underwood et al. "Using CubeSat/micro-satellite Technology to Demonstrate the Autonomous Assembly of a Reconfigurable Space Telescope (AAReST)". In: *Acta Astronautica* 114 (Sept. 2015), pp. 112–122. ISSN: 00945765. DOI: 10.1016/j.actaastro.2015.04.008. URL: http://www.sciencedirect.com/science/article/pii/S0094576515001642.

[37] W. Keats Wilkie et al. *Structural Feasibility Analysis of a Robotically Assembled Very Large Aperture Optical Space Telescope*. 2007. DOI: doi:10.2514/6.2007-181410.2514/6.2007-1814. URL: http://dx.doi.org/10.2514/6.2007-1814.

[38] Akira Meguro, Hironori Ishikawa, and Akio Tsujihata. "Study on Ground Verification for Large Deployable Modular Structures". In: *Journal of Spacecraft and Rockets* 43.4 (July 2006), pp. 780–787. ISSN: 0022-4650. DOI: 10.2514/1.16037. URL: http://www.researchgate.net/publication/245438560%7B%5C_%7DStudy%7B%5C_%7Don%7B%5C_%7DGround%7B%5C_%7DVerification%7B%5C_%7Dfor%7B%5C_%7DLarge%7B%5C_%7DDeployable%7B%5C_%7DModular%7B%5C_%7DStructures.

[39] R. W. Herr and G. C. Horner. "Deployment Tests of a 36-element Tetrahedral Truss Module". In: *NASA. Langley Research Center Large Space Systems Technology*. Vol. 2. 1981, pp. 59–69. URL: http://adsabs.harvard.edu/abs/1981lsst....2...59H.

[40] Masayoshi Misawa. "Deployment Reliability Predicition for Large Satellite Antennas Driven by Spring Mechanisms". In: *Journal of Spacecraft and Rockets* 31.5 (May 1994). URL: http://arc.aiaa.org/doi/abs/10.2514/3.26526?journalCode=jsr.

[41] John M. Hedgepeth. "Influence of Fabrication Tolerances on the Surface Accuracy of Large Antenna Structures". In: *AIAA Journal* 20.5 (1982), pp. 680–686. DOI: 10.2514/3.7936.

[42] John M. Hedgepeth and Richard K. Miller. *Investigation of Structural Behavior of Candidate Space Station Structure*. Tech. rep. Carpinteria, California: Astro Aerospace Corporation, 1989.

[43] E. Komendera and N. Correll. “Precise Assembly of 3D Truss Structures using MLE-based Error Prediction and Correction”. In: *The International Journal of Robotics Research* 34.13 (Oct. 2015), pp. 1622–1644. ISSN: 0278-3649. DOI: 10.1177/0278364915596588. URL: http://ijr.sagepub.com/content/early/2015/10/15/0278364915596588.abstract.

[44] Erik Komendera et al. “Truss Assembly and Welding by Intelligent Precision Jigging Robots”. In: *2014 IEEE International Conference on Technologies for Practical Robot Applications (TePRA)*. IEEE, Apr. 2014, pp. 1–6. ISBN: 978-1-4799-4605-1. DOI: 10.1109/TePRA.2014.6869150. URL: http://ieeexplore.ieee.org/lpdocs/epic03/wrapper.htm?arnumber=6869150.

[45] John M. Hedgepeth. *Critical Requirements for the Design of Large Space Structures*. Tech. rep. Carpinteria, California: Astro Aerospace Corporation, 1981. URL: http://catalog.hathitrust.org/Record/011432076%20http://hdl.handle.net/2027/uiug.30112106584581.

[46] Mark S. Lake, Lee D. Peterson, and Martin M. Mikulas. “Space Structures on the Back of an Envelope: John Hedgepeth’s Design Approach”. In: *Journal of Spacecraft and Rockets* 43.6 (2006), pp. 1174–1183. DOI: 10.2514/1.21076.

[47] Lee Peterson and Gregory Agnes. *How the Mass of Large Gossamer Optical Telescopes Scales with Size and Disturbance Environment*. 2007. DOI: doi:10.2514/6.2007-181310.2514/6.2007-1813. URL: http://dx.doi.org/10.2514/6.2007-1813.

[48] *Abaqus*. 2014.

[49] Aden B. Meinel and Marjorie P. Meinel. “Two-stage Optics: High-acuity Performance from Low-acuity Optical Systems”. In: *Optical Engineering* 31.11 (1992), p. 11. DOI: 10.1117/12.59946.

[50] *Sunjammer*. 2014. URL: http://www.sunjammermission.com/home.

[51] *Articulated Mast Systems*. 2014. URL: http://www.atk.com/products-services/articulated-mast-systems.

[52] Nicolas Hudson et al. “Model-based Autonomous System for Performing Dexterous, Human-level Manipulation Tasks”. In: *Autonomous Robots* 36.1-2 (2014), pp. 31–49. DOI: 10.1007/s10514-013-9371-y. URL: http://dx.doi.org/10.1007/s10514-013-9371-y.

[53] Nicolas Lee, Sergio Pellegrino, and Yen-Hung Wu. “A Design Algorithm for the Placement of Identical Segments in a Large Spherical Mirror”. In: *Journal of Astronomical Telescopes, Instruments, and Systems* 1.2 (2015).

[54] John M. Hedgepeth. *Pactruss Support Structure for Precision Segmented Reflectors*. Tech. rep. Carpinteria, California: Astro Aerospace Corporation, 1989.

[55] Alan M. Watt. "Deployable Structures with Self-locking Hinges". PhD thesis. University of Cambridge, 2003. URL: http://ethos.bl.uk/OrderDetails.do?uin=uk.bl.ethos.426505.

[56] *M55J Data Sheet*. URL: http://www.toraycfa.com/pdfs/M55JDataSheet.pdf.

[57] Yunus A. Çengel. *Heat and Mass Transfer: a Practical Approach*. Boston: McGraw-Hill, 2007.

[58] Mark S. Lake, Lee D. Peterson, and Marie B. Levine. "Rationale for Defining Structural Requirements for Large Space Telescopes". In: *Journal of Spacecraft and Rockets* 39.5 (2002), pp. 674–681. DOI: 10.2514/2.3889.

[59] *Technical Specs*. URL: https://www.rockwestcomposites.com/technical-specs.

[60] *Mechanical Properties of Carbon Fibre Composite Materials*. URL: http://www.performance-composites.com/carbonfibre/mechanicalproperties%7B%5C_%7D2.asp.

[61] *ABS M-30, Fortus 3D Production Systems FDM Materials*. URL: http://www.stratasys.com/materials/fdm/abs-m30.

[62] *Specifications for Common Plastic Molding Design Material*. URL: http://www.engineersedge.com/plastic/materials%7B%5C_%7Dcommon%7B%5C_%7Dplastic.htm.

[63] Martin M. Mikulas and Robert F. Crawford. *Sequentially Deployable Maneuverable Tetrahedral Beam*. Dec. 1985. URL: https://www.google.com/patents/US4557097.

[64] Michihiro Natori. *Jointed Extendible Truss Beam*. Apr. 1987. URL: https://www.google.com/patents/US4655022.

[65] John M. Hedgepeth and Louis R. Adams. *Design Concepts for Large Reflector Antenna Structures*. Tech. rep. Washington, United States, 1983.

[66] C. J. Clopper and E. S. Pearson. "The Use of Confidence or Fiducial Limits Illustrated in the Case of the Binomial". In: *Biometrika* 26.4 (1934), pp. 404–413. DOI: 10.1093/biomet/26.4.404. URL: http://biomet.oxfordjournals.org/cgi/doi/10.1093/biomet/26.4.404.

[67] *Carbon/Epoxy Composite Tube C 427477*. URL: https://www.goodfellowusa.com/catalog.

[68] Sergio Pellegrino. "Structural Computations with the Singular Value Decomposition of the Equilibrium Matrix". In: *International Journal of Solids and Structures* 30.21 (1993), pp. 3025–3035. DOI: http://dx.doi.org/10.1016/0020-7683(93)90210-X. URL: http://www.sciencedirect.com/science/article/pii/002076839390210X.

[69] *Coefficient of Friction Reference Table*. URL: http://www.engineershandbook.com/Tables/frictioncoefficients.htm.

[70] H.M.Y.C. Mallikarachchi and Sergio Pellegrino. "Optimized Designs of Composite Booms with Tape Spring Hinges". In: *51st AIAA/ASME/ASCE/AHS/ASC Structures, Structural Dynamics, and Materials Conference*. Structures, Structural Dynamics, and Materials and Co-located Conferences. American Institute of Aeronautics and Astronautics, Apr. 2010. DOI: doi:10.2514/6.2010-2750. URL: http://dx.doi.org/10.2514/6.2010-2750.